



NTNU – Trondheim
Norwegian University of
Science and Technology

Electrical Transport Studies of (111)-Oriented BTO/LSMO-Based Heterostructures

Kristoffer Skogen Raa

Nanotechnology

Submission date: June 2015

Supervisor: Thomas Tybell, IET

Norwegian University of Science and Technology
Department of Electronics and Telecommunications

Abstract

Strain-induced magnetoelectric coupling in thin film heterostructures is a popular topic in the emerging field of multiferroic materials. Normally such heterostructures are grown with a (001) orientation, but (111)-oriented structures may exhibit increased coupling at the interfaces. In this study, the electrical transport properties of (111)-oriented ferroelectric-ferromagnetic BTO/LSMO heterostructures were investigated in order to explore the possible effects of magnetoelectric coupling.

An experimental technique was established that enabled important transport properties to be measured, such as resistivity, magnetoresistance, carrier density and mobility. Van der Pauw's method formed the basis for the measurements, but a simplified version was employed which utilized data from a single bonding configuration. Because of additional simplifications and other potential errors, the technique was considered to be best suited for qualitative investigations.

A one-band model was adopted when analyzing the Hall measurements, but the process was complicated by the presence of the anomalous Hall effect. To circumvent the anomalous contributions, the slope in the linear region of the Hall resistance was used as a measure of the ordinary Hall effect. Overall, the Hall measurements were found to be most accurate in the region 100 – 275 K. At higher temperatures, the complexity of the Hall effect prevented qualitative results from being obtained by the use of simple models. Below 100 K instrument limitations was the main issue.

To improve the accuracy in future work, the following suggestions were proposed: A complete implementation of van der Pauw's method, usage of metal masks for gold contact formation, and an automated method of optimizing curve fits and instrument parameters.

Between 50 – 400 K, the resistivities ranged from $0.3 \text{ m}\Omega \cdot \text{cm}$ to $80 \text{ m}\Omega \cdot \text{cm}$, which is comparable to known values for (001)-oriented LSMO. A reference sample exhibited a magnetoresistance close to -45% at 3 T, which surpasses the findings in similar studies. Between 100 – 275 K, the carrier densities were calculated as 1 – 2 holes/unit cell, which is in agreement with reports on (001)-oriented LSMO. An up to 10-fold increase of the resistivities was observed for samples with LSMO grown on top of BTO rather than directly on the STO substrates. Furthermore, the metal-insulator transition temperatures and magnetoresistance peak temperatures were up to 70 K lower for these samples. This was believed to be caused by lower LSMO film quality due to non-ideal epitaxial growth of the BTO layers. Even though the transport properties differed significantly between the heterostructures, no clear signs of strain-mediated magnetoelectric coupling were observed.

Sammendrag

Multiferroiske materialer som utviser tøyings-indusert magnetoelektrisk kobling i tynnfilm heterostrukturer er et lovende forskningsområde i rask fremvekst. Vanligvis blir slike heterostrukturer grodd med en (001) orientering, men det er mulig at (111)-orienterte strukturer kan inneha en større grad av kobling ved grensesjiktene. I denne studien ble de elektriske transportegenskapene til (111)-orienterte ferroelektriske-ferromagnetiske BTO/LSMO heterostrukturer undersøkt for å utforske mulige effekter av magnetoelektrisk kobling.

En eksperimentell teknikk ble etablert som gjorde det mulig å måle viktige transportegenskaper som resistivitet, magnetoresistans, bærertetthet og mobilitet. Målingene var basert på van der Pauws metode, men en forenklet versjon ble benyttet hvor data kun ble inkludert fra én enkelt lednings-konfigurasjon. Kombinert med andre feilkilder medførte dette at teknikken ble regnet for å være best egnet til innledende og kvalitative studier.

En modell som kun tar hensyn til ett enkelt ledningsbånd ble brukt til å analysere Hall målinger, men den anomale Hall effekten gjorde tolkningen av målingene komplisert. Stigningstallet til den lineære delen av Hall resistansen ble brukt som et mål på den ordinære Hall effekten for å unngå anomale bidrag. Generelt ble det påvist at Hall-målingene var mest nøyaktig i temperaturintervallet 100 – 275 K. Ved høyere temperaturer er Hall effekten for avansert til å kunne analyseres ved bruk av enkle modeller. Under 100 K var hovedproblemet instrumentbegrensninger.

Følgende endringer ble foreslått for å kunne utbedre nøyaktigheten i framtidig arbeid: En komplett implementasjon av van der Pauws metode, bruk av metallmasker for deponering av gullkontakter og en automatisert metode for å optimalisere kurvetilpasninger og instrumentparametre.

Mellom 50 – 400 K varierte resistiviteten fra $0.3 \text{ m}\Omega \cdot \text{cm}$ til $80 \text{ m}\Omega \cdot \text{cm}$, som er sammenlignbart med kjente verdier for (001)-orientert LSMO. Magnetoresistansen til en referanseprøve ble målt til -45% ved 3 T som er høyere enn rapporterte verdier i lignende studier. I området 100 – 275 K ble bærertettheten målt til 1 – 2 hull/enhetscelle. Dette er i samsvar med kjente verdier for (001)-orientert LSMO. En opp mot tidobling av resistiviteten ble påvist for prøver med LSMO grodd på toppen av BTO, i stedet for direkte på STO substratet. Disse strukturene hadde også opp mot 70 K lavere temperaturer for toppunktet til magnetoresistansen og overgangen mellom metallisk og isolerende fase. Dette ble sett på som et mulig tegn på lavere filmkvalitet på grunn av ikke-ideell epitaktisk vekst av BTO-lagene. Til tross for at transportegenskapene varierte betydelig for ulike heterostrukturer, ble det ikke observert noen sikre tegn på tøyings-indusert magnetoelektrisk kobling.

Preface

This master's thesis was performed during the spring 2015 at the Department of Electronics and Telecommunications, NTNU. The work was completed in laboratories at the institute, and at NTNU NanoLab.

Recently a method has been developed by the oxide electronics group at NTNU, which enables growth of (111)-oriented perovskites. BTO/LSMO-based heterostructures that are grown using this method are expected to exhibit altered properties and possibly strain-mediated coupling at the interfaces. Most of the time spent on this thesis was devoted to the development of a technique that is able to characterize the electrical transport properties of such structures.

In practice this work was started from scratch, and various mistakes were made that seemed obvious at the end of this work. As an example, the limitations related to performing measurements efficiently using van der Pauw's method were discovered over halfway through this work. Because of the time consuming measurements, a few unnecessary simplifications had to be made in order to obtain results within the limited time span. Fortunately, many pitfalls and potential errors were discovered by the end of this work. Even though the final outcome was not as good as I hoped, I am certain that the developed technique can be of greater use in the future if the suggested improvements are implemented.

I would like to give a thanks to my always enthusiastic supervisor Prof. Thomas Tybell. He has guided me along the way, and given me valuable feedback through interesting discussions. I would like to thank Torstein Bolstad for making the sample structures and for proofreading my thesis. I also want to thank Jonas M. Ribe for introducing me to the wire bonding tool. The Research Council of Norway is acknowledged for the support to NTNU NanoLab through the Norwegian Micro- and Nano-Fabrication Facility, NorFab (197411/V30). Finally, I would like to thank my friends and family for their support throughout this thesis and all my years at NTNU.

Kristoffer Skogen Raa
NTNU, Trondheim
June 16, 2015

Contents

Abstract	iii
Sammendrag	v
Preface	vii
List of Abbreviations	xi
List of Figures	xiii
List of Tables	xv
1 Introduction	1
1.1 Motivation	1
1.2 Background	2
1.3 Outline	2
2 Theory	5
2.1 Perovskite Manganites – $\text{La}_{1-x}\text{Sr}_x\text{MnO}_3$	5
2.1.1 Crystal Structure	5
2.1.2 Electrical Transport in LSMO	5
2.1.3 Effect of Doping Concentration	8
2.1.4 The Colossal Magnetoresistance Effect	8
2.2 BaTiO_3	9
2.3 Multiferroic Materials	10
2.3.1 The Magnetoelectric Effect	10
2.3.2 Multi-Phase Compounds and Composites	13
2.3.3 Magnetoelectric Random Access Memory	15
2.3.4 (111)-Oriented BTO/LSMO Heterostructures	17
2.4 State of the Art	18
2.4.1 LSMO Transport Properties	18
2.4.2 ME Coupling in BTO/LSMO Heterostructures	19
2.5 The Hall Effect	20
2.5.1 One-Band Approximation	20

2.5.2	Two-Band Model	22
2.5.3	The Anomalous Hall Effect	23
3	Experimental	27
3.1	Sample Structures	27
3.2	The Van Der Pauw Method	29
3.2.1	Resistivity Measurements	29
3.2.2	Hall Measurements: Mobility and Carrier Density	31
3.2.3	AC Current Hall Measurements	33
3.2.4	Error Estimation	34
3.3	Preparation of Gold Contacts	35
3.4	Wire Bonding	35
3.5	Electrical Transport Measurements	39
3.5.1	ETO Parameters	40
3.5.2	ETO Scripts	41
3.6	Data Processing and Measurement Overview	43
4	Results and Discussion	45
4.1	Calculating the Hall Resistance	45
4.2	Calculating the Carrier Density	49
4.2.1	Single-Value-Based Calculations	50
4.2.2	Slope-Based Calculations	50
4.3	Bonding Scheme	56
4.3.1	Resistivity and Magnetoresistance	57
4.3.2	Hall Resistance and Carrier Density	58
4.3.3	Conclusion	60
4.4	General Errors	60
4.4.1	Finite Contact Dimensions	61
4.4.2	Aluminum Bonds	61
4.4.3	ETO Parameters	61
4.5	BTO/LSMO Heterostructures	62
4.5.1	Resistivity vs. Temperature	62
4.5.2	Magnetoresistance vs. Temperature	64
4.5.3	Magnetoresistance vs. Magnetic Field	64
4.5.4	Carrier Density	67
4.6	Mobility	67
5	Conclusion	71
5.1	Future Prospects	72
	References	82
	Appendix A ETO Scripts	83
A.1	Resistivity and MR vs. Temperature	83
A.2	MR vs. Magnetic Field	84
A.3	Hall Measurements	84

Appendix B MATLAB Scripts	85
B.1 Resistivity and MR vs. Temperature	85
B.2 Hall Measurements	90
B.3 MR vs. Magnetic Field	95
B.4 General Functions	97
Appendix C Testing Structures	99

List of Abbreviations

BFO	BiFeO ₃ .
BTO	BaTiO ₃ .
CMR	Colossal MagnetoResistance.
ETO	Electrical Transport Option.
FeRAM	Ferroelectric Random Access Memory.
LCMO	La _{1-x} Ca _x MnO ₃ .
LFMR	Low Field MagnetoResistance.
LSMO	La _{1-x} Sr _x MnO ₃ .
MBE	Molecular Beam Epitaxy.
ME	MagnetoElectric.
MR	MagnetoResistance.
MRAM	Magnetic Random Access Memory.
PLD	Pulsed Laser Deposition.
STO	SrTiO ₃ .
T_C	Paramagnetic to ferromagnetic transition temperature.
T_{MI}	Metal-Insulator transition temperature.

TMR Tunneling MagnetoResistance.

List of Figures

2.1	Simplified unit cell LSMO	6
2.2	Double exchange mechanism	7
2.3	Typical resistivity and T_{MI} behavior for LSMO thin films	7
2.4	BaTiO ₃ crystal structures	10
2.5	BaTiO ₃ phase diagram	11
2.6	Mechanism for the composite magnetoelectric effect	14
2.7	Magnetoelectric random access memory	16
2.8	BTO/LSMO crystal orientations and interfaces	17
2.9	Hall effect overview	21
2.10	Overview anomalous Hall effect mechanisms	24
3.1	Illustration of sample heterostructures	28
3.2	Classical six point Hall geometry	29
3.3	Arbitrary sample shape for van der Pauw measurements	30
3.4	Square sample setups for van der Pauw resistivity measurements	31
3.5	Van der Pauw Hall setup for square sample	32
3.6	Diagram for ideal and non-ideal Hall measurement	33
3.7	Gold contact formation via lift-off	36
3.8	Wedge bonding process	37
3.9	Illustration of parallel bonding pattern to sample puck	39
4.1	Ideal resistance vs. field plot for Hall measurements with no zero field offsets – BTO(1.26 nm)/LSMO	46
4.2	Finite zero field offsets for non-ideal resistance vs. field plot for Hall measurements – BTO(1.26 nm)/LSMO	47
4.3	Hall resistance offsets vs. temperature – reference	47
4.4	Temperature stability test – BTO(100 nm)/LSMO	48
4.5	Hall resistances between 150 – 300 K – reference	51
4.6	Single-value-based carrier density – reference	51
4.7	Carrier density calculated using slope-based method – reference	53
4.8	Comparisons of carrier densities calculated using different ranges of Hall resistances – reference	53
4.9	High temperature Hall resistances – reference	54
4.10	Hall resistance differences over the linear range – reference	55

4.11	Magnified versions of the linear region of the Hall resistance – reference	55
4.12	Resistivity comparisons of two bonding configurations – reference . .	57
4.13	Magnetoresistance comparisons of two bonding configurations – reference	58
4.14	Hall resistance comparisons using two different bonding configurations – BTO(5 nm)/LSMO	59
4.15	Carrier density comparisons using two different bonding configurations – BTO(5 nm)/LSMO	60
4.16	Resistivity vs. temperature comparison – all samples	63
4.17	Magnetoresistance vs. temperature comparison – all samples	65
4.18	Magnetoresistance vs. external field – reference sample	66
4.19	Magnetoresistance vs. external field – LSMO/BTO(5 nm)	66
4.20	Calculated carrier densities – all samples	68
4.21	Carrier mobilities for the reference sample (a) , and BTO(5 nm)/LSMO (b)	69
A.1	ETO script: resistivity and magnetoresistance vs. temperature . . .	83
A.2	ETO script: magnetoresistance vs. magnetic field	84
A.3	ETO script: Hall measurements	84

List of Tables

2.1	LSMO doping regimes	8
3.1	Wedge bonding parameter list	38
3.2	Measurement overview for the studied samples	43
4.1	Metal-insulator temperatures – all samples	62
C.1	Overview of testing sample structures	99

1. Introduction

1.1 Motivation

Today consumers have grown accustomed to significant performance increases as they upgrade their cellphones and computers every few years. In accordance with Moore's law [1], the industry has continuously fulfilled these expectations by decreasing component dimensions. Back in 1960, Nobel laureate Richard Feynman envisioned the success of Moore's law even before its existence when he stated that "There's plenty of room at the bottom" [2]. Subsequently, device miniaturization and the introduction of nanotechnology has proved his vision to hold true. However, scaling benefits are expected to diminish as the critical sizes reach the quantum regime and the fundamental physical limits [3]. Therefore, researchers have started the search for alternative solutions that can keep up with consumer demands, without Moore's law being the main driving force.

In 2010 the phrase "More than Moore" was born [4]. This phrase refers to a new trend suggesting that future advances might result from incorporation of new functionalities rather than downscaling. Similarly to Feynman's famous words, this foreshadowing may mark the beginning of a new era. Oxide materials are strong candidates for this new trend since they display an unmatched variety of electronic properties, such as ferromagnetism and ferroelectricity. Furthermore, they may exhibit exotic effects such as giant and colossal magnetoresistance [5], or high T_C superconductivity [6]. Many of these effects and properties have already been utilized in applications such as magnetic and ferroelectric random access memories (MRAM and FeRAM) [7, 8], spintronics [9] and hard disk read heads [10].

Nowadays one of the most popular topics within oxide electronics is multiferroics, which are materials that exhibit at least two ferroic orders simultaneously, e.g. ferromagnetism and ferroelectricity [11]. The ferroic orders may be coupled through the magnetoelectric effect, implying that magnetic properties can be controlled electrically and vice versa [12, 13]. If multiferroic materials are realized with a strong magnetoelectric coupling, novel devices are expected to follow with higher performance and lower power consumption than the current generation of components [14, 15].

1.2 Background

A major challenge within the field of multiferroics, is to find materials that exhibit strong magnetoelectric coupling at room temperature. Over the past few years, perovskite thin film heterostructures have proved to be one of the best candidates in order to overcome this challenge [16]. Normally such heterostructures are grown with a (001) orientation, but the growth of high-quality and atomically flat (111)-oriented perovskite oxides films have recently been accomplished [17,18]. Compared to (001)-oriented heterostructures, a larger number of oxygen atoms are shared between the octahedra at the interfaces, which suggests that the magnetoelectric coupling might be stronger.

In this work a potential magnetoelectric coupling were to be studied between ferroelectric BaTiO₃ (BTO) and ferromagnetic La_{0.7}Sr_{0.3}MnO₃ (LSMO), when grown as heterostructures on (111)-oriented SrTiO₃ (STO) substrates. LSMO doped with 30 % Sr²⁺ is known to be a spin-polarized half-metal, with electrical transport properties that depend on the arrangement of the oxygen atoms. Therefore, interaction with the BTO layers at the interfaces is expected to alter its properties. In other words, observations of abnormal transport behavior may indicate a magnetoelectric coupling¹. Evidence of such interface coupling have already been observed as discontinuous jumps in the resistivity for (001)-oriented BTO/LSMO samples [19].

Consequently, the first main goal of this work was to establish a technique that can be used to characterize important transport properties such as resistivity, magnetoresistance and carrier density. Specifically this requires an experimental procedure to be optimized, and a set of tools to be developed that can analyze the data automatically.

The second goal was to utilize this technique to carry out a series of measurements on a selection of sample structures. By comparing the obtained results, the objective was to discover general trends and come up with potential explanations. In essence, solving both of these goals would help determine if (111)-oriented BTO/LSMO heterostructures can help improve the magnetoelectric coupling in multiferroic composites.

1.3 Outline

Following this introduction, chapter 2 will provide a theoretical background for the chosen materials and an overview of the physics related to the relevant transport properties. This includes a general introduction of the Hall effect and a few details that are specific for LSMO, such as the anomalous Hall effect and the colossal magnetoresistance. Furthermore, an overview is given for multiferroic materials and the magnetoelectric effect. Section 2.4 reviews state of the art research related to LSMO as a stand alone material, and when used in heterostructures.

Chapter 3 introduces the experimental techniques and procedures that were established, such as gold contact formation, wire bonding and electrical transport

¹A study of the potential magnetic changes was performed by others in parallel to this work.

measurements. Since the entire procedure was based on van der Pauw's method, this method has been explained thoroughly.

Chapter 4 presents the results and discusses them continuously. This chapter is divided into two parts where the first focuses on the establishment of the technique, and the second on the obtained results for the heterostructures.

Finally, a conclusion is given in chapter 5. This part suggests how the developed techniques can be used in future work, and summarizes the investigations of potential magnetoelectric coupling in BTO/LSMO-based heterostructures.

2. Theory

2.1 Perovskite Manganites – $\text{La}_{1-x}\text{Sr}_x\text{MnO}_3$

Perovskite manganites is a class of materials exhibiting a large variety of magnetic and electronic properties such as ferromagnetism, antiferromagnetism, charge and orbital ordering, and magnetic-field driven metal-insulator transitions [20]. The general formula is $\text{RE}_{1-x}\text{AE}_x\text{MnO}_3$ where RE is a trivalent rare earth ion (La^{3+} , Pr^{3+} or Nd^{3+}) and AE a divalent alkaline earth ion (Sr^{2+} , Ca^{2+} , Ba^{2+} or Pb^{2+}) [21]. Depending on the exact content of the ions, the material properties and temperature characteristics may vary significantly. $\text{La}_{1-x}\text{Sr}_x\text{MnO}_3$ (LSMO) is one of the compounds within this class, and specifically $\text{La}_{0.7}\text{Sr}_{0.3}\text{MnO}_3$ was used as the ferromagnetic layer in this study¹. The following parts give an overview of LSMO and its related properties.

2.1.1 Crystal Structure

LSMO is synthesized by doping the parent compound LaMnO_3 with Sr^{2+} . The unit cell of bulk LSMO is a distorted perovskite, often described as pseudo-cubic with a lattice parameter and unit cell angle of 3.87 \AA and 90.26° respectively [22, 23]. Using a more complete description, the unit cell is characterized as rhombohedral with space group $R\bar{3}c$ and lattice constants $a_r = 5.471 \text{ \AA}$ and $\alpha_r = 60.43^\circ$ [24, 25]. A simplified illustration of the unit cell is shown in Fig. 2.1, where the Mn ions sits in the middle of an oxygen octahedron and the La/Sr ions occupy the corners of the cube. Normally these octahedra are slightly distorted

2.1.2 Electrical Transport in LSMO

Undoped LaMnO_3 is an A-type antiferromagnet and a Mott insulator. According to the classical band model by Bloch-Wilson, Mott insulators are expected to be electrically conducting [26]. In reality however, they are insulating due to electron-electron interactions that are not accounted for in the classical band model [27]. Despite the fact that the parent compound is insulating, adding dopants can turn

¹The short term LSMO may refer to both the general formula and the specific composition utilized in this work. In this chapter it is used to describe the general compound.

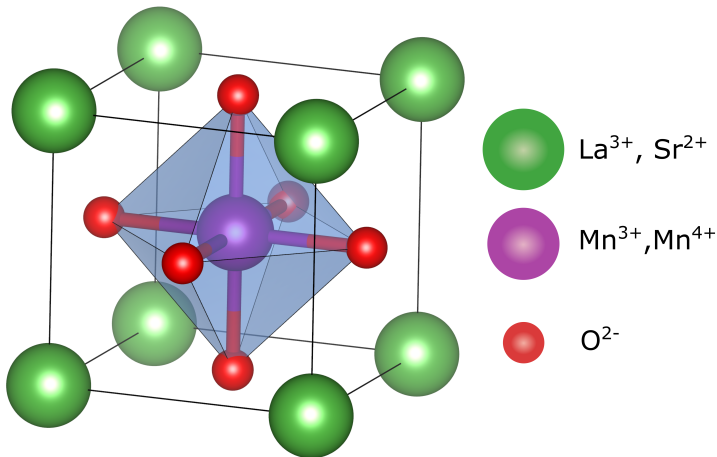


Figure 2.1: Simple representation of the LSMO unit cell, where the distortion of the oxygen octahedra has been neglected.

LSMO into a spin-polarized half-metal for certain doping concentrations [28]. Substituting La^{3+} with Sr^{2+} changes the manganese valence from Mn^{4+} in undoped LaMnO_3 to a mixture of Mn^{3+} and Mn^{4+} in LSMO [29]. Upon doping, the mixed manganese valence promotes electron hopping from Mn^{3+} to a vacant position in a neighboring Mn^{4+} . This hopping motion takes place via the 2p orbitals of the oxygen atoms. Such electron movement was first described by Zener in 1951, and is referred to as the double exchange mechanism [30]. The simultaneous hopping from Mn^{3+} to O^{2-} and from O^{2-} to Mn^{4+} is illustrated in Fig. 2.2.

In LSMO the spins are strongly coupled in accordance with Hund's rules [31]. Effectively this means that the hopping probability and the electrical conductance is at a maximum when the manganese spins are parallel. Moreover, the hopping motion and the double exchange interactions are suppressed when the spins are misaligned [32]. In other words, the electrical transport and ferromagnetic interaction both depend on the alignment of spins, and therefore they are closely linked. Evidence of this connection can be observed when comparing the metal-insulator transition temperature T_{MI} , to the Curie temperature T_C . An example of these transition temperatures is shown in Fig. 2.3. The metal-insulator transition temperature is defined as the peak of the resistivity vs. temperature curve, while T_C denotes the paramagnetic to ferromagnetic transition. This plot also represents the expected resistivity characteristics for thin film $\text{La}_{0.7}\text{Sr}_{0.3}\text{MnO}_3$ samples.

As can be seen, T_{MI} lies at slightly larger temperatures than T_C , which correspond to the general behavior for LSMO. Understanding why T_{MI} and T_C do not coincide perfectly has led to several investigations. Possible explanations involve factors such as polaron formation, Jahn-Teller distortions, oxidizing conditions or strain [34, 35]. Today it is commonly accepted that the double exchange mechanism cannot provide a complete description of the electrical transport in doped manganites alone, but it is still regarded as the main mechanism.

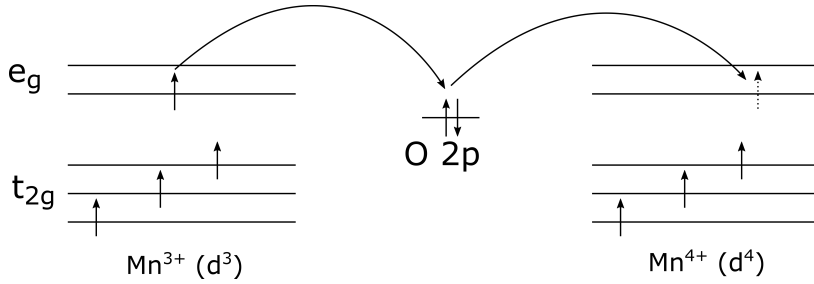


Figure 2.2: Illustration of the double exchange mechanism responsible for many of the transport properties in LSMO.

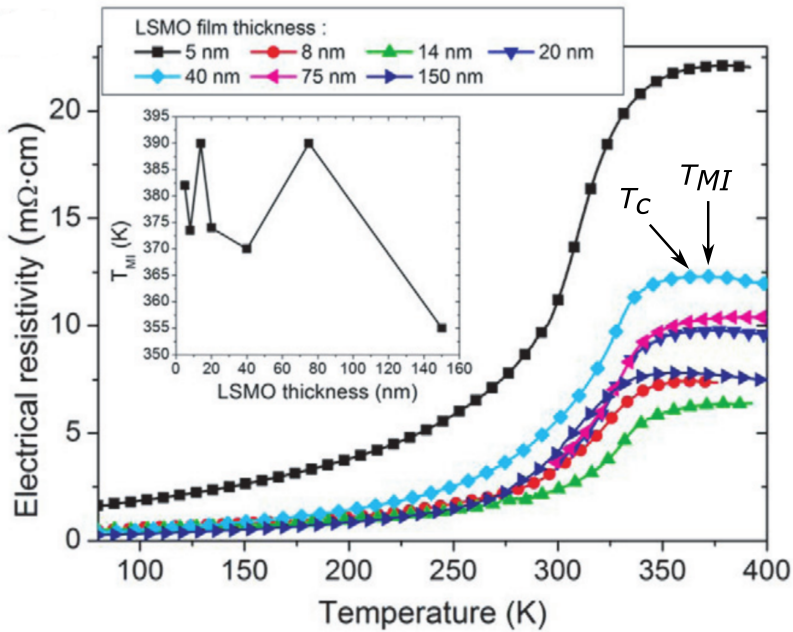


Figure 2.3: Typical resistivity characteristics for $\text{La}_{0.7}\text{Sr}_{0.3}\text{MnO}_3$ grown on (001)-oriented STO substrates. The metal-insulator transition temperature (~ 370 K) and the Curie temperature (~ 360 K) are marked for the 40 nm sample. The inset summarizes the T_{MI} values for the other samples. Adapted from [33].

2.1.3 Effect of Doping Concentration

Modifying the doping concentration of Sr^{2+} in LSMO can give rise to varying degrees of magnetic orderings or transport states. Table 2.1 summarizes different doping regimes and the corresponding properties. As can be seen, LSMO is only metallic for doping concentrations in the range $0.2 \leq x \leq 0.5$, and the maximum T_C value is reached between $x = 0.3$ and $x = 0.35$. Doping within this range also ensures the lowest resistivity values and highest metal-insulator transition temperatures. The ideal doping level is often referred to as $x = 1/3$, where bulk LSMO is a 100 % spin-polarized half-metal and has a $T_C \sim 370$ K [36]

For doping concentrations $x < 0.5$ the conduction band is more than half filled and is referred to as hole-doped (electron-doped for $x > 0.5$). This means that holes are the dominant charge carriers in the half-metallic state [29]. Taking $x = 0.3$ or $\text{La}_{0.7}\text{Sr}_{0.3}\text{MnO}_3$ as an example, theoretical considerations implies that there are 0.3 holes/unit cell.

Table 2.1: Overview of the electrical transport and magnetic ordering at different doping levels of $\text{La}_{1-x}\text{Sr}_x\text{MnO}_3$. Adapted from [28, 37].

Doping	Transport	Magnetic ordering
$x \leq 0.1$	insulating	A-type antiferromagnetic
$0.2 \leq x \leq 0.5$	metallic	ferromagnetic
$0.5 \leq x \leq 0.75$	insulating	CE-type antiferromagnetic
$0.75 \leq x \leq 0.85$	insulating	C-type antiferromagnetic ferromagnetic
$0.9 \leq x \leq 1.0$	insulating	G-type antiferromagnetic

2.1.4 The Colossal Magnetoresistance Effect

A contributing element to the popularity of manganites, is the fact that they exhibit the colossal magnetoresistance effect (CMR). Generally, magnetoresistance is the property of a material to change its resistance by the application of an external magnetic field. This effect was first discovered and explained by William Thomson in 1856 [38]. During Thomson's initial experiments, he was never able to observe a larger change than a decrease of about 5 % [39]. In contrast, mixed valence manganites were found to display resistances changing by several orders of magnitude during the 1980s. As an example, Jin *et al* measured magnetoresistances on the order of 1000 % in $\text{La}_{1-x}\text{Ca}_x\text{MnO}_3$ (LCMO) at 6 T [40]. Furthermore, the proposed mechanism for the large changes was fundamentally different from the ordinary effect. Naturally this discovery received attention from a researches all over the globe, who have hoped to utilize the effect for applications such as magnetic sensors and spintronics [41]. To distinguish the newly discovered type of magnetoresistance from the first, the term colossal was added and the CMR effect was born.

The existence of the CMR effect in LSMO can be explained by the double exchange mechanism and its dependence on spin alignment. Close to T_C , the magnetization decreases rapidly as the parallel alignment of spins becomes less

pronounced. As explained previously, this also suppresses the carrier hopping, and leads to an increased resistance. By exposing the material to an externally applied magnetic field, the spins realign to a parallel configuration. In essence the hopping rate increases and the resistance drops, hence a CMR effect is observed.

Quantitatively the CMR effect is measured as the relative ratio between the resistance in an applied field, $R(H)$, and at zero field, $R(0)$. In the literature comparing absolute values of the CMR ratio can be a bit problematic as the utilized formulas tend to vary. One of the most common definitions that is also used in this work is

$$MR = \frac{R(H) - R(0)}{R(H)}. \quad (2.1)$$

Using this formula the magnetoresistance becomes negative if an applied field induces a decreased resistance.

2.2 BaTiO₃

In this work BTO was used as the ferroelectric material in the heterostructures, hence a short overview is given below. Since its discovery, BTO has been one of the most studied ferroelectric materials because of its simplicity and high degree of symmetry [42]. Today BTO is not only used for research purposes, but has been utilized in various electronic applications such as multilayer capacitors, positive temperature coefficient (PTC) thermistors, piezoelectric transducers and several other electro-optic devices [43, 44].

In its cubic and paraelectric phase, BTO is a centrosymmetric perovskite with the general ABO₃ ($Pm\bar{3}m$) formula. It has Ba²⁺ at the A-sites (corners), Ti⁴⁺ at the B-site (center) and O²⁻ at the face centers [45]. The cubic phase is shown in Fig. 2.4a with an octahedral symmetry of the oxygen atoms. In its bulk form, a first order phase transition occurs at 393 K, where the unit cell is distorted along one of the main axes and becomes tetragonal [47]. An example of the tetragonal unit cell ($P4mm$) is shown in Fig. 2.4b. As opposed to the cubic phase, the tetragonal phase is not centrosymmetric, which gives rise to ferroelectricity. Going from the cubic to the tetragonal state, the cations (predominately Ti⁴⁺) are displaced with respect to the oxygen atoms, and a spontaneous electrical polarization results along the axis of elongation. In accordance with the requirements for any ferroelectric, the application of an external electric field may switch the direction of the displacement so that the polarization is reversed.

In addition to the tetragonal state at room temperature, two other ferroelectric phases exist at lower temperatures [48]. If the temperature is decreased to 278 K, the unit cell becomes orthorhombic ($Amm2$), which means that it is elongated along a face diagonal ([011]-direction). Further drops in temperature results in a rhombohedral phase ($R3m$) at 183 K, where the structure is elongated along a body diagonal ([111-direction]). Schematic representations of the distorted unit cells in the orthorhombic and rhombohedral phase are shown in Fig. 2.4c and 2.4d respectively.

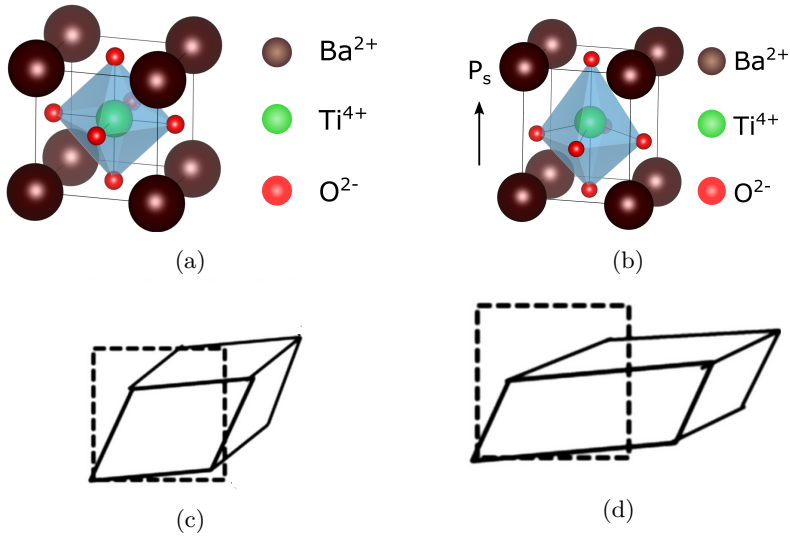


Figure 2.4: The cubic paraelectric phase of BTO is shown in (a), and the tetragonal ferroelectric phase in (b). The resulting spontaneous polarization for the tetragonal phase is shown, but the displacements of the atoms are greatly exaggerated for illustrative purposes. Schematics of the orthorhombic and rhombohedral phases are shown in (c), and (d) and were taken from [46].

The phase diagram for BTO is shown in Fig. 2.5 and summarizes the mentioned transitions and phases. An important feature of this diagram is that each phase transition slightly changes the lattice parameters.

2.3 Multiferroic Materials

During the last decade, increasing scientific interest has been given to so-called multiferroic materials exhibiting at least two out of five ferroic orders: ferroelectricity, ferromagnetism, antiferromagnetism, ferroelasticity or ferrotoroidicity [49]. In this treatment the focus will be on materials with ferroelectric and (anti)ferromagnetic properties.

By itself, the mere existence of two or more ferroic orders is not necessarily useful for applications. However, if for example the ferroelectric and ferromagnetic properties are strongly coupled as a result of the magnetoelectric (ME) effect, many potential applications can be imagined. The following sections give an overview of the magnetoelectric effect and related materials.

2.3.1 The Magnetoelectric Effect

In short, the ME effect can be explained as the appearance of an electric polarization \mathbf{P} by the application of a magnetic field \mathbf{H} . Analogously, the application of

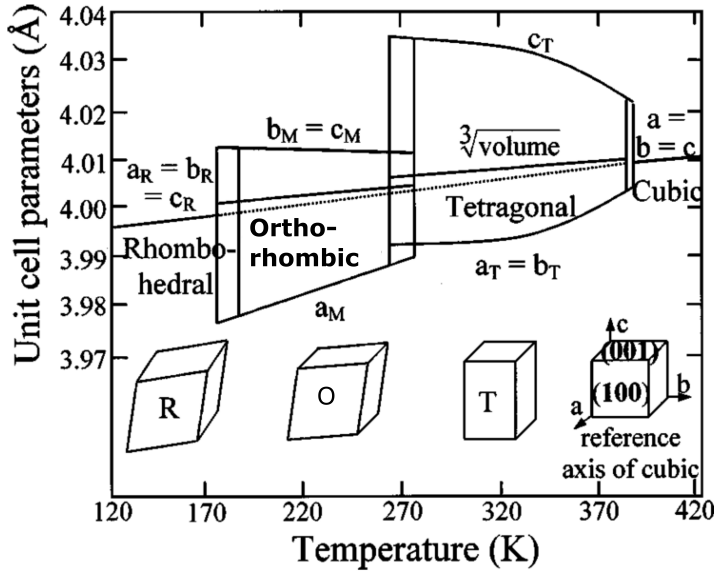


Figure 2.5: Phase diagram showing the variation of crystal structure and lattice parameters for BT0 as a function of temperature. Adapted from [19].

an electric field \mathbf{E} can induce a magnetization \mathbf{M} [12, 50, 51].

The first signs of this effect was observed in 1888 by Röntgen when he discovered that a dielectric became magnetized when put in motion in an electric field [52]. 17 years later, the reverse effect was observed by Wilson [53]. In 1894 Pierre Curie predicted the intrinsic ME effect in stationary crystals based on symmetry considerations [12, 54]. During the following years and even decades, none of the experiments conducted to demonstrate the ME effect were successful. Dzyaloshinskii was the first to observe both the direct and converse ME effect, when he studied single crystals of antiferromagnetic Cr_2O_3 in 1961 [55].

Multiferroic ME materials are commonly divided into single-phase materials [16, 56–58] and composites [59–61]. Initially, the majority of the researched materials were single phase compounds. Subsequently, the focus was shifted towards two-phase composites, multi-phase laminates and most recently thin film heterostructures [59]. The following parts highlight the differences between single-phase and multi-phase ME materials.

Single Phase Compounds

Since the first observation of the magnetoelectric effect in Cr_2O_3 , over ten different single phase ME compounds have been investigated to a large extent. The ME effect in such compounds can be explained as an intrinsic effect where two ferroic properties are connected directly. Based on Landau theory, an expansion of the free energy $F(\mathbf{E}, \mathbf{H})$ can be used to describe the ME effect in single phase compounds.

For a system with an applied magnetic field H and an electric field E whose i th components are denoted by E_i and H_i , the expression of the free energy becomes [12, 62]:

$$F(\mathbf{E}, \mathbf{H}) = -P_i^S E_i - M_i^S H_i - \frac{1}{2} \epsilon_0 \epsilon_{ij} E_i E_j - \frac{1}{2} \mu_0 \mu_{ij} H_i H_j - \alpha_{ij} E_i H_j - \frac{1}{2} \beta_{ijk} E_i H_j H_k - \frac{1}{2} \gamma_{ijk} H_i E_j E_k - \dots \quad (2.2)$$

In the first two terms on the right hand side, P^S and M^S denote the spontaneous polarization and magnetization respectively. The third term describes the electrical response from an electric field and the fourth term the magnetic equivalent. The quantities ϵ_0 and μ_0 are the permittivity and permeability of free space, whereas $\epsilon_{ij}(T)$ and $\mu_{ij}(T)$ are second-rank tensors describing the relative permittivity and permeability respectively. The fifth term is perhaps the most important part, which describes the linear dependence between the electric and magnetic field through a magnetoelectric coupling factor $\alpha_{ij}(T)$. The two final terms represent higher order contributions via the magnetoelectric coupling coefficients β_{ijk} and γ_{ijk} , which are third-rank tensors.

By differentiating equation (2.2), the polarization can be found as

$$P_i(\mathbf{E}, \mathbf{H}) = -\frac{\partial F}{\partial E_i} = P_i^S + \epsilon_0 \epsilon_{ij} E_j + \alpha_{ij} H_j + \frac{1}{2} \beta_{ijk} H_j H_k + \gamma_{ijk} H_i E_j + \dots \quad (2.3)$$

Similarly, the magnetization becomes

$$H_i(\mathbf{E}, \mathbf{H}) = -\frac{\partial F}{\partial H_i} = M_i^S + \mu_0 \mu_{ij} H_i H_j + \alpha_{ij} E_i + \beta_{ijk} E_i H_j + \frac{1}{2} \gamma_{ijk} E_j E_k + \dots \quad (2.4)$$

Oftentimes, only the linear term is included when describing the ME effect. This results in two simple expressions showing that a magnetic field can induce a change in polarization, and that an electric field can induce a change in magnetization:

$$\Delta P \approx \alpha_{ij} \Delta H \quad (2.5)$$

$$\Delta M \approx \alpha_{ij} \Delta E \quad (2.6)$$

The ME coupling factor α_{ij} appearing in these two expressions is often taken as a measure of the coupling strength when comparing different materials. Normally, it is given in the SI units sm^{-1} . Another commonly cited quantity is the magnetoelectric voltage coefficient $\alpha_E = \partial E / \partial H$, normally given in the units $\text{Vcm}^{-1} \text{Oe}^{-1}$ [63].

Today, the most promising candidate for single-phase multiferroic devices is BiFeO_3 (BFO) [64]. This material is a perovskite with both ferroelectric and antiferromagnetic properties that are coupled even at room temperature² [65]. The

² BiFeO_3 has a Néel temperature of 640 K and a Curie temperature of 1100 K in its rhombohedral state.

first publications on BFO focused on bulk crystals, but thin films have become more popular recently [66]. Although single-phase compounds such as BFO seem promising, there are still no known single-phase multiferroics with strong ME coupling at room temperature. Fundamentally, there are several possible reasons as to why there are so few single-phase multiferroics. In an article back in 2000, Hill investigated a few possible explanations such as symmetry incompatibilities, electronic differences and what she called “ d^0 -ness” [61]. The latter proposal was considered to be the most important factor. More specifically the “ d^0 -ness” involved the fact that the B cation in ferroelectric oxides mostly have a formal charge corresponding to the d^0 configuration, while magnetic moments are dependent on partially filled d -orbitals.

To circumvent these problems researchers started looking towards multiferroic composites, which is the topic of the next part.

2.3.2 Multi-Phase Compounds and Composites

By combining a ferromagnetic and ferroelectric material, a multi-phase multiferroic material may result. Intrinsically neither of the phases are multiferroic, but the interaction between them can lead to an extrinsic ME effect. As opposed to single-phase compounds, this makes the choice of materials more flexible and allows both the ferromagnetic and ferroelectric material to be chosen so that they have optimal properties for the desired application. Due to this flexibility, researchers have found composites that exhibit giant magnetoelectric response even at room temperature [67].

The first composite ME material was grown by van Suchtelen, van den Boomgard *et al* during the 1970’s [68]. They combined ferroelectric BTO and ferromagnetic CoFe_2O_4 in an eutectic composite by unidirectional solidification. The ME voltage coefficient was found to be as high as $130 \text{ mVcm}^{-1}\text{Oe}^{-1}$. Even today this is well above values for known single-phase compounds, which is normally in the range $1 - 20 \text{ mVcm}^{-1}\text{Oe}^{-1}$ [69].

Most of the ME composites investigated after the original discovery were based on two-phase bulk ceramics. Two-phase composites have a specific notation used to describe the phase connectivity, e.g. 0-3, 2-2, 1-3 etc [70]. In this scheme, the numbers denote the dimensionality of each phase, where for example 0-3 implies particles embedded in a matrix, while 2-2 indicates a layered structure. Even though many different combinations and materials were researched during the 20 first years following the original discovery, the complex fabrication and slow progress made people lose interest in the field. A simpler and cheaper sintering technique was proposed in the 1990s [71, 72], but the products had lower ME coefficients than the previously fabricated eutectic composites. Because of this, the most recent wave of research was delayed until 2000, as new and advanced growth procedures such as pulsed laser deposition (PLD) and molecular beam epitaxy (MBE) became more widespread. After the appearance of these techniques, thin film ME heterostructures with nanometer precision have become the most promising candidate for practical applications.

In 1972 van Suchtelen described the ME effect in composites as a product tensor

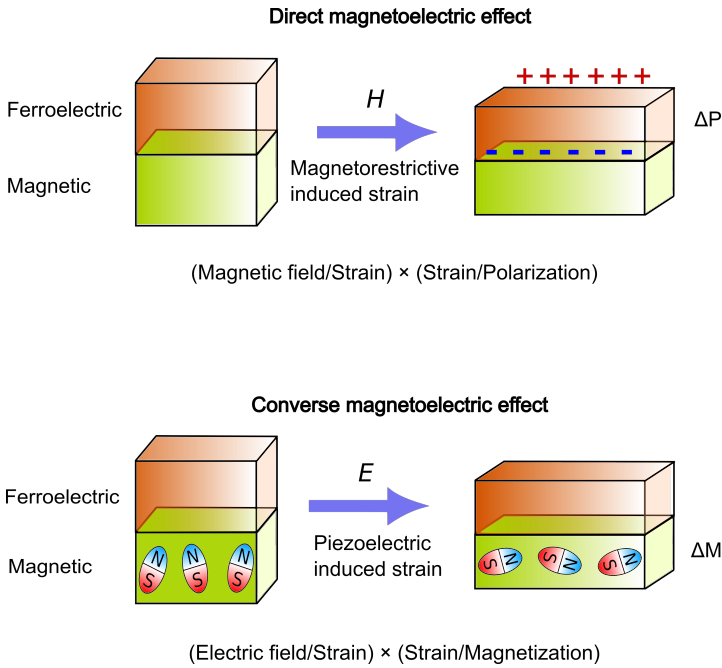


Figure 2.6: A schematic representation of the ME effect in composite multiferroic materials. The ME coupling is explained by induced strain from the magnetorestrictive and piezoelectric effect.

property resulting from interactions between the involved phase [73]. In ferromagnetic/ferroelectric composites the ME effect can be explained as the product of the magnetorestrictive effect (magnetic/mechanical) in the magnetic phase, and the piezoelectric effect (mechanical/electrical) in the ferroelectric [74]. Qualitatively, this is often written as

$$\text{Direct ME Effect} = \frac{\text{magnetic}}{\text{mechanical}} \times \frac{\text{mechanical}}{\text{electric}} \quad (2.7)$$

$$\text{Converse ME Effect} = \frac{\text{electric}}{\text{mechanical}} \times \frac{\text{mechanical}}{\text{magnetic}} \quad (2.8)$$

According to this model, the coupling happens via elastic interaction and is considered to be strain-mediated.

An illustration the ME effect in a composite of a ferromagnetic and ferroelectric material can be seen in Fig. 2.6. The direct ME effect is illustrated at the top where an applied magnetic field H induces strain in the magnetic layer (magnetorestrictive effect), which is transferred mechanically to the ferroelectric layer. In turn, this induces an electric polarization P as a consequence of the piezoelectric effect. The bottom part illustrates the converse ME effect, where an applied electric field E induces strain in the ferroelectric layer which is transferred and converted to a

magnetization change in the magnetic layer.

As was shown in equation (2.5) and (2.6), the relationship between the applied magnetic field (electric field) and induced polarization (magnetization) is approximately linear for single-phase compounds. For composite materials however, the strain coupling is related via a square dependence of the field strength. Therefore a more general definition of the magnetoelectric coefficient is employed:

$$\alpha = \left| \frac{\partial E}{\partial H} \right| \quad (2.9)$$

When magnetoelectric coefficients are reported for composite multiferroics, this definition is normally used in the calculations.

Today the largest known ME coefficients in composites have been shown to reach as high as $92 \text{ Vcm}^{-1}\text{Oe}^{-1}$, and up to $16\,000 \text{ Vcm}^{-1}\text{Oe}^{-1}$ at resonance frequencies for a three-phase composite made of $\text{Pb}(\text{Zr},\text{Ti})\text{O}_3$ ceramic fibers, a phosphor-copper-sheet unimorph and a NdFeB magnet [75]. Theoretical investigations have even suggested that there is no upper bound for the ME coefficient, but it was pointed out that this is not necessarily synonymous with infinite performance [76]. Since the ME properties are dependent on extrinsic coupling, finding ways to maximize the indirect coupling has become the most important issue. In this regard, the biggest challenges for nano-structured multiferroic composites are control of growth and interfaces.

2.3.3 Magnetoelectric Random Access Memory

Possible applications for multiferroic materials include sensors, transformers, gyrators and microwave devices [63]. If multiferroic materials are realized with a sufficiently strong ME coupling, another potential application is magnetoelectric RAM (MERAM) [14]. Ideally MERAM would combine the best features associated with two existing memory technologies: ferroelectric RAM (FeRAM) and magnetic RAM (MRAM). One of the drawbacks with FeRAM, is that the reading process is destructive, implying that the bit content must be rewritten continuously. As for MRAM, one of the main concerns is the high power consumption related to the writing operation, which utilizes relatively large magnetic fields. The following part explains the working principles of MERAM and its potential advantages to the current memory technologies.

An illustration of a possible MERAM element based on thin films is shown in Fig. 2.7. The green layer on top of the electrode is multiferroic (ferroelectric-antiferromagnetic), and has a strong ME coupling. Even though a single phase multiferroic material is assumed in this example, a more realistic approach would be to grow an antiferromagnetic film on top of a ferroelectric³. Both of the blue layers are ferromagnetic, but the direction is assumed to be fixed in the top layer and free to change in the bottom layer. Because of the giant magnetoresistance effect, the resistance takes on different values depending on the relative orientation of the magnetization in these layers [10]. The resistance is either low in the parallel

³As with a single phase compound, this would also require the ME coupling to be strong.

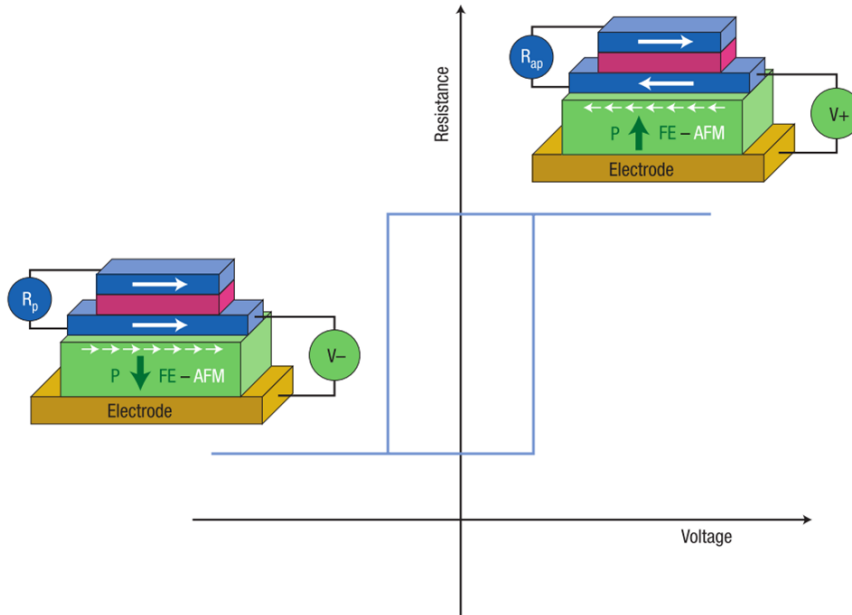


Figure 2.7: Illustration of a possible MERAM memory device based on a multiferroic material with strong ME coupling. The two blue layers are ferromagnetic with the direction of the magnetization indicated by large white arrows. The green layer is both antiferromagnetic and ferroelectric, where the electrical polarization is indicated by large green arrows and the spin direction at the interface by small white arrows. Taken from [14].

configuration, R_P , or high in the anti-parallel configuration, R_{AP} . These differences correspond to a “0” and “1”, which enables storage of information similarly to existing memory technologies.

An important requirement is that the direction of the magnetization in the bottom ferromagnetic layer must be linked to the orientation of the antiferromagnet. This connection may take place at the interface due to exchange bias. Owing to the ferroelectric properties, the multiferroic layer also has an electric polarization (large green arrow), which can be switched by the application of an external voltage. If the ME coupling is sufficiently strong, switching the direction of the polarization may flip the spins in the antiferromagnetic phase. Consequently, the domains in the bottom ferromagnet are also changed. Effectively this would allow magnetically stored bits to be written by an electric voltage instead of a magnetic field. The blue curve illustrates the hysteresis behavior for the resistance and the applied voltage.

In summary, MERAM may avoid the destructive reading process in FeRAM, and the high energy demands associated with magnetic writing in MRAM.

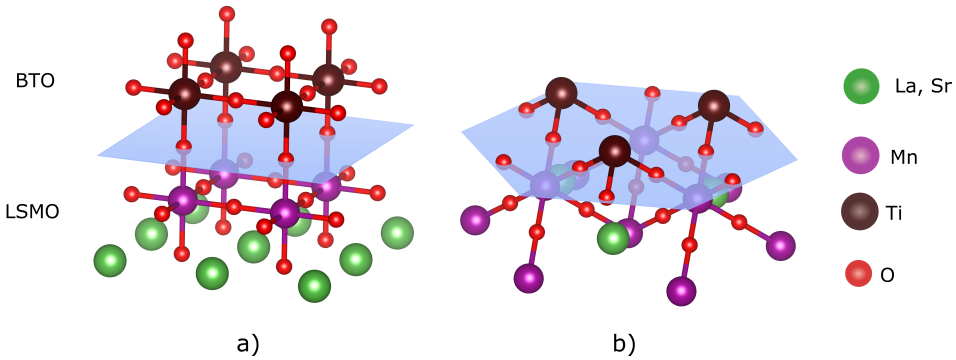


Figure 2.8: Illustration of the interface region for a (001) and (111)-oriented BTO/LSMO heterostructure in (a) and (b) respectively. The BTO layer is at the top while the LSMO layer is at the bottom. One oxygen atom is shared per unit cell across the interface for the (001)-oriented structure, while three oxygen atoms are shared at (111) interfaces.

2.3.4 (111)-Oriented BTO/LSMO Heterostructures

In this work the unconventional (111) orientation was the main difference compared to similar studies. The aim of this section is to highlight why it can be interesting to investigate possible strain-induced magnetoelectric coupling in such heterostructures.

The oxygen atoms forming the octahedra in perovskites are important both for the ferroelectric and ferromagnetic properties. During epitaxial growth of BTO/LSMO-based heterostructures, the oxygen atoms at the interface form a connection between the ferroelectric and ferromagnetic phase. In BTO, there are two events that may induce displacements of the oxygen atoms. One possibility, is that a change in polarization slightly shifts the position of the oxygen atoms due to the piezoelectric properties. Another possibility is that one of the phase transitions induce fractional changes of the lattice parameters, which also leads to small displacements. For epitaxial interfaces such displacements may be transferred to the LSMO layer, i.e. the layers become strain-coupled. Specifically, the tilt angle of the distorted octahedra in LSMO may change, or the O-Mn-O bonds may be compressed or elongated. Both of these events would alter the hopping probability of the itinerant carriers due to the double exchange mechanism. Similarly, the magnetic properties may be changed via strain-coupling to the BTO layer. Essentially this implies that displacements originating in the BTO layer may be transferred and used to control the properties of LSMO.

Normally thin film heterostructures are grown with a (001) orientation, where only one oxygen atom is shared at the interface per unit cell. This has been illustrated in Fig. 2.8a. One of the advantages of (111)-oriented heterostructures, is that three oxygen atoms are shared per unit cell, as shown in Fig. 2.8b. Qualitatively, an increased number of shared oxygen atoms suggest a stronger coupling.

Furthermore, the orbital structure of the shared oxygen atoms at (111) interfaces are dissimilar as opposed to the equivalent top/bottom atoms that are shared for the (001) orientation. This may also increase the coupling strength. Another advantage of (111)-oriented perovskites, is that they have been demonstrated to be able to form high quality interfaces with topological insulators, semiconductors and other ferroelectrics [77]. This ability can mostly be attributed to their hexagonal symmetry, and it is therefore harder to achieve the same quality for cubic (001)-oriented perovskites.

2.4 State of the Art

Since the discovery of LSMO, researchers have tried to increase its usefulness by the use of different growth techniques, doping concentrations, film thicknesses and sample structures. The first part of this section presents a handful of recent studies with the aim of illustrating how LSMO can be manipulated to increase its usefulness in future devices. These manipulations are not necessarily related to a ME coupling, but the second part takes a closer look at such coupling in BTO/LSMO heterostructures.

2.4.1 LSMO Transport Properties

Increasing the metal-insulator transition temperature, or improving the overall resistivity characteristics can be beneficial for various electronic applications. In one study, the effect of growing 10 – 50 nm LSMO thin films on top of a BTO/CeO₂/YSZ⁴/Si multilayered structure was investigated [78]. Varying the BTO thickness in the range 5 – 60 nm was observed to have a major impact on both the resistivity and the T_{MI} values. The optimal BTO thickness of 20 nm resulted in T_{MI} values close to 390 K for 50 nm LSMO films, which is 10 – 40 K higher than for bulk samples of LSMO grown on STO. The proposed explanation was large compressive in-plane strain. Such improvements can broaden the range of operating temperatures. These findings were not explained by a ME coupling, but still show that the properties of LSMO can be influenced by other material layers.

The opportunity to dope LSMO so that it becomes a spin-polarized half-metal, makes it an attractive choice for spintronic devices. In tunneling magnetoresistance (TMR) devices the spin is conserved during tunneling, which implies that the tunneling probability is largest for spin-polarized materials [79]. Therefore, properly doped LSMO is a suitable material for magnetic TMR structures and devices [80]. Moreover, LSMO has proved to be a promising material for spin valves in conjunction with organic semiconductors [81–83], and it has been shown to be able to inject and transfer spin-polarized currents in structures with carbon nanotubes [84].

One of the main challenges related to potential applications based on the CMR effect in LSMO, is that high fields (> 1 T) are required. Because of this, an ongoing research strives to achieve low field magnetoresistance (LFMR). By the

⁴ YSZ is an abbreviation for the ceramic Yttria-stabilized zirconia

growth of LSMO:ZnO self-assembled vertically aligned nanocomposites on (001) STO substrates, Chen et al. obtained magnetoresistance values of 17.5% and 30% at 40 K and 154 K respectively [85]. These values were measured at 0.3 T and were up to 12 times larger than in normal epitaxial LSMO films. In another study conducted by Majumdar et al., they obtained similar values around 17% by the use of MgO substrates which introduced structural defects and grain-boundaries [86]. Although totally different approaches were used, the enhanced MR was attributed spin-polarized tunneling across artificially introduced grain boundaries in both of the given examples.

2.4.2 ME Coupling in BTO/LSMO Heterostructures

Similarly to various recent studies of ME multiferroics, BTO/LSMO heterostructures with planar interfaces have received the most attention. Even though the interfacial area is not maximized for such heterostructures, the value of having homogeneously distributed strain coupling is considered as a large advantage [23]. Despite the increased popularity of planar interfaces, there is a limited amount of studies based on heterostructures with coupling between two thin films. For BTO/LSMO heterostructures, one of the materials is often used in its bulk form as a substrate while the other is grown on top as a thin film. As an example, Lee et al. studied strain coupling in 50 nm thin films of $\text{La}_{0.67}\text{Ca}_{0.33}\text{MnO}_3$ epitaxially grown on top of (001)-oriented single-crystalline BTO [19]. They observed two discontinuous jumps for the resistivity at certain temperatures in the range between 20 – 400 K. A 12% jump was detected around 280 K and a 10% jump in the proximity of 185 K. As these temperatures lie close to the orthorhombic and rhombohedral phase transitions for BTO, the jumps were attributed induced strain effects in the LSMO layer caused by the changes of the BTO lattice parameters. Similar behavior was observed around the same temperatures for the magnetization.

More recently, Eerenstein et al. went on to measure the ME coupling in similar structures [23]. They fabricated samples of 40 nm LSMO on top of (001)-oriented bulk BTO substrates and observed a large change in magnetization around the rhombohedral \rightarrow orthorhombic phase transition during heating. Additionally they reported electrically induced giant, sharp and persistent magnetic changes corresponding to a ME coefficient of $\alpha = 2.3 \times 10^{-7} \text{ sm}^{-1}$. Using X-ray diffraction, they confirmed that the strain coupling took place via ferroelastic non-180° BTO domains.

Researchers have also grown heterostructures where both the BTO and LSMO layer were deposited as thin films [87]. As opposed to the previous examples, no discontinuous jumps were observed when measuring the magnetization for 19 nm BTO grown on top of 10 – 50 nm LSMO. On the other hand, they did observe a large ($> 10\%$) electrical modulation of the magnetization at room-temperature. The effect was induced by polarization reversal in BTO, and the measurements indicated that the effect was limited to a thin LSMO layer of about 3 nm at the interface. Another group fabricated a bilayer structure of 250 nm LSMO and 330 nm on top of (001)-oriented LaAlO_3 substrates [88]. Their investigations showed that the ferroelectric and ferromagnetic properties were maintained at their intrinsic levels,

and a magnetoelectric voltage coefficient α_E was measured to $140 \text{ mV/cm}^{-1} \text{Oe}^{-1}$ at room temperature.

Nowadays one of the major challenges associated with oxides and other functional materials, is that the integration with current silicon technology must be feasible. In an attempt to solve this problem, Singamaneni et al. grew epitaxial bilayers of 25–100 nm BTO and 217 nm LSMO on Si (001) substrates [89, 90]. As with the previous example, no discontinuous jumps were observed for the magnetization in the relevant temperature range. A suggested explanation was that the films were clamped to the substrate. However, when comparing LSMO/Si samples without BTO they saw an almost 2-fold higher magnetic coercive field, a 3-fold reduction in saturation magnetization and improved squareness. Strong in-plane spin pinning of the ferromagnetic layer induced by BTO was believed to be the cause. These observations are particularly important since they show that magnetic properties can be controlled by a ferroelectric layer and incorporated with current Si technology.

2.5 The Hall Effect

The Hall effect is a fundamental phenomenon that can be observed in most electronic materials. Nowadays, the effect is exploited in various sensing technologies, or in transducers which may be found in automobiles, computers, industrial controls and consumer devices [91, 92]. Moreover, Hall measurements is a widespread characterization method which can provide valuable information about the transport properties for materials such as metals and semiconductors.

The following sections give an overview of the physics related to the ordinary Hall effect, in addition to the anomalous Hall effect which complicates the situation for ferromagnetic materials.

2.5.1 One-Band Approximation

In order to perform qualitative studies a one-band model is often sufficient, and it simplifies the calculations considerably compared to a two-band model to be discussed in section 2.5.2. A one-band approximation is mostly valid for simple metals with a spherical Fermi surface and only one type of carriers. This approximation also applies to semiconductors with a large excess one dopant type.

The first discovery of the ordinary Hall effect was made by Edwin H. Hall in 1879 [93]. He explained the effect as a result of an interaction between moving charge carriers and an externally applied magnetic field, B . This interaction is governed by a combination of electric and magnetic forces, commonly referred to as the Lorentz force [94]:

$$\mathbf{F} = q(\mathbf{E} + \mathbf{v} \times \mathbf{B}) \quad (2.10)$$

In this equation q is the elementary charge, \mathbf{v} the velocity of the particle and \mathbf{B} an applied magnetic field. To avoid confusion with signs, the following treatment

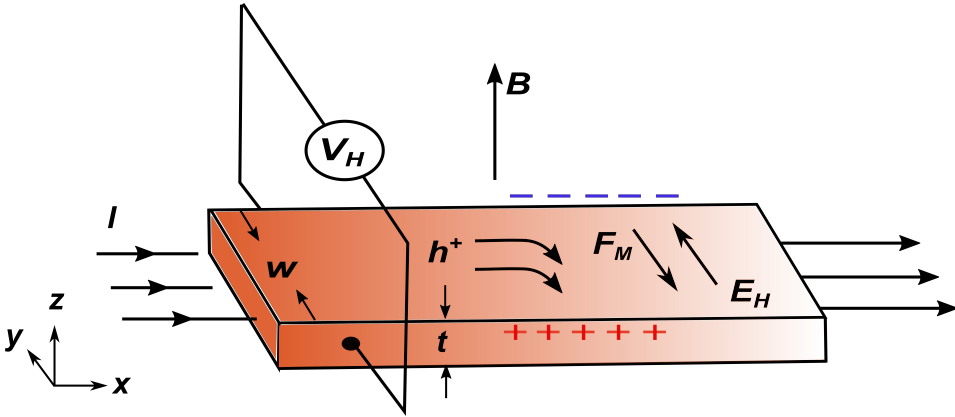


Figure 2.9: The Hall effect is illustrated by a hole moving in a magnetic field \mathbf{B} , perpendicular to the current direction. Due to the Lorentz force, a charge builds up on the bottom side and a field is set up in the transverse direction. By measuring the Hall voltage V_H across the sample, parameters like the carrier density n and mobility μ can be deduced.

is based on a positive hole moving in a magnetic field perpendicular to the current direction, as illustrated in Fig. 2.9.

By applying the right hand rule, it can be seen that the magnetic term in equation (2.10) generates a downwards force F_M . Consequently, holes start to pile up on the bottom side so that a positive charge builds up, which induces an electric field E_H . As the system reaches equilibrium, the generated force from the electric field F_E is equal to the magnetic force F_M . Given the setup in the figure, the vector notation can be dropped and the following expressions are obtained:

$$F_E = F_M \quad (2.11)$$

$$qE_H = qv_d B_z \quad (2.12)$$

$$E_H = v_d B_z \quad (2.13)$$

$$\frac{V_H}{w} = v_d B_z \quad (2.14)$$

In equation (2.12)-(2.14) v_d denotes the drift velocity of the holes at steady-state, w the width of the sample, and E_H and V_H the Hall field and voltage respectively. The carrier density n can be determined using a general expression for the current density $J_x = nqv_d$ [94]. In practice the current I_x is often the known quantity, which when substituted for J_x gives

$$I_x = nqv_d A \implies v_d = \frac{I_x}{nqt}, \quad (2.15)$$

where A is the area of the cross-section and t the thickness. Using equation (2.15)

to insert for v_d in equation (2.14) then yields

$$V_H = \frac{I_x}{nqt} B_z \quad (2.16)$$

This can be re-arranged to find an expression for the carrier density

$$n = \frac{I_x B_z}{qV_H t}. \quad (2.17)$$

Multiplying the above equation with the thickness t , all geometry dependent factors are removed and the sheet carrier density n_s ($n_s = nt$) is obtained,

$$n_s = \frac{I_x B_z}{qV_H} \quad (2.18)$$

Another commonly cited quantity is the Hall coefficient R_H [95], defined as

$$R_H = \frac{E_H}{J_x B_z} = \frac{1}{nq}. \quad (2.19)$$

When using the one-band model, the sign of the Hall voltage V_H or the Hall coefficient R_H indicates the sign of the carriers, i.e. holes or electrons.

One last important transport property is the carrier mobility μ . For materials with excess of one carrier type, the mobility can be related to the resistivity, ρ [95]:

$$\rho = \frac{1}{nq\mu} \quad (2.20)$$

Substituting ρ with the sheet resistance R_s ($\rho = R_s t$), and n_s for n , the following relation is obtained:

$$\mu = \frac{1}{qn_s R_s}. \quad (2.21)$$

Inserting for n_s in equation (2.21) gives a final expression for the mobility:

$$\mu = \frac{V_H}{R_s I_x B_z} \quad (2.22)$$

One reason the sheet carrier density n_s and sheet resistance R_s were used in the latter part, is that geometry factors such as the thickness t is removed. Additionally n_s and R_s can be related to measurable quantities found by van der Pauw's method. This will be explained more thoroughly in section 3.2.

2.5.2 Two-Band Model

For materials where both electrons and holes take part in the transport, a simple one-band model is insufficient. In such cases, the formulas obtained above for the carrier density, Hall coefficient and mobility are invalid. From the fact that the electrons and holes are located in different bands, a two-band model must be

evaluated. If the contributions from both carrier types are included, the current density can be written as a sum of two terms [95]

$$J = qn_e v_e + qn_h v_h \quad (2.23)$$

$$= q(n_e \mu_e + n_h \mu_h)E, \quad (2.24)$$

where $n_{e,h}$ denote the electron and hole densities, $v_{e,h}$ the velocities and $\mu_{e,h}$ the corresponding mobilities. From the definition of the resistivity ($\rho = E/J$) [95], equation (2.24) can be rearranged to find the resistivity

$$\rho = \frac{1}{q(n_e \mu_e + n_h \mu_h)}. \quad (2.25)$$

The Hall coefficient also becomes more complicated when two carrier types are present, and is defined as [96]

$$R_H = \frac{n_h \mu_h^2 - n_e \mu_e^2}{q(n_h \mu_h + n_e \mu_e)^2}. \quad (2.26)$$

An important point when working with the two-band model, is that neither the sign of the Hall coefficient nor the Hall voltage can be interpreted as an indication of the carrier charge. In practice Hall measurements based on a two-band model must be accompanied with band-structure calculations, and the mobility ratio μ_e/μ_h must be determined.

Even though the main carriers in LSMO are holes, electrons are also known to take part in the transport [97]. Therefore, a two-band model should be employed to fully capture the transport properties.

2.5.3 The Anomalous Hall Effect

Two years after Hall's original discovery, he observed that the force driving the electrons to one of the sides was ten times stronger in ferromagnetic iron than in nonmagnetic conductors [98]. His second discovery has later been acknowledged as the first observation of the anomalous Hall effect. Today this additional effect is known to be present to some degree in all ferromagnetic conductors.

Sometimes the transverse resistivity or Hall resistivity, ρ_{xy} , is reported separately from the overall resistivity. For non-ferromagnetic materials only the ordinary Hall coefficient contribute to this resistivity, but for ferromagnetic materials such as LSMO the anomalous Hall effect adds an additional term [20, 28]:

$$\rho_{xy}(B, T) = R_H(T)B + \mu_0 R_a(T)M(B, T). \quad (2.27)$$

The first term comes from the ordinary temperature dependent Hall coefficient $R_H(T)$ and its linear dependence on B . The second term describes the anomalous Hall effect where μ_0 is the vacuum permeability, $R_a(T)$ the anomalous Hall coefficient and $M(B, T)$ the magnetization. Previous investigations have shown that R_H is weakly temperature dependent in thin films, whereas the anomalous Hall

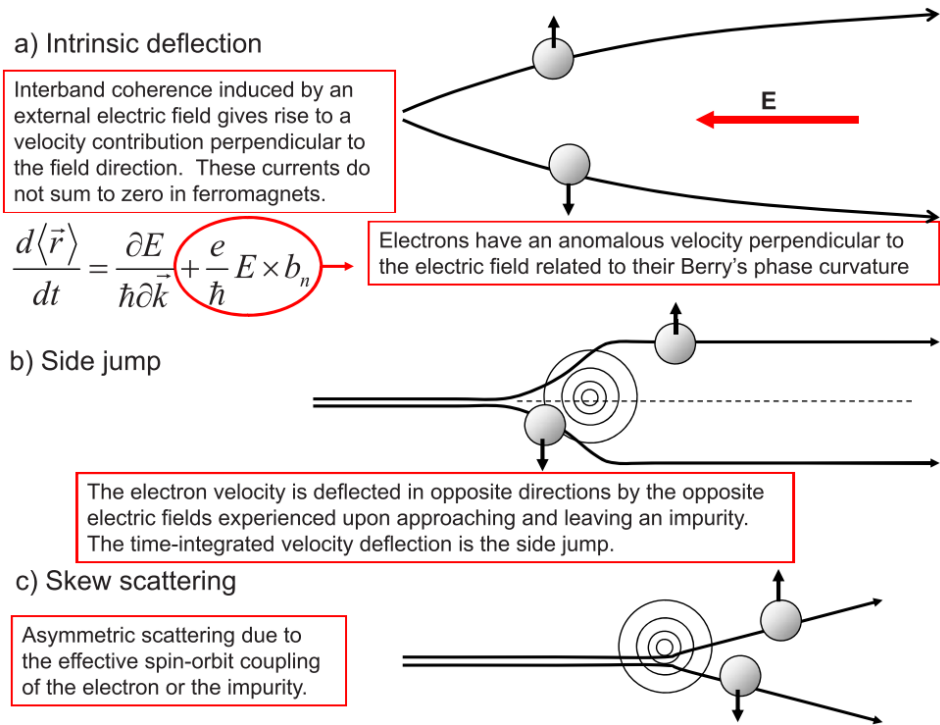


Figure 2.10: Overview of the three main theories explaining the anomalous Hall effect. (a) illustrates intrinsic deflections, (b) side jumps and (c) skew scattering. Taken from [99].

coefficient R_a shows a much stronger dependence, peaking slightly above the Curie temperature [97, 100].

The first theory explaining the anomalous Hall effect was proposed by Karplus and Luttinger in 1954 [101]. They showed that an externally applied electrical field may give the electrons an additional contribution to their group velocity, which is perpendicular to the direction of the field. It was found that this velocity contribution may be non-zero when summed over all occupied band states for ferromagnetic conductors. Effectively, this results in an additional intrinsic contribution to the Hall effect.

An alternative theory was developed by Smit, and involves spin-orbit interactions that causes asymmetric scattering from impurities [102, 103]. This mechanism is often called skew scattering and is an extrinsic effect. A similar extrinsic mechanism was described by Berger, and is based on side jumps by quasi-particles upon scattering from spin-orbit coupled impurities [104]. The first three main theories are summarized in Fig. 2.10. Today all of these theories are accepted as possible explanations and more advanced theories have built upon these [99].

Previous studies of the anomalous Hall effect in single crystals of manganites

have shown that the anomalous contribution is negative, while the ordinary Hall effect is positive (consistent with holes as main carriers) [105]. One study also found indications of skew scattering being the main contributor [106]. More recently, similar investigations have been done for thin film manganites, and one of these showed that both skew scattering and the side-jump mechanism are important for LSMO and LCMO [20]. These mechanisms are known to saturate at low temperatures or high fields, which allows the ordinary effect to be studied more easily in these regimes. The importance of this fact will become apparent in section 4.2.2.

3. Experimental

This chapter introduces the experimental techniques and methods that were developed in order to characterize the electrical transport properties of BTO/LSMO-based heterostructures. First an overview is given for the sample structures, followed by a review of van der Pauw's method which formed the basis for the electrical measurements. The latter parts cover preparation of gold contacts, wire bonding, electrical measurements, and data processing.

3.1 Sample Structures

The BTO/LSMO heterostructures investigated in this work were grown by pulsed laser deposition (PLD) on (111)-oriented SrTiO₃ substrates¹. An illustration of the sample structures can be seen in Fig. 3.1. The sample at the top was grown with a single layer of 10 nm LSMO, and was used as a reference when comparing the samples with additional BTO layers. The heterostructures at the bottom mainly differed by having varying BTO thicknesses or reversed orders of the LSMO and BTO layers. These heterostructures were chosen in order to examine trends, and to investigate a possible magnetoelectric effect via strain-coupling. For the remaining part of this thesis, samples with either BTO or LSMO on top are referred to as BTO/LSMO or LSMO/BTO respectively, and only the BTO thicknesses will be given specifically since the LSMO thickness was kept constant at 10 nm. Additionally, the general formula LSMO will refer to the exact composition studied in this work – La_{0.7}Sr_{0.3}MnO₃.

A series of samples with thicker BTO layers were also grown, but these were mostly used for testing purposes during the establishment of the technique. An overview of these structures can be found in appendix C. In this work the main focus was given to samples with thinner BTO layers, as these were expected to provide higher quality interfaces. Thinner samples also exhibited a large change in the coercive field around 105 K, possibly caused by a phase transition in the STO substrates².

¹The growth procedures were not performed as a part of this thesis.

²Determined in an unpublished study by Torstein Bolstad

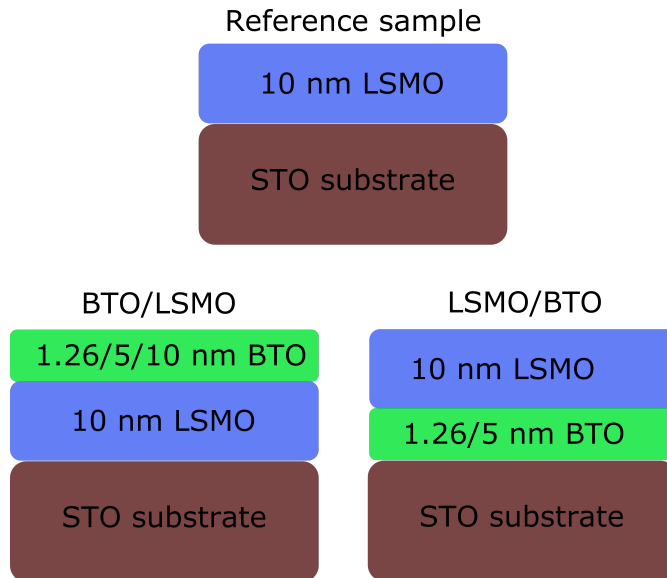


Figure 3.1: Illustration of the sample structures that were used to examine possible ferromagnetic-ferroelectric coupling. The top structure is a reference sample with a 10 nm layer of LSMO grown on the STO substrate. The BTO/LSMO samples to the bottom left have an additional top layer of either 1.26 nm, 5 nm or 10 nm BTO. The LSMO/BTO heterostructures to the bottom right have the order of the BTO and LSMO layers reversed so that LSMO is grown on top of BTO.

3.2 The Van Der Pauw Method

In 1958 Leo J. van der Pauw introduced a new method designed to improve resistivity and Hall measurements for samples with an arbitrary shape [107]. He argued the validity of this method if the following conditions are fulfilled [108]:

1. The contacts are at the circumference of the sample.
2. The contacts are sufficiently small.
3. The sample has a homogeneous thickness.
4. The surface of the sample is singly connected, implying that the sample can not contain isolated holes.

To be able to measure the mobility and carrier density properly using classical Hall bar geometries, a minimum of six are needed, as shown in Fig. 3.2. One of the advantages of van der Pauw's method is that only four contacts are required which allows simpler geometries to be used. Moreover, the corresponding calculations do not require geometry dependent parameters to be determined, such as sample width or distances between contacts [109].

3.2.1 Resistivity Measurements

Given an arbitrarily shaped sample with four contacts as shown in Fig. 3.3, the resistance $R_{12,34}$ can be found by applying a current I_{12} between contact 1 and 2 and measuring the voltage drop V_{34} from 3 to 4:

$$R_{12,34} = \frac{V_{34}}{I_{12}}. \quad (3.1)$$

Similarly $R_{23,41}$ can be calculated as:

$$R_{23,41} = \frac{V_{23}}{I_{41}}. \quad (3.2)$$

In real life, the samples to be measured are often square-shaped. For such geometries, a contact is made in each corner and the measurements are performed

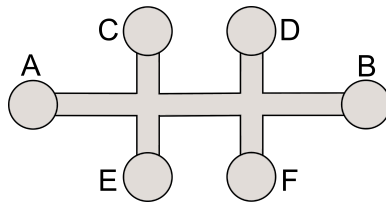


Figure 3.2: Illustration of classical Hall bar geometry where six contacts are needed to perform accurate measurements.

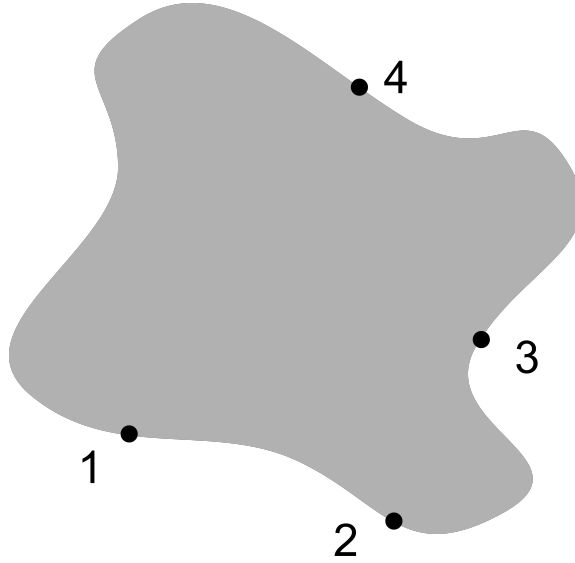


Figure 3.3: Illustration of an arbitrarily shaped sample with four contacts 1-4 to be used for van der Pauw measurements.

as illustrated in Fig. 3.4. First, the current is applied vertically and the voltage is measured across the opposite edge. In the next step, the same procedure is repeated when measuring horizontally. Analogously to equation (3.1) and (3.2), the resistances $R_{12,34}$ and $R_{23,41}$ can be calculated. From these two resistances, the resistivity ρ can be deduced from van der Pauw's formula [107, 108]

$$\exp\left(\frac{-\pi t R_{12,34}}{\rho}\right) + \exp\left(\frac{-\pi t R_{23,41}}{\rho}\right) = 1, \quad (3.3)$$

where t is the thickness of the measured sample. Sometimes this equation is given for the sheet resistance R_s rather than the resistivity ρ . From the relation $\rho = R_s t$, equation (3.3) can also be written as

$$\exp\left(\frac{-\pi R_{12,34}}{R_s}\right) + \exp\left(\frac{-\pi R_{23,41}}{R_s}\right) = 1, \quad (3.4)$$

In either case, the resistivity or sheet resistance must be found numerically. As the determination is based on experimental values, including more data points yields better results. According to the reciprocity theorem [110], $R_{12,34} = R_{34,12}$, which means that two measurements can be made for both the horizontal and vertical setup in Fig. 3.4 [111]. Additionally, measurements of reversed polarities can be included to obtain the following average values for the vertical and horizontal resistances [112]:

$$R_{vertical} = \frac{R_{12,34} + R_{34,12} + R_{21,43} + R_{43,21}}{4} \quad (3.5)$$

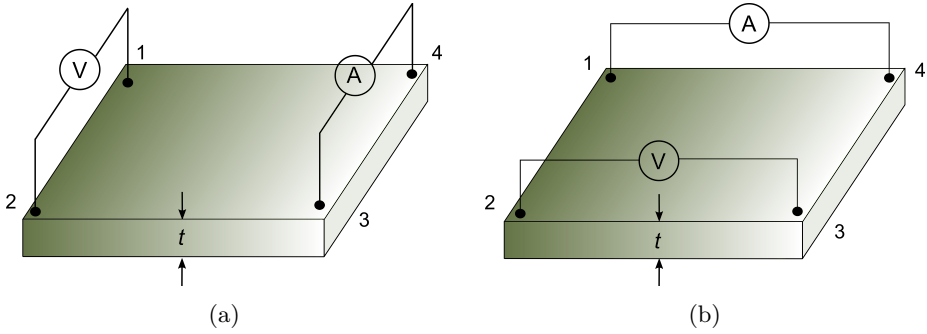


Figure 3.4: Experimental setup for determination of the resistivity or sheet resistance using van der Pauw's method. The resistances $R_{vertical}$ and $R_{horizontal}$ can be obtained from the setup in (a) and (b) respectively.

and

$$R_{horizontal} = \frac{R_{23,41} + R_{41,23} + R_{32,14} + R_{14,32}}{4}. \quad (3.6)$$

Taking the sheet resistance as an example, the final relation then becomes:

$$\exp\left(\frac{-\pi R_{vertical}}{R_s}\right) + \exp\left(\frac{-\pi R_{horizontal}}{R_s}\right) = 1, \quad (3.7)$$

The averaging procedure is one of the strengths of van der Pauw's method when accurate results are required, but it is also one of the major drawbacks. Compared to classical techniques that are based on single measurements, van der Pauw's method requires additional steps which increase the time consumption.

Ideally, the relation between the calculated resistances and the unknown quantities R_s or ρ can be simplified if the sample possesses a line of symmetry. In such cases it can be shown that $R_{12,34} = R_{23,41}$ which leads to the expressions [108]:

$$\rho = \frac{\pi t}{\ln 2} R_{12,34} \quad (3.8)$$

or

$$R_s = \frac{\pi}{\ln 2} R_{12,34}. \quad (3.9)$$

3.2.2 Hall Measurements: Mobility and Carrier Density

In section 2.4.2 a few examples were given where discontinuous jumps of the resistivities were taken as evidence of strain-induced coupling in LSMO-based heterostructures. However, there are currently no known examples where Hall measurements have been performed in such studies. In this work Hall measurements were included in order to accommodate the resistivity measurements. This could for example help determine if possibly discontinuities are caused by changes in the Fermi sphere/carrier density, or by variations in the mobilities.

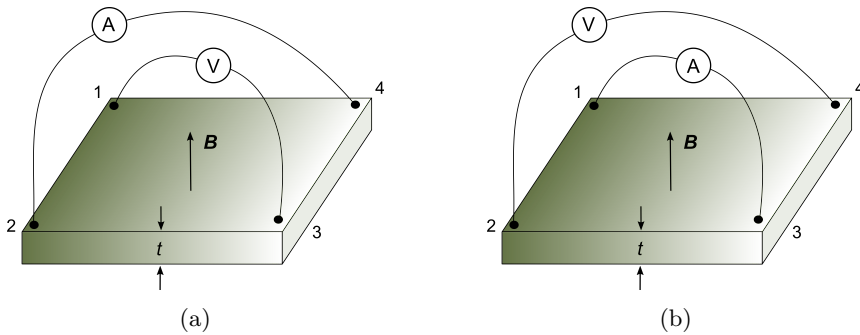


Figure 3.5: Measurement setup for the Hall effect according to van der Pauw's method. The voltage is measured across the opposite diagonal of the current, and a magnetic field is applied normal to the sample surface.

Slight adjustments of the method used for resistivity measurements enables determination of the mobility and carrier density. As was shown previously, these quantities can be calculated using equation (2.17) and (2.22). Given that the sheet resistance or resistivity has been found as described above, the only unknown quantity is the Hall voltage V_H . This can be found by applying a magnetic field perpendicular to the sample surface while forcing a current through one of the diagonals. The induced Hall voltage is measured across the opposite diagonal. Fig. 3.5 illustrates how to perform Hall measurements using van der Pauw's method. Although perpendicularly aligned current and voltage contacts is optimal, the main requirement is that they are crossed.

In most cases the contacts are not perfectly aligned, which introduces unwanted contributions to the voltage drop. These contributions can be several orders of magnitude larger than the Hall voltage and cannot be ignored. Repeating the measurements with the field direction reversed can remove the unwanted contributions due to contact offsets. The effects of a non-ideal setup and the field reversal process are illustrated in Fig. 3.6.

At the bottom of the diagram the ideal case is illustrated where only the Hall effect contributes to the measured voltage, i.e. $V(B=0) = 0$. If this is the case, only one measurement is required. Here it is assumed that a positive magnetic field provides a positive Hall voltage³. At the top the contacts are misaligned, leading to a finite Hall voltage measured at zero field, $V(B=0) = V_0$. Consequently, the correct hall voltage must be calculated using the values that are obtained from the field reversal:

$$V_H = \frac{V(B_+) - V(B_-)}{2} \quad (3.10)$$

Analogously to the resistivity measurements, more accurate results can be obtained by reversing the current direction and rotating the contact setup. Using a

³The sign of the measured voltage will vary with the experimental setup and direction of current relative to the magnetic field. Therefore it is important to make an evaluation of the setup before bonding contacts and applying a current and magnetic field.

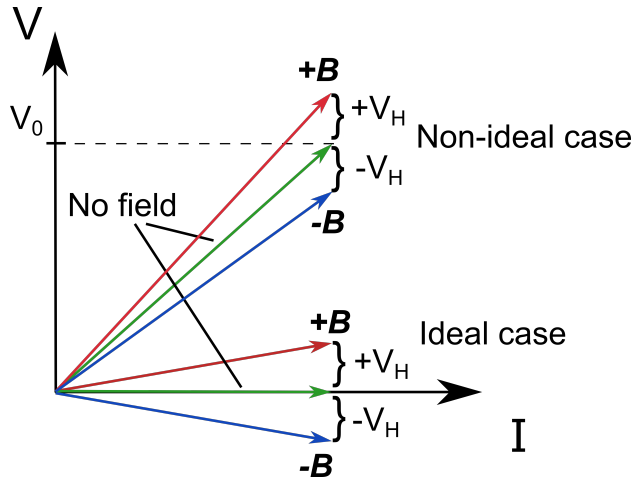


Figure 3.6: A schematic representation of an ideal Hall measurement ($V(B=0) = 0$) (bottom) and a non-ideal ($V(B=0) = V_0$) measurement (top). Only one measurement is needed for the ideal case, whereas two measurements at opposite fields are needed for non-ideal situations.

notation where numbered indices refers to contacts on the sample, and the sign refers to the direction of the magnetic field, the following voltages can be measured and calculated:

$$V_A = V_{13+} - V_{13-} \quad V_C = V_{24+} - V_{24-} \quad (3.11)$$

$$V_B = V_{31+} - V_{31-} \quad V_D = V_{42+} - V_{42-} \quad (3.12)$$

Finally, the Hall voltage can be calculated as the average of these values:

$$V_H = \frac{V_A + V_B + V_C + V_D}{8} \quad (3.13)$$

3.2.3 AC Current Hall Measurements

One of the tasks in this work was to evaluate the use of the VersaLab instrument⁴ when analyzing the Hall effect. Two aspects of the instrument require the treatment above to be slightly altered. The first point is that the system has a built-in AC current source which is used for the Hall measurements. Secondly, the generated data files contains resistance values rather than voltages, which means that the Hall voltage is only indirectly measured. This section provides an overview of the required changes.

In contrast to DC sources, the current changes sign over each period for an AC signal, and uses an average value for the reported resistance. When the current changes sign after half a period, the charge carriers are deflected to the other side

⁴The instrument used for electrical measurements, see section 3.5 for more details.

of the sample, which implies a change of sign for the Hall voltage. By the fact that the reported resistance is calculated as the ratio of the voltage and the current (which has a varying sign), the correct sign is maintained⁵. For this to be true, the response time of the carriers and Hall voltage is assumed to be much faster than the time constant of the AC signal. Normal operating conditions utilizes frequencies on the order of 1 – 30 Hz, which is unproblematic compared to carrier response times on the order of nano to picoseconds [113].

Quantitatively, equation (3.10) cannot be used since the exact values of the Hall voltages are unknown. The solution is to introduce the “Hall resistance” $R_H = V_H/I_x$, which can be determined similarly to V_H by dividing equation (3.10) by I_x

$$\frac{V_H}{I_x} = \frac{V(B_+) - V(B_-)}{2I_x}. \quad (3.14)$$

This can then be rewritten as

$$R_H = \frac{R(B_+) - R(B_-)}{2}. \quad (3.15)$$

Using R_H , the carrier density given by equation (2.17) becomes

$$n = \frac{I_x B_z}{qV_H t} \implies n = \frac{B_z}{qR_H t}, \quad (3.16)$$

Equation (2.21) can still be used to find the mobility, but the sheet density becomes

$$n_s = \frac{I_x B_z}{qV_H} \implies n_s = \frac{B_z}{qR_H} \quad (3.17)$$

3.2.4 Error Estimation

Two disadvantages of van der Pauw’s method are that his two first requirements are never completely fulfilled. Ideally the contacts should be infinitely small, point-like contacts, but it would require an enormous voltage to force the current through an infinitesimal contact area [109]. In practice all contacts have a finite size which introduces errors. The formulas used to approximate the error vary between different geometries, and have been discussed in detail in ref. [114, 115]. In relevance to this work, an example is given for square geometries.

For resistivity measurements on square samples, the correction factor $\Delta\rho/\rho$ is roughly proportional to $(D/L)^2$, where D is the average contact diameter and L the distance between contacts [107]. Similarly, contacts placed at a distance R from the periphery introduces an error $(R/L)^2$. When it comes to Hall measurements the error is considerably larger, as the correction factor $\Delta R_H/R_H$ is roughly proportional to (D/L) or (R/L) . For a given measurement the total error is the sum of the errors associated with each of the contacts.

Normally, the contacts dimensions were roughly 5 to 10% of the length of the sample sides. For Hall measurements this simply implies an error between 5 to 10% per contact, while the error lies between 0.25 to 1% for resistivity measurements.

⁵The instrument is able to report both negative and positive resistances depending on the measured voltages.

3.3 Preparation of Gold Contacts

Ahead of the wire bonding procedure, gold contacts were deposited in each of the sample corners using a Quorum Q150R S plasma sputterer⁶. Manually created masks were used to perform a lift-off procedure in order to ensure correct placement of the contacts. Because of varying sample dimensions and lack of fitting masks, ordinary Scotch tape was used as a mask⁷.

An illustration of the deposition steps can be seen in Fig. 3.7. The tape was cut and prepared with a scalpel under a microscope, and laid on top of the sample surface with the sticky side pointing upwards. Two strips of tape were put on top of each other to leave an opening in every corner, as illustrated by Fig. 3.7b. In the next step, 15 nm of 99.99% gold was sputtered on the sample surface, producing the result shown in Fig. 3.7c. Finally, the tape was removed (lift-off), leaving gold only in the four corners, as shown in Fig. 3.7d. To minimize variations between the samples, a large effort was put into obtaining square gold contacts of equal dimensions. The size of the contacts was chosen with the aim of providing enough space for a few wire bonding attempts.

Given the simple masks that were made, a thin layer of gold was also deposited on the vertical edges of the samples. In a worst case scenario, this may form a junction between the sample puck and the LSMO layers. Using a multimeter, the resistance was measured between the sample puck and the LSMO films. The edge-sample puck resistance was found to be above 10 M Ω for all samples, which is several orders of magnitude larger than the measured LSMO resistances. Overall, gold removal from the edges was not deemed necessary.

3.4 Wire Bonding

Wire bonding is a flexible technique employed when making interconnections to integrated circuits, electronic devices, or in general when making small-scale precise contacts. The operation is somewhat similar to a normal sewing machine, where needles are used to “sew” electrical components together using conducting wires. Bonding wires are normally made of gold, silver, copper or aluminum and are contacted either using ball bonding or wedge bonding.

Ball bonding utilizes a high voltage electrical charge that melts the tip of the wire. The tips then takes the shape of a ball, which explains the name of the technique. Both a downwards force and ultrasonic energy are applied when forming the bond between the sample surface and the wire. In this work ball bonding was tested using gold wire, but none of the attempts were successful.

The term “wedge bonding” comes from the wedge-shaped structure at the end of the needle. An illustration of the wedge bonding process is shown in Fig. 3.8. As opposed to ball bonding, the wedge needle is not just a simple capillary needle. The main difference lies at the end of the wedge needle, where the wire goes into

⁶Numerous attempts were made at bonding directly to the sample surfaces. Because of unstable bond quality the gold deposition procedure was preferred.

⁷Attempts were also made with aluminum foil, but tape was found to yield better results.

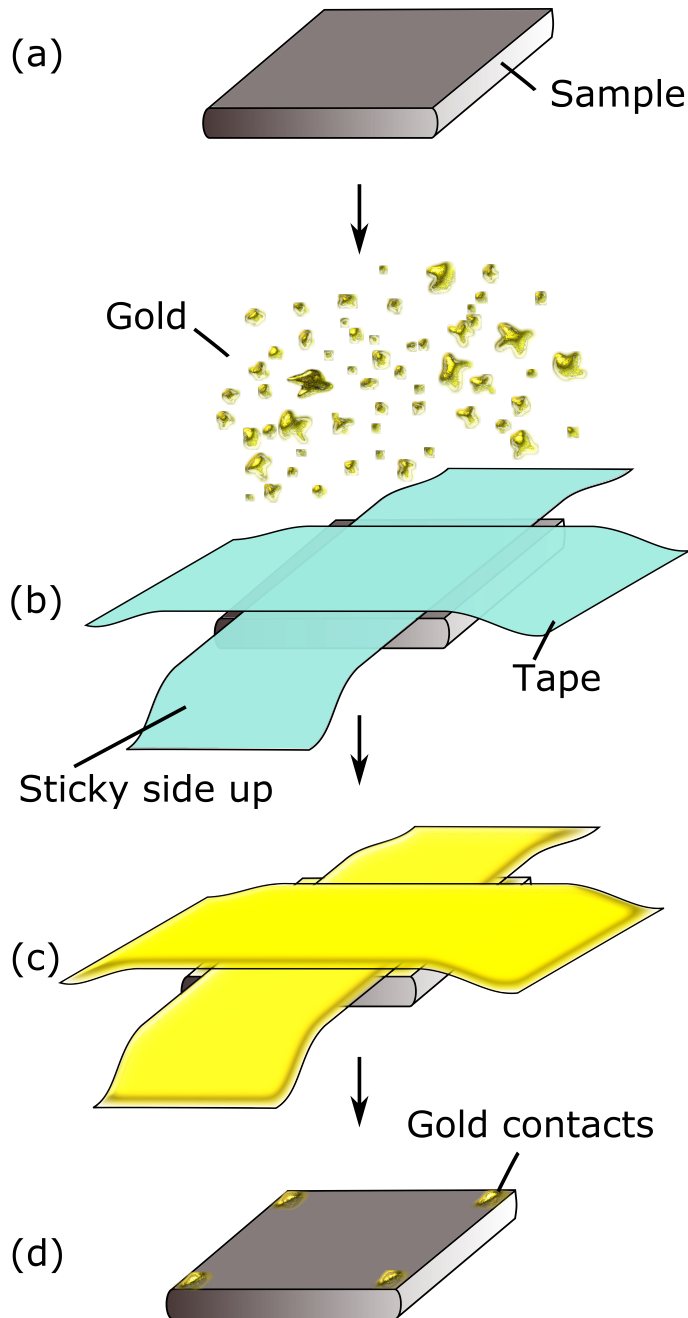


Figure 3.7: Illustration of the lift-off process used when depositing gold contacts on the sample surface. Part (a) shows a clean surface that is covered with tape and sputtered with gold in (b). The result before tape removal can be seen in (c), while the final result with gold contacts in each corner is shown in (d).

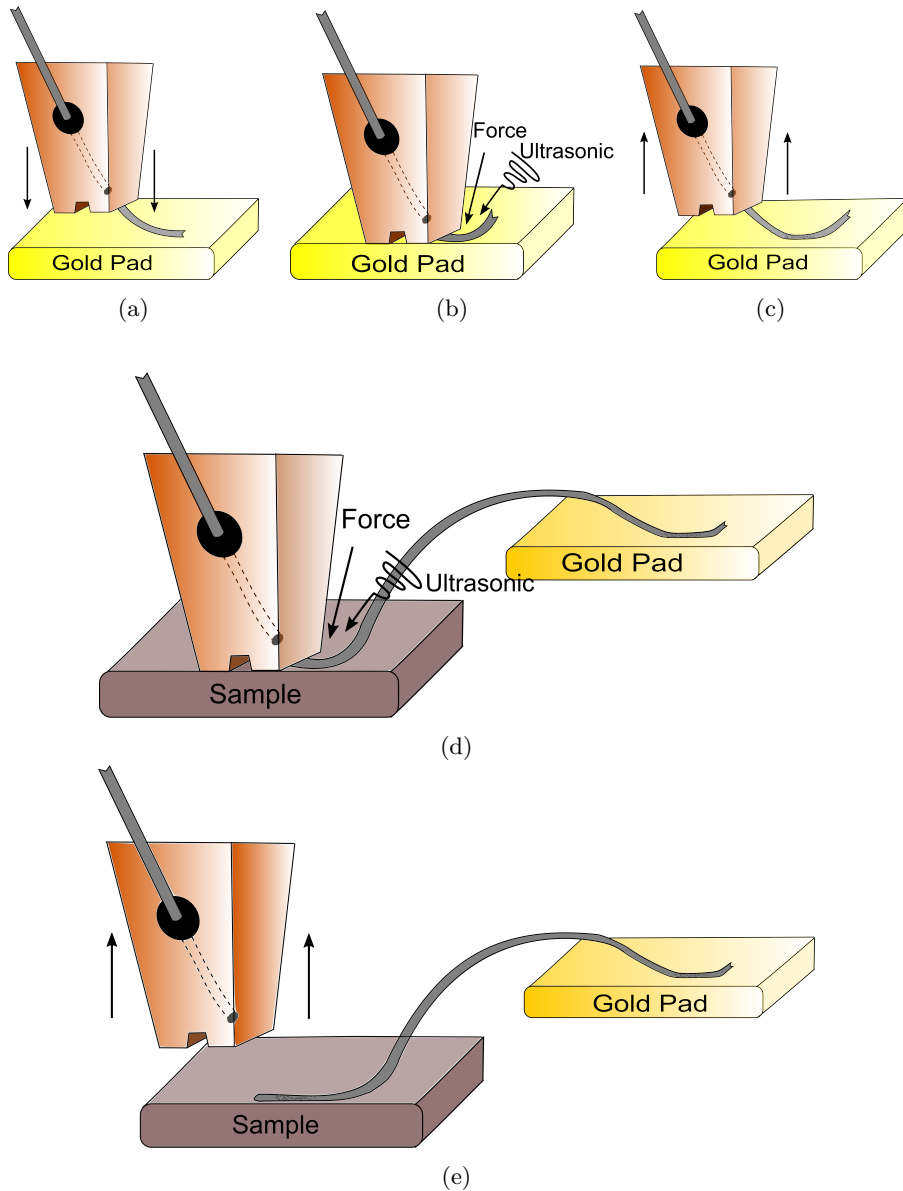


Figure 3.8: Illustration of the wedge bonding process where aluminum wire is bonded between gold pads on the sample puck and the sample surface. In (a) the needle is brought close to the gold pads before the bond is made using force and supersonic energy as shown in (b). In (c) the bond has been made and the needle is lifted and repositioned to the sample surface. The final bond is made in (d) where the wire is cut to yield the final result shown in (e). The placement of the sample contact does not correspond to the actual placement in this work (corners).

the backside of the needle at an angle $\sim 30 - 60^\circ$ and back out at the bottom of the tip. Similarly to ball bonding, both pressure and ultrasonic sound are applied when making wedge bonds⁸. In summary, the most important wedge bonding parameters are [116]:

- **Ultrasonic energy:** The ultrasonic energy provides a mechanical scrubbing action that can help break through oxide layers, and it generates frictional heat that can improve the bonds.
- **Downwards force:** Promotes bonding by forcing the wire into the material surface.
- **Bonding time:** The time at which the needle is in contact with the substrate, mainly connected to the energy provided by the ultrasonic sound.
- **Heat:** Supplying heat evaporates contaminating liquids and makes the bonds adhere more strongly to the surface. Typical temperatures lie around 120°C .

The optimal choice of parameters depends on material properties such as hardness, roughness and atomic content. The best set of parameters is found by optimizing one parameter at a time, while keeping the remaining ones constant. Generally, too large forces or amounts of ultrasonic energy tend to weaken the bonds, and the same applies to long bonding times. Either the bonds break immediately or they are weakened by cracks so that they become unstable over extended periods of time. On the contrary, applying too small forces or amounts of ultrasonic energy renders it difficult to make the bonds adhere to the sample, and they might loosen more easily.

In this work aluminum wires were chosen since gold is too soft for the studied materials. Additionally, previous studies have shown that aluminum can provide good Ohmic contacts to LSMO samples [117, 118]. Whereas ball bonding commonly utilizes gold wires, wedge bonding is better suited for aluminum wires. Consequently, all wire bonding procedures in this work were performed using wedge bonds and aluminum wire with a TPT HB05 bonding tool. Since the samples were mounted on a sample puck that was too large to be used in conjunction with the bonding tool's heating plate, all bonding processes were performed at room temperature. A list of good parameters can be found in Tab 3.1.

As explained in section 3.2, obtaining optimal results using van der Pauw's method requires reconfiguration of the bonding pattern. Ideally, a bond made in

Table 3.1: Overview of typical wire bonding parameters. Bond 1 refers to the bond to the gold pads on the sample puck, and bond 2 to the bond on the sample surface.

	Force	Ultrasonic intensity	Time
Bond 1	25 – 30	200	180 – 200
Bond 2	30 – 35	200 – 240	190 – 210

⁸When using gold wire for wedge bonding, ultrasonic energy is not always necessary, but it is needed for aluminum wire.

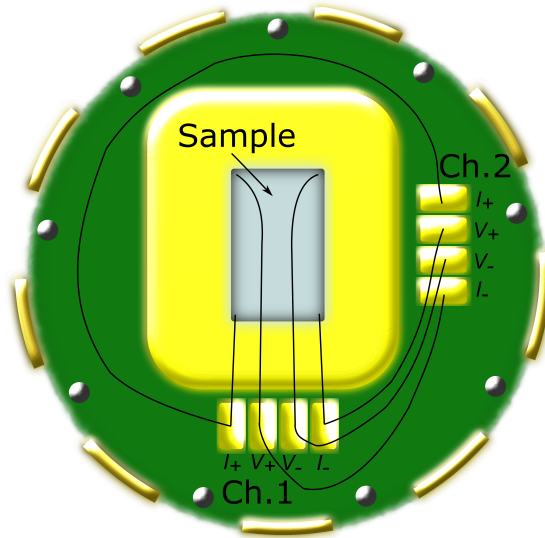


Figure 3.9: Illustration of bonding pattern from gold contacts to sample puck when performing van der Pauw resistivity measurements. Channel 1 is bonded to measure horizontally and channel 2 vertically.

each of the corners is sufficient if it is possible to switch the input/output of each contact, i.e. current source or voltage detection. However, with the equipment available in this work, the gold pads on the sample puck were locked to either I_+ , I_- , V_+ or V_- . On the other hand, the sample pucks had two channels available for measurements, which still requires only four bonds to be made to the sample. Taking resistivity measurements as an example, the bonding scheme in Fig. 3.9 illustrates the idea. With this configuration, channel one is bonded for horizontal measurements, while channel two is bonded in parallel with the gold pads on channel one. This would allow channel two to measure vertically, hence the measurement procedures would be simplified.

3.5 Electrical Transport Measurements

The electrical transport option (ETO) module of a Quantum Design VersaLab instrument was used for resistance measurements in this project. Various scripts were made using the ETO software in order to calculate the resistivity, magnetoresistance and Hall related quantities.

3.5.1 ETO Parameters

Generally, certain parameters provided more consistent results than others when measuring the resistance. An overview of the most important ETO parameters and options is given below:

- **AC amplitude:** Amplitude of the AC current excitation signal. Normally, amplitudes were set in the range 0.001 – 0.1 mA.
- **AC frequency:** Frequency of current signal. Sometimes more noise were detected if the frequency was set below 1 Hz or above 50 Hz. Values were normally chosen in the range 10 – 25 Hz.
- **Voltage range:** The detection limit for the measured voltages (40 μ V – 4 V. Determines the gain of the signal detection.
- **Voltage autorange:** If set to off, it allows the voltage range to be chosen manually as described above. When turned on, the software automatically tries to determine the best suited range. Activating this function gave inconsistent results and it did not seem to work properly. The option was always set to off in this work.
- **Averaging time:** Determines the length of the averaging interval for each data point. The time must be larger than the period of the signal, which is determined by the frequency. Higher frequencies allows for lower averaging times, while still including the same number of periods in the average for each data point. Thus the total measurement time can be decreased while roughly keeping the same accuracy.
- **Temperature rate:** Normally given in K/min and is limited to the range 0.03 – 20 K/min. While scanning continuously during a temperature sweep, the rate must be slow enough to allow the sample to keep up with the chamber temperature.
- **Field rate:** Similarly to the temperature rate, too large values (maximum 0.03 T/s) cause a delay in the system, and a mismatch between the reported resistance and the actual resistance at the given field value. Keeping the rate below 0.02 T/s avoided such problems.
- **Set temperature:** Sets a target value for the temperature. The temperature changes continuously at the chosen rate until it reaches the target.
- **Set field:** Sets a target value for the field. The field changes continuously at the chosen rate until it reaches the target.
- **Scan temperature:** Changes the temperature stepwise from a chosen starting point to a set end temperature. The size of the steps and the rate between each step are entered manually. At each step the system waits for the temperature to stabilize, and it can execute additional commands.
- **Scan field:** Scans the field analogously to the temperature scan described above.

Choice of Current Amplitude and Voltage Range

Because of varying sample resistances, the AC current amplitude and voltage range had to be optimized separately for each of the samples. The amplitude was varied manually, and the voltage range was adjusted accordingly. The stability of the reported resistance was used as a criterion for the parameter optimization. The parameters were considered to be sufficiently optimized when an amplitude change of 10% led to resistance changes smaller than 0.1%. The standard deviations of the reported resistances were also taken into account during the optimization.

Generally, it was desirable to set the amplitude as high as possible without introducing heating problems or software errors⁹. Too small amplitudes may lead to difficulties when detecting weak voltage signals. Since a large current amplitude requires a large voltage range, the signal gain is lower than for smaller amplitudes, which may reduce the noise levels. If the generated voltage is larger than the detection limit, the signal will saturate and produce inaccurate results.

ETO Temperature Settings

The temperature reported by the instrument can be ambiguous since it is measured inside the chamber, while there is no guarantee that this is equal to the real sample temperature. Even though a thermally conducting glue was used to stick the samples to the sample puck, the heat transfer is not an instant process. Setting the temperature rate too high during a temperature sweep might introduce a mismatch between the reported temperature and the real sample temperature.

Such problems are most likely to occur while measuring continuously using the *set temperature* command. The magnitude of the errors is largest close to T_C , where the temperature dependence of the resistance is at its strongest. Typically a temperature hysteresis produces errors by up to 15% in this region if the rate is not set on the order of 0.1 K/min. A continuous temperature scan is only regarded as a useful tool when a “quick and dirty” approach is desired.

To minimize errors associated with temperature mismatch, the slower and more accurate *scan temperature* command is preferred. This option provides a stable sample temperature while scanning in steps of 1 K at a rate of 3 – 10 K/min. All results in this work were obtained using the stepwise option.

3.5.2 ETO Scripts

Various ETO scripts were made with the goal of balancing out the efficiency and accuracy of the measurements. Including more points or reducing the temperature rates always increased the accuracy, but at the expense of an increased time consumption. The exact setup of each of the developed scripts affected the end results differently. Therefore, a qualitative overview of the most important scripts is given below, whereas the complete versions can be found in appendix A. Additionally, a short description of the output data is provided

⁹The software errors were mostly the instrument’s inability to drive high amplitude currents through the sample.

Resistivity and Magnetoresistance vs. Temperature

1. The field is set to 0 T.
2. Start temperature scan from 400 to 50 K with increments of 1 K corresponding to 351 steps. The rate was set to 1 K/min between each step.
3. At each step perform a single resistance measurement, averaged over 10 s.
4. Stop zero field measurement at 50 K.
5. Set field to 2 T, or any other desired value.
6. Repeat step 1 – 2 from 50 to 400 K in a magnetic field.

Output data: Two data sets with one resistance value per Kelvin in the range 50 – 400 K, at 0 T and at 2 T respectively.

Magnetoresistance vs. Magnetic Field

1. Start temperature scan from 400 to 250 K with increments of 10 K, and a rate of 10 K/min between each step.
2. At each temperature step perform the following:
 - Wait 6 min for temperature to stabilize.
 - Scan field from 0 to 3 T in steps of 0.05 T. Perform a single resistance measurement at each field step, averaged over 10 s.
 - Set field to 0 T and continue to next temperature.
3. End measurement at 250 K.

Output data: Each data set has one resistance value every 0.05 T in the range 0 to 3 T. The sets include resistances for every 10 K between 250 K and 400 K.

Hall Measurements

1. Start temperature scan from 400 to 50 K with increments of 25 K, and a rate of 10 K/min between each step.
2. At each temperature step perform the following:
 - Wait 6 min for temperature to stabilize.
 - Scan field from 0 to 3 T in steps of 0.05 T. Perform a single resistance measurement at each field step, averaged over 10 s.
 - Set field to 0 T
 - Scan field from 0 to –3 T in steps of 0.05 T. Perform a single resistance measurement at each field step, averaged over 10 s.
 - Set field to 0 T and continue to next temperature.

3. End measurement at 50 K.

Output data: Two data sets are generated for every 25 K between 50 K and 400 K. The first set of these pairs contains one resistance value every 0.05 T in the range 0 to +3 T, and the second the equivalent between 0 to -3 T.

3.6 Data Processing and Measurement Overview

In order to analyze and convert the data into relevant transport properties, additional calculations and processing were needed. To achieve this, various scripts were written in MATLAB. A complete version of these can be found in appendix B.

An overview of the measurements and calculations that were performed for each of the samples can be seen in Table 3.2. As will be discussed in section 4.3, only a single bonding configuration was measured for most of the samples. This has been indicated in the table.

Table 3.2: Overview of the measurements performed for each of the samples. A single X denotes measurements based on a single bonding configuration, while XX indicates that two configurations were measured. $R_H(T)$ includes calculations of the carrier density and mobility.

Sample	$\rho(T)$	$MR(T)$	$MR(H)$	$R_H(T)$
Reference	XX	XX	X	X
BTO(1.26 nm)/LSMO	X	X		X
BTO(5 nm)/LSMO	X	X		XX
BTO(10 nm)/LSMO	X	X		X
LSMO/BTO(1.26 nm)	X	X		X
LSMO/BTO(5 nm)	X	X	X	X

4. Results and Discussion

The aim of this chapter is to discuss the main objectives in this work. The first part focuses on the establishment of the technique. An overview of the most important steps has already been provided in the experimental chapter, but this chapter includes more in-depth discussions and explains how and why specific parameters and procedures were chosen. Additionally, a major part is devoted to the analysis of potential errors, and to discussions of the current limitations of the technique. The latter part applies especially to the Hall measurements, since the corresponding analysis was more complex than for the other transport properties. To help the reader better understand subsequent results, the two first sections of this chapter discuss complications related to the calculations of the Hall resistance and the carrier density.

The second part focuses on the results that were obtained when utilizing the technique to characterize (111)-oriented BTO/LSMO-based heterostructures. Relevant transport properties are displayed graphically, and the measured sample structures are compared. Possible trends are examined and viable explanations are proposed. Based on these results, the potential existence of magnetoelectric coupling will be discussed.

4.1 Calculating the Hall Resistance

The first step of the Hall analysis, is to utilize equation (3.15) in order to calculate the Hall resistance from the output data described in section 3.5.2. Ideally, this removes all field symmetric contributions that do not originate from the Hall effect. Examples of the resulting Hall resistances will be shown in section 4.2, while this section focuses on the potential errors related to these calculations.

By the fact that the ordinary Hall effect is a field dependent phenomenon, the Hall resistance is expected to be zero when no external field is applied¹, i.e. $R_H(0) = 0$. In other words, the positive and negative field sweeps should both start at the same resistance value. An example of the measured resistance as a function of the applied field can be seen in Fig. 4.1. This example illustrates an ideal case where the two initial values are equal. The overall shape is mainly determined by

¹This is not always true for materials exhibiting the anomalous Hall effect.

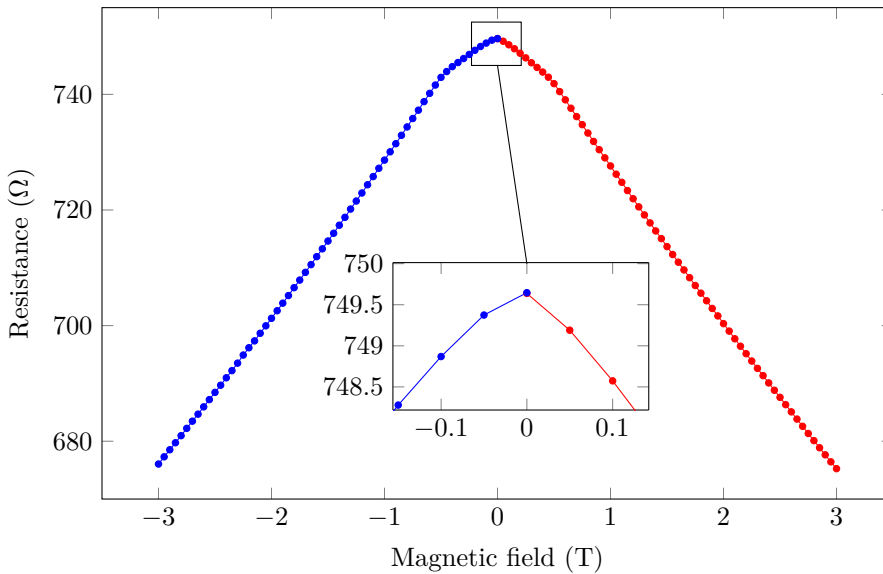


Figure 4.1: Example of an ideal resistance vs. field plot measured using a van der Pauw Hall geometry. The data was obtained from BTO(1.26 nm)/LSMO at 250 K.

the magnetoresistance, while the small offsets between corresponding positive and negative fields are caused by the Hall effect.

However, an additional offset was frequently observed at zero applied field. An example of a non-ideal case with a rather large zero field offset of about 0.5Ω can be seen in Fig. 4.2. Generally, the offsets got smaller as the temperatures decreased, and they were mostly below 0.1Ω . Fig. 4.3 shows the typical magnitude of the offsets as a function of temperature. As will be shown in the next section, the resulting Hall resistances were sometimes on the order of 0.01Ω . Consequently, offsets of the observed magnitude may be of great importance. Below, a few explanations have been suggested for the offsets.

Temperature Drift

One possible explanation, is that the temperature of the sample has not been allowed to stabilize before the measurement starts. This was often found to be the case when scanning the temperature in steps of 25 K as described in section 3.5.2. Fig. 4.4 shows an example of the resistance drift over the first 400 s for a selection of measurements between 50 – 170 K. As can be seen, the resistance mostly begins to stabilize after a delay of 300 s. Minor instabilities are present after 400 s for some of the included temperatures. Still, these are of small magnitude and could have been caused by other errors.

In this example only relatively low temperatures are included, but similar behavior was observed at higher temperatures. Generally, delays longer than 400 s

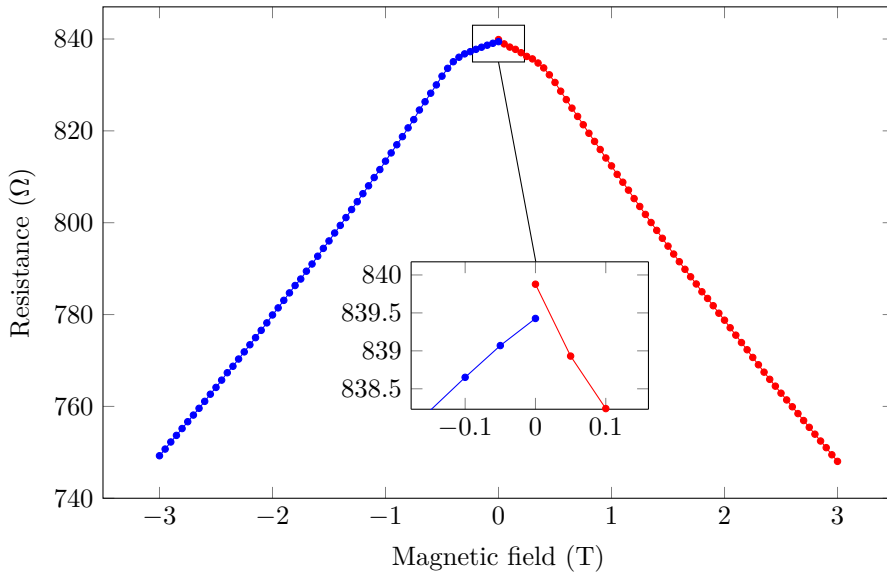


Figure 4.2: Example of a non-ideal resistance vs. field plot measured with the sample bonded in a van der Pauw Hall geometry. The data was obtained from BTO(1.26 nm)/LSMO at 275 K.

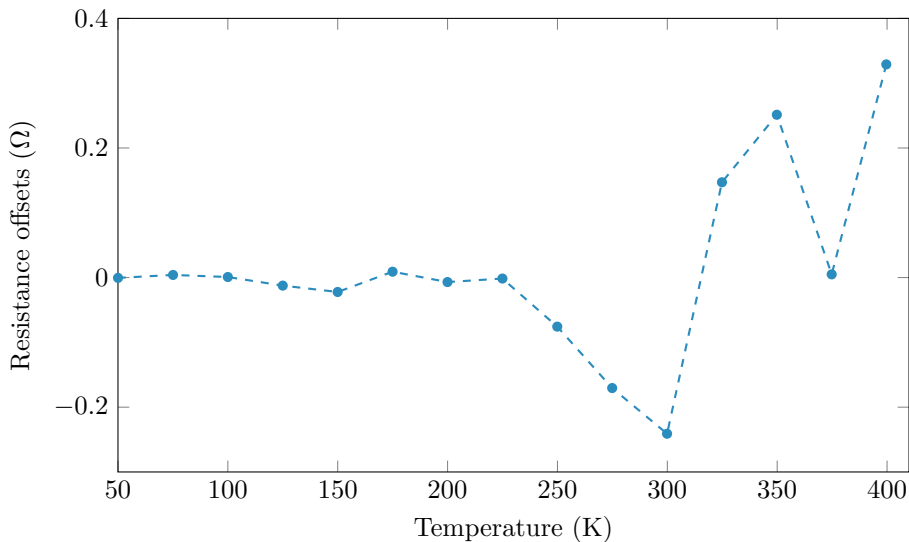


Figure 4.3: Calculated zero field offsets for the reference sample during measurements of the Hall resistance. The values were calculated as the difference between the zero field resistance from the positive and negative field sweep.

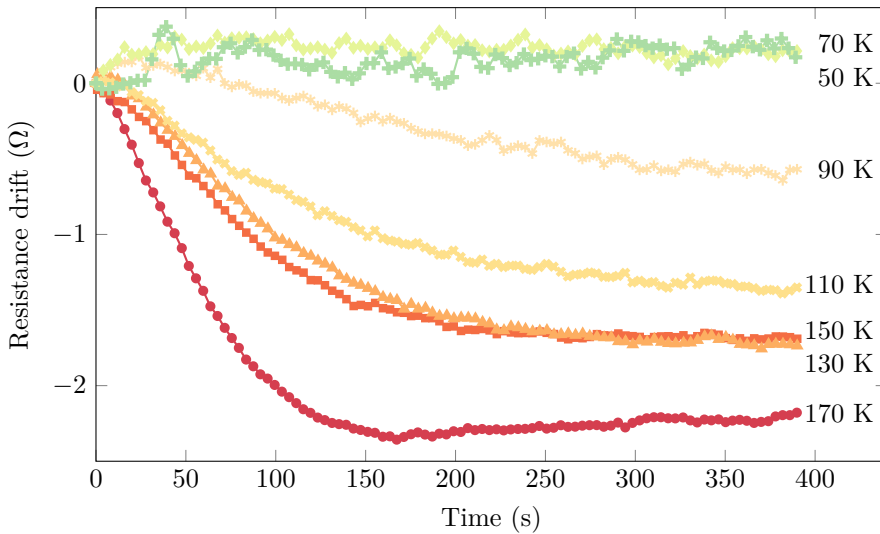


Figure 4.4: Temperature stability measured on the test structure BTO(100nm)/LSMO in the temperature range 50 – 170 K. The resistance values were calculated as the difference between the resistance at $t = 0$ and $t = x$ for x up to 400 s.

did not improve the stability. To prevent errors caused by temperature drift during Hall measurements, a delay of 6 minutes was added at the start of each step. Introducing this delay decreased the offsets by a factor of 2–3. However, the result in Fig. 4.2 was obtained after the addition of the delays, implying that temperature drift was not the only reason for the offsets.

Anomalous Hall Effect

According to equation (2.27) the anomalous Hall effect is only indirectly dependent on external fields through the magnetization $M(B, T)$. More importantly, the anomalous Hall effect is known to produce a finite Hall resistance for ferromagnetic materials even in the absence of a magnetic field [119, 120]. This stands in contrast to the statement regarding the ordinary Hall effect at the beginning of this section.

Because of the ferromagnetic hysteresis in LSMO, a remnant magnetization is likely to be present after each field sweep, implying a finite anomalous contribution. Since the field was reversed at each step, the direction of the remnant magnetization would also be reversed when changing from a positive to a negative field sweep. As opposed to the CMR effect, the anomalous Hall effect is dependent on the sign or direction of the magnetization. Effectively this would double the potential offsets rather than eliminating them. For this explanation to be true, the remnant polarization produced by the negative fields is assumed to persist as the temperature is decreased by 25 K. Given the complexity of the anomalous Hall effect, it is hard to quantify the magnitude of its contribution. Nevertheless, neither this proposal

can explain the apparently random change of sign for the offsets.

General Observations

In this work T_C was found to lie around 340 K for the BTO/LSMO samples, and 5 – 10 K lower for the LSMO/BTO samples². Close to T_C , even minor magnetization differences may lead to significant variations of the measured resistance because of the double exchange mechanism. As was shown in Fig 4.3, the offsets were of larger magnitude at high temperatures, which may indicate that they originated from physical instabilities (temperature, magnetization etc.)

Other potential explanations include ETO instrument errors or unstable bonds. Offsets caused by such factors are expected to fluctuate in time, and to vary between different measurements. Since the ETO parameters were kept constant for each individual measurement, the magnitude of offsets caused by instrument errors was expected to be relatively constant. Therefore, the temperature dependence shown in Fig. 4.3 weakens the explanation based on such factors.

To summarize, the exact cause of the zero field offsets was not determined with certainty. Consequently, a combination of the mentioned factors was considered to be the most probable explanation. Importantly, no procedures were developed that consistently removed the offsets. The potential impacts the offsets may have on the final results will be discussed in section 4.2.2.

4.2 Calculating the Carrier Density

After the Hall resistance has been determined as a function of magnetic field, the next step is to calculate the carrier density based on the one-band model described in section 2.5.1. In addition to being relatively simple, this model is often used in the literature, which enables comparisons to similar studies. Even though it was noted in section 2.5.2 that both electrons and holes contribute to the transport properties, holes are known to dominate below T_C . This means that the one-band model can be useful over a large range of temperatures. However, the Hall resistances calculated using equation (3.15) do not necessarily correspond to R_H in the expression for the carrier density (equation (3.16)). This possible discrepancy is a consequence of the anomalous Hall effect.

Two different approaches were compared in MATLAB when calculating the carrier density based on the one-band model. The main difference between the methods were the procedures used to find a correct value of R_H . The first and simplest approach assumed the anomalous contribution to be negligible compared to the ordinary effect. Neither the second method incorporated the anomalous effect in the treatment, but procedures were implemented in order to extract values only from the ordinary Hall effect. The following parts give an overview of these two methods, and explain why one of them was chosen over the other.

²Approximate values for T_C was determined in a parallel study of the magnetic properties by Torstein Bolstad.

4.2.1 Single-Value-Based Calculations

Using the single-value-based method, an average value of R_H was calculated from a set of data points at 3 T^3 . This relatively naive method assumes the anomalous contribution to be negligible compared to the ordinary Hall effect. Even though this is a rather crude simplification, there are examples of previous studies based on this approach. One example is a preliminary study of LCMO where the researchers obtained qualitatively useful data, but observed that the absolute values of the carrier densities diverged notably compared to studies that included the anomalous Hall effect [121]. The main advantage of this approximation is that the calculations become relatively quick and simple.

In order to check the validity of this approximation, the Hall resistance was plotted as a function of magnetic field at different temperatures. As an example, Hall resistances have been plotted at selected temperatures in Fig. 4.5 for the reference sample. At low fields ($< 0.8\text{ T}$), the anomalous Hall effect dominates and the slopes are negative, i.e. $R_a \gg R_H$. Moving to higher fields, the ordinary Hall effect becomes more important, which can be seen from the linear behavior and the positive slopes. When comparing the absolute values of R_H , it is evident that the anomalous contribution cannot be neglected. In fact the anomalous Hall effect is stronger than the ordinary effect for all of the included temperatures, but its magnitude is greatly reduced as the temperature decreases. This is analogous to the saturation effects described at the end of section 2.5.3. As expected, the ordinary Hall effect exhibits a weaker temperature dependence. Consequently the single-value-based method will result in erroneous carrier densities, and the sign of the carriers may be wrong. The calculated carrier density for the reference sample is shown in Fig. 4.6. Although the absolute values might seem reasonable, the negative values indicate that electrons rather than holes are the dominant charge carriers. The inaccuracy of this result will become clearer when a better method is introduced in the next section.

In conclusion, this method is not suited for studies of the Hall effect in LSMO. At best it may provide qualitative results below 100 K , where the anomalous contributions may become negligible at large fields.

4.2.2 Slope-Based Calculations

In the one-band model the ordinary Hall effect forms the basis for the analysis. This means that contributions from the anomalous effect should be excluded. As explained above, this is not achieved with the single-value-based method. An alternative approach only utilizes the region with a positive slope when calculating the Hall resistance, and is therefore referred to as the “slope-based method”.

³It is also possible to choose a set of values at any other field, but the maximum applicable field value was used in order to minimize the anomalous contribution.

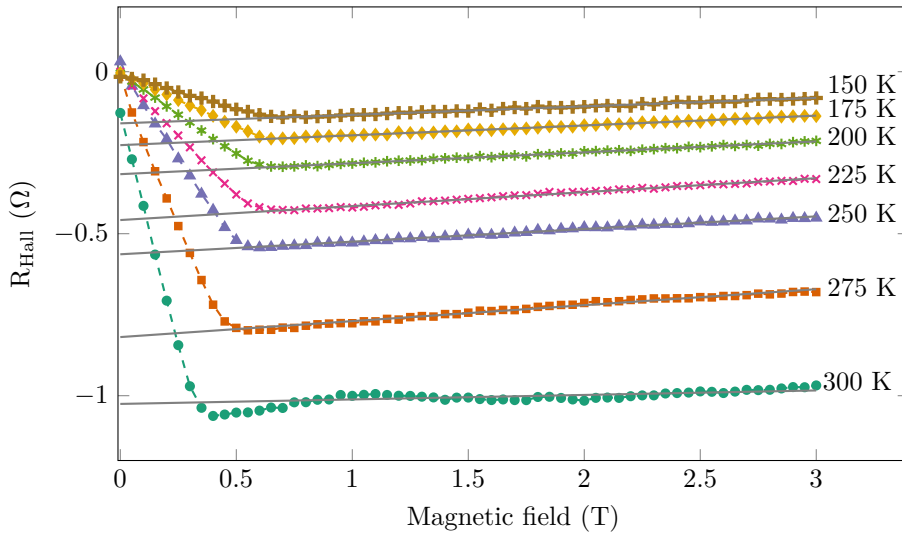


Figure 4.5: Hall resistances in the range 150 – 300 K for the reference sample. The part with a negative slope corresponds to the anomalous Hall effect, and the one with a positive slope comes from the ordinary Hall effect. A linear curve fit has been applied between 1 – 3 T, and is used when calculating the real Hall resistance using the slope-based method.

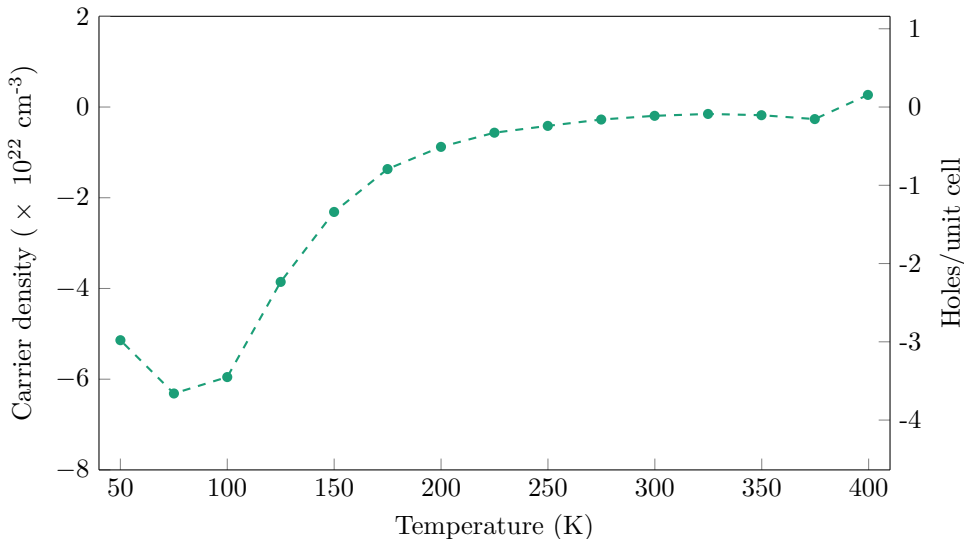


Figure 4.6: Calculated carrier density for the reference sample using the single-value based method. The negative sign implies that electrons are the main charge carriers which is not known not to be the case.

Working Principle

Focusing on the regime below T_C , the measurements indicated that the anomalous effect saturated between 0.5 and 1 T for all of the samples. In order to extract the values of the slopes, linear curve fits were applied to the Hall resistances in the linear region. For simplicity all points were weighted equally, but an option was added to alter the weight of each point depending on manually chosen parameters. Returning to Fig. 4.5, examples of the linear curve fits can be seen for each of the temperatures.

Having determined the values of the slopes in units of V/T , calculating the carrier density is straight forward. By the use of slopes rather than single values, a more accurate indication of the carrier charge is achieved. In Fig. 4.7 the carrier density for the reference sample has been re-calculated using the slope-based method. As opposed to the previous method, the positive carrier densities agree with the theoretical expectation of holes as the main carriers.

The mentioned curve fit can be applied to any set of data points as long as they are within the linear region. Fig. 4.8 shows the calculated carrier densities using data points from different field regimes. Evidently, the potential errors increase as fewer points are included. Moreover the largest impact are seen for carrier densities close to T_C and at low temperatures. In some cases including data points solely from high fields may be advantageous, but this is not always true for measurements with a large degree of noise. Especially the exclusion of data points below 100 K was found to be less ideal. The way the scripts were designed in this work, choosing the ideal range has to be done manually for each data set. For simplicity, all curve fits in this work were based on data from the region 1 – 3 T. For the remaining part of this thesis, all Hall related quantities are calculated using the slope-based method.

Limitations and Errors

There are a few limitations one should be aware of when using this method, and some of them become more pronounced at certain temperatures. These errors are discussed next, in addition to potential problems caused by the zero field offsets

Above T_C : The most apparent of these limitations, is a consequence of the complexity of the Hall effect above T_C . At such temperatures the Hall effect is governed neither by the ordinary Hall effect nor by the anomalous Hall effect, but rather the hopping motion of charge carriers [122]. To this date the exact mechanism is not well understood close to T_C , and the effect of an inhomogeneous magnetic state makes a proper analysis difficult. For LSMO this dependence has yet to be determined and is regarded as relatively complicated. Despite of this, the carrier densities were calculated above T_C similarly to lower temperatures, but the resulting values do not necessarily reflect the real material properties. This was mainly done for comparisons with similar studies. To better illustrate the behavior at high temperatures, Fig. 4.9 shows Hall resistances between 325 and 400 K for the reference. The large offset at 400 K and the otherwise inconsistent behavior at 350 K and 375 K indicate that none of the known theories are applicable.

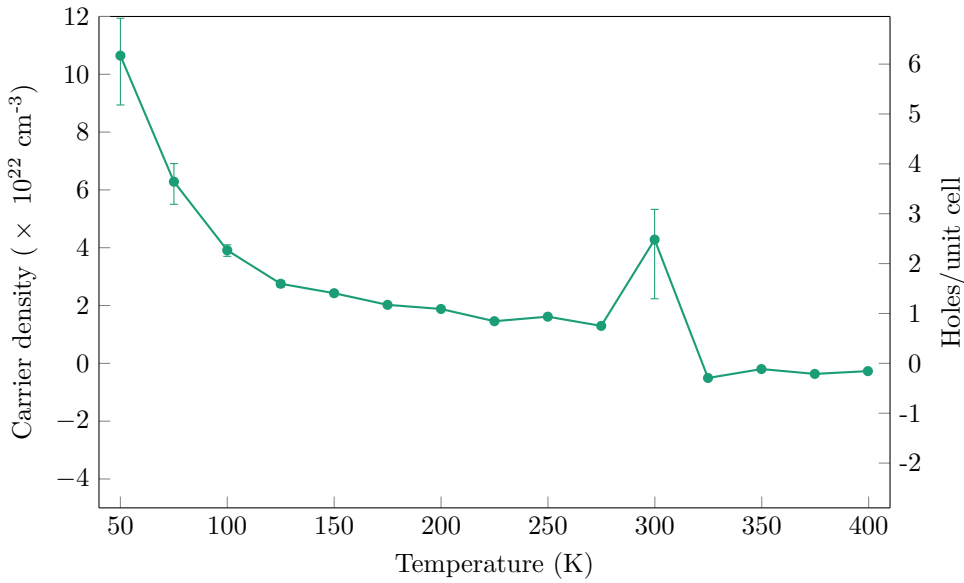


Figure 4.7: Carrier density for the reference sample, calculated using the slope-based method. The error bars are based on the curve fits and indicate the 95% confidence intervals.

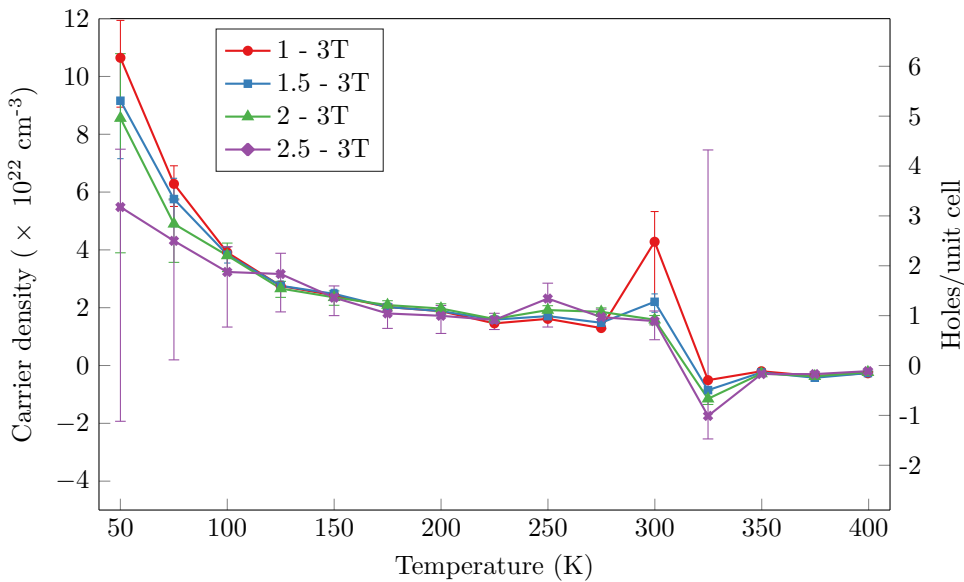


Figure 4.8: Comparisons of carrier densities calculated using different Hall resistances corresponding to different field ranges. The results were obtained from the reference sample.

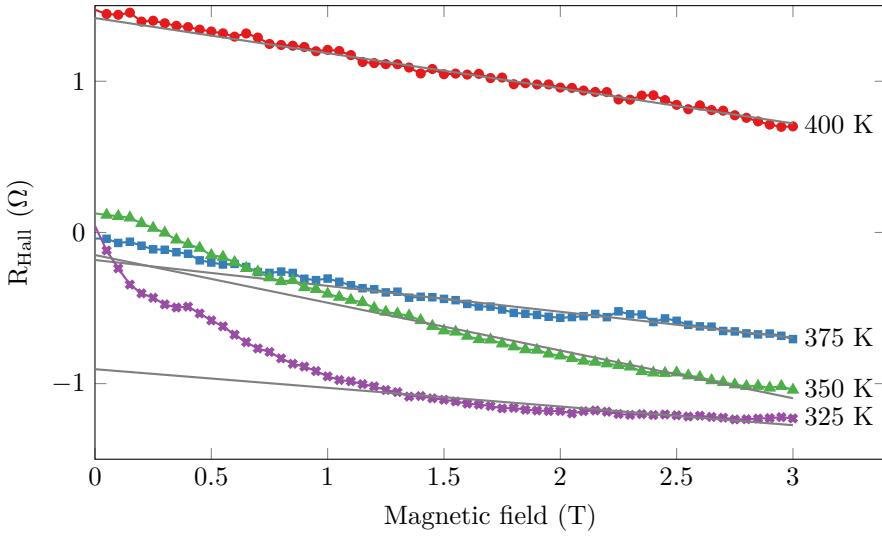


Figure 4.9: High temperature Hall resistances for the reference sample. The linear curve fits were applied between 1 – 3 T.

Slightly below T_C : In some cases measurements down to 70 K below T_C also introduced problems, since the anomalous effect seemed to dominate even at fields up to 3 T. Looking at the curve measured at 325 K in Fig. 4.9, it is evident that the anomalous Hall effect dominates. Generally, this often led to incorrect values close to T_C , and larger uncertainties caused by the linear curve fit. One way to overcome such problems is to increase the field until the anomalous effect saturates. Previous investigations have shown that a linear region is observable for all temperatures below T_C when stronger fields (> 5 T) are employed [123]. However, the equipment limited the maximum value of the magnetic field to ± 3 T in this work.

Below 100K: At low temperatures both the Hall resistance and the slope become smaller. To illustrate this, the change of the resistance over the linear region was calculated as $R(3\text{ T}) - R(1\text{ T})$ for the reference sample. The result is shown in Fig. 4.10 for temperatures well below T_C . These values are also indirect measures of the slopes. When comparing the values at 275 K and 50 K, a ten-fold decrease can be seen. At the lowest temperatures, the resistance change were of the same order as the standard deviations related to the ETO measurements. A short discussion of the standard deviations can be found in section 4.4.3. For now it will be stated that they were normally about $0.02\ \Omega$ and sometimes as high as $0.1\ \Omega$. The importance of this noise at 50 K and 275 K can be seen in Fig. 4.11a and 4.11b respectively. These plots show magnified versions of R_H , and demonstrate that the noise levels change dramatically relative to the slopes as the temperature decreases. Returning to Fig. 4.7, this explains the large error bars at low temperatures.

Zero field offsets: Regarding the zero field offsets, three scenarios can be imagined where the measurements should provide trustworthy results. In the first

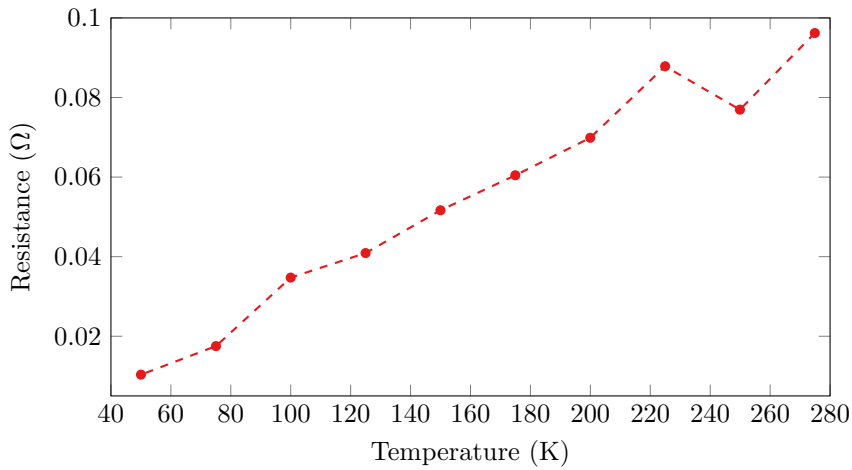


Figure 4.10: Difference between largest and smallest resistance value in the range 1 – 3 T for the reference sample. Only the temperature range where the ordinary Hall effect was clearly visible has been included.

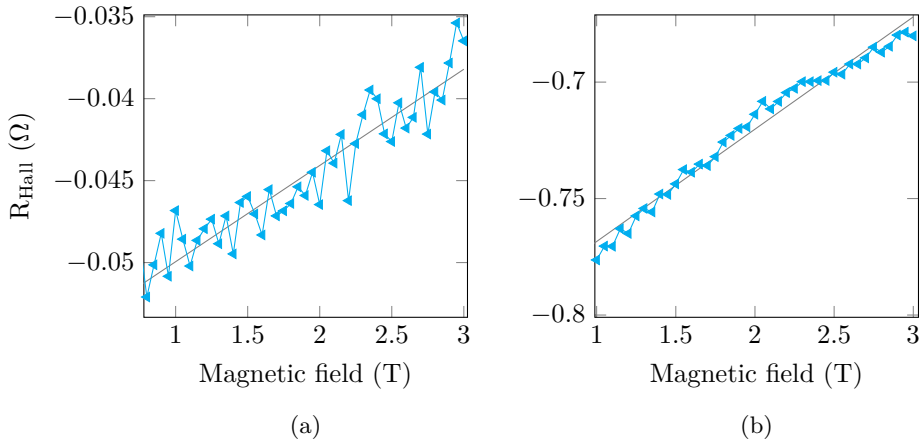


Figure 4.11: Magnified versions of the linear region of the Hall resistance for the reference at (a) 50 K and (b) 275 K.

scenario, the offsets are assumed to be caused by instabilities that changes the resistance at a constant rate. If this is the case, each point would be shifted by the same amount. Therefore, the slopes based on the differences will not be affected.

In a second scenario, the offsets can be imagined to develop during the time between the positive and negative sweeps. This time period takes place at the end of each positive sweep, as the field is brought back to zero. When a new measurement is started for the negative sweep, the configuration of the instrument electronics might have changed slightly, or software related calibration procedures may be different. If this was to be the case, all measurements taken at negative fields values would be shifted equally, thus the calculated slopes would remain the same.

Lastly, offsets caused by the anomalous Hall effect would not cause any major problems as long as the slopes form the basis for the calculations.

Temperature drift: Even though steps were made to avoid temperature drift, the potential errors will be discussed next. Taking a measurement with a decreasing temperature as an example, the resistance will also decrease (at least below T_{MI}). If a sufficient time delay is not included, the resistance will keep decreasing as the measurement starts. During the first field sweep, the system is likely to reach the correct temperature. As the field gets back to zero, the resistance would therefore be lower than at the initial measurement. Depending on whether the system is cooled or warmed, the end result would be a slightly increased or decreased slope. Similar errors may be produced by unstable bonds or fluctuating instrument instabilities.

4.3 Bonding Scheme

Previously, the bonding configuration in Fig. 3.9 was suggested for van der Pauw measurements. With this bonding scheme, the resistance is first measured by channel one and subsequently by channel two⁴. An important premise for this parallel coupling to work properly, is that there can be no cross-talk between the two channels. This criteria is met if the unused channel acts like an open circuit while the other is measuring. In reality however, samples that were bonded to both channels at the same time sometimes resulted in a larger degree of noise than those only bonded to one. Additionally, the producer of the equipment confirmed that the setup was not designed to be used with the proposed bonding scheme. The main cause of this was considered to be the fact that both channels are connected to the same voltmeter and current source. Therefore, the electronic components cannot be operated totally independently.

An alternative bonding approach is to remove the wires after the first measurement, and rewire them in a different configuration ahead of the second. This provides the desired values for the averaging procedures, and avoids cross-talk between the channels. The main drawback of this solution, is that the already

⁴These measurements can be done in quick succession with practically no delay.

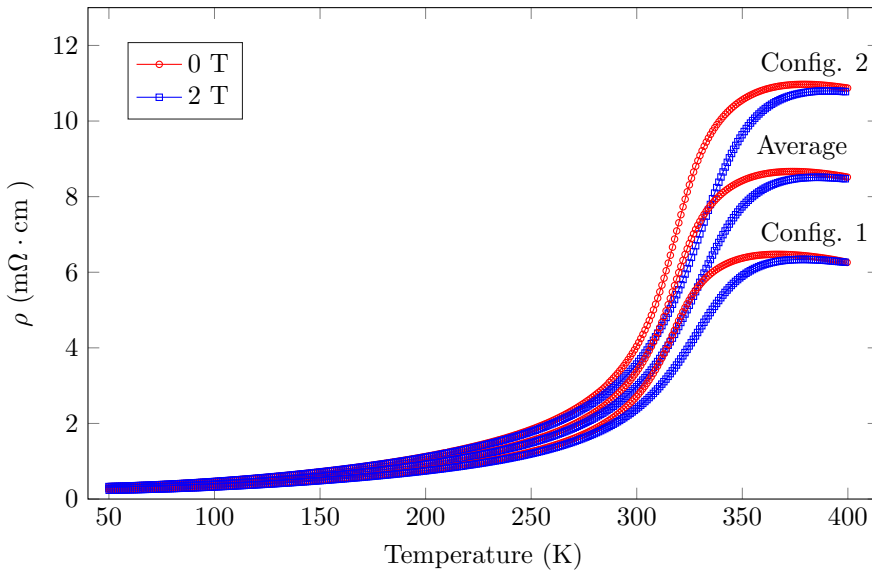


Figure 4.12: Comparison of resistivity calculations using a horizontal and vertical bonding configuration at 0 T and 2 T for the reference. The average value was calculated numerically using van der Pauw’s formula. The result was obtained when investigating the use of only a single bonding configuration.

extensive measurement times⁵ are close to doubled for resistivity measurements, and increased by a factor of about 1.5 for Hall measurements: If both channels are wired simultaneously, only a single temperature or field sweep is needed, since data can be obtained from both channels at each step. On the contrary, rewiring the sample requires the sweeps to be executed twice. Even though the total time spent on resistance measurements would be almost the same for both cases, the time consumption of the temperature/field sweeps are normally the limiting factor.

To explore the potential differences between two bonding configurations, the rewiring approach was performed once for resistivity measurements and once for Hall measurements. The corresponding results are discussed next with focus on the bonding scheme.

4.3.1 Resistivity and Magnetoresistance

Fig. 4.12 shows the measured resistivity for the reference sample at 0 T and 2 T. The measurements were performed using both a horizontal and vertical bonding scheme. The average result was found by solving equation (3.3) numerically. The overall shapes are relatively comparable, and the T_{MI} values only vary by a few percent. However, the absolute values of the two configurations differ by up to 50 %

⁵As an example, performing a single resistivity and magnetoresistance vs temperature sweep from 50 – 400 K takes up to 48 hours.

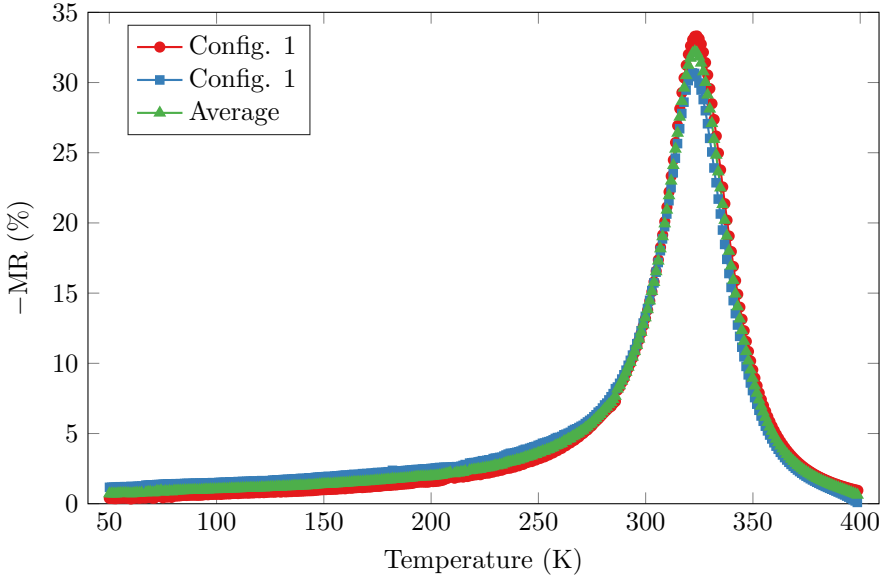


Figure 4.13: Calculated magnetoresistance at 2 T for the reference sample using a horizontal and vertical bonding configuration. The result was obtained when investigating the use of only a single bonding configuration.

compared to the average. Because of other potential errors, it is hard to pinpoint the exact deviations caused by the varying bonding configurations. Furthermore the reference sample was not perfectly square-shaped, and the sample sides were about half the length a of the other samples. As will be discussed later on, this increases the potential differences between the horizontal and vertical configurations. Hence, the observed discrepancies might have been smaller for some of the other samples. Nonetheless, this result emphasizes that the averaging procedures are crucial for accurate results.

Based on the data in Fig. 4.12, the corresponding magnetoresistances were also calculated, as can be seen in Fig. 4.13. Here, the differences are less pronounced, and the values vary by about 10% at the peak. This can be explained by the fact that the magnetoresistance is calculated as a relative difference (equation (2.1)) rather than being proportional to the measured resistance. Consequently, the obtained magnetoresistance values were assumed to be more precise than the resistivities.

4.3.2 Hall Resistance and Carrier Density

Similarly to the above examples, Hall measurements were carried out using two different bonding configurations, but with the sample structure BTO(5 nm)/LSMO. The calculated Hall resistances and the corresponding curve fits have been plotted between 125 and 275 K in Fig. 4.14. The largest errors of up to 20% were observed

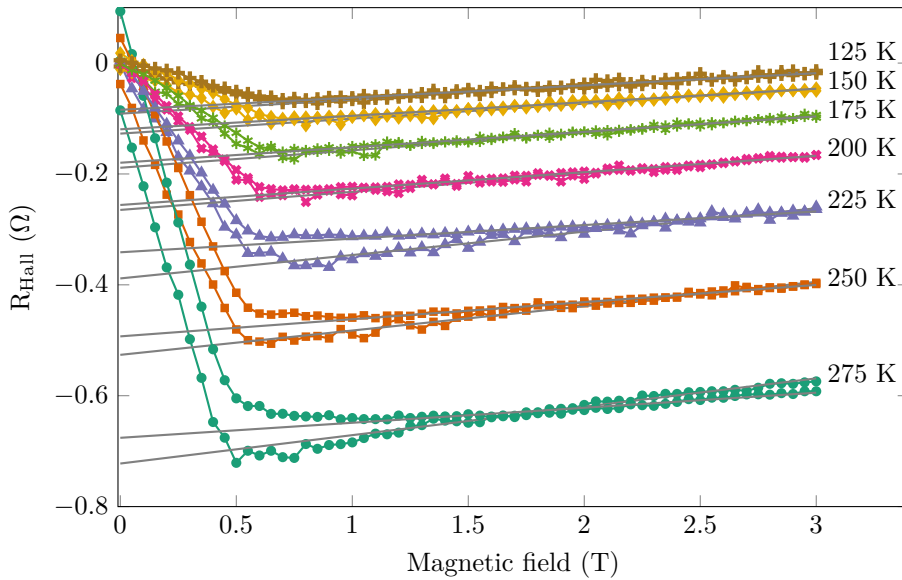


Figure 4.14: Calculated Hall resistance for BTO(5 nm)/LSMO using two different bonding configurations. The result was obtained when investigating the use of only a single bonding configuration.

in the anomalous region, i.e. at high temperatures and at low fields. On the contrary, the differences between the bonding configurations were on the order of 1 – 5 % in the linear region. As with the magnetoresistances, the small deviations can be explained by the fact that the Hall resistance is calculated as a difference. An important point is that a field of about 1.5 T was needed in order to produce linear behavior above 225 K, but the curve fits were applied between 1 – 3 T at all temperatures.

The corresponding carrier densities are shown in Fig. 4.15. Ignoring the values above 300 K, the largest errors of about 50 % can be seen in the range 225 – 300 K, which is in line with the findings in Fig. 4.14. Although the result has been omitted here, changing the range of the applied curve fit to 2 – 3 T reduced the errors to below 10 %. This functions as a reminder of the fact that the range of the curve fits should be optimized individually instead of consistently using the region between 1 – 3 T.

In summary, including data from more than one bonding configuration seemed to be most critical for resistivity measurements. This can be explained by the fact that the resistivity is proportional to the reported resistances, while the other quantities result from differences. For accurate and quantitative measurements disregarding the optimal bonding procedures is not recommended, but a simpler approach may be a useful tool for qualitative studies.

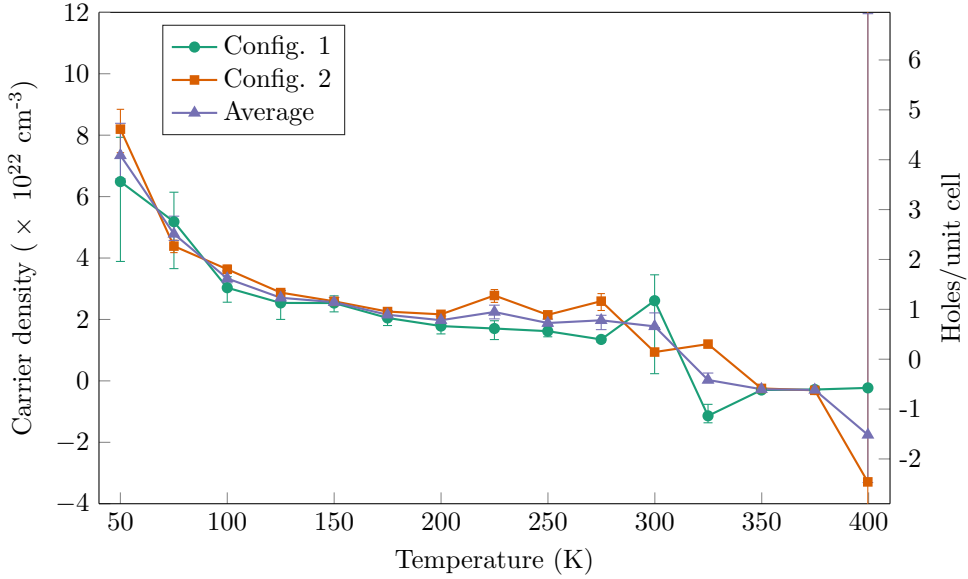


Figure 4.15: Calculated carrier density for BTO(5 nm)/LSMO using two different bonding configurations. The result was obtained when investigating the use of only a single bonding configuration.

4.3.3 Conclusion

As a consequence of the potential problems related to a parallel bonding scheme, usage of both channels simultaneously was avoided. Furthermore, the alternative solution of rewiring the samples was omitted due to time constraints. Unless stated otherwise, this means that all results referred to in this thesis are based on measurements from a single bonding configuration with only one channel. Clearly, this removes one of the strengths of van der Pauw's method, but the above results showed that the qualitative significance is not lost. Moreover, steps were taken to minimize the errors caused by the simplified measurement procedure. As described in section 3.2.1, symmetric samples ideally yield the same resistance for both configurations, which allows van der Pauw's equation to be simplified to equation (3.8). To be able to exploit this convenience, the samples were deliberately cut as squares. Thus, the lack of averaging should be less detrimental. Lastly, the AC current source implies that current reversal was included indirectly for each measurement.

4.4 General Errors

Several potential errors have already been mentioned, but the majority of them were related to the Hall measurements. In this section, errors will be discussed that

are of general importance for all types of measurements. This includes problems associated with finite contact dimensions, aluminum bond formation and choice of ETO parameters.

4.4.1 Finite Contact Dimensions

In section 3.2.4 it was stated that van der Pauw's method assumes infinitely small contacts, which is unrealistic in real experiments. The gold contacts formed in this work were of approximately the same size. However, since the sample dimensions differed by a factor of two, the errors were larger for smaller samples as a consequence of the increased (D/L) ratio. Furthermore, the shape of the samples varied slightly due to edges that were not ideally cut⁶. Since the non-straight edges impacted the corner regions the most, the gold contacts were not always perfectly square-shaped.

With respect to quantitative measurements, the Hall related uncertainties of 5 to 10% per contact are of significant magnitude. On the other hand, they are not expected to vary in time as long as the contacts remain intact. Additionally, the errors are relatively controllable and easy to quantify. In summary, this means that finite contact dimensions were not expected to undermine the qualitative usefulness of the results. The errors between 0.25 and 1% per contact for resistivity measurements were not considered to be critical in this work.

4.4.2 Aluminum Bonds

Obtaining ideal contacts both requires good electrical contact, and that the bonds adhere to the surface and are mechanically stable. Although a simple quality check can be made with a multimeter and through a visual inspection, it is difficult to determine if the bonds are optimal. Repeatedly bonding to the same sample with the same settings occasionally led to contact resistances varying by up to 10%, but the differences were normally on the order of 1 – 2%.

Another complicating factor was the observation of degrading bond quality over time. If the samples were left unused for a couple of days, the resistance had often increased by a few percent. This was not considered to be critical for the resistivity measurements, but may lead to noticeable errors for the Hall measurements, since these rely on small differences. Physical degradation and aluminum oxidization were suggested as the most probable explanations for this observation. To minimize such problems, the measurements were performed immediately after the bonding procedures, and new bonds were made when the resistance had increased by a few percent compared to the first measurement.

4.4.3 ETO Parameters

Based on preliminary optimizations, the current amplitude and voltage range were set between 0.005 – 0.01 mA and 40 – 400 mV throughout this work. This led

⁶The (111)-orientation of the samples complicates the cutting process. As opposed to (001)-oriented samples there are no natural cleavage planes [124].

to standard deviations between $0.02 - 0.1 \Omega$ which was found to be independent of temperature. However, a more careful optimization procedure was carried out for the reference sample at the end of this work. With an amplitude of 0.5 V and a voltage range of 400 mV the standard deviation was reduced by a factor of 20, resulting in deviations on the order of 0.001Ω . This could lead to great improvements of the Hall calculations below 100 K .

4.5 BTO/LSMO Heterostructures

Previous sections have shown a selection of results with the goal of illustrating important limitations or procedures related to the established of the technique. This section is devoted to the main results that were obtained when comparing different BTO/LSMO heterostructures.

4.5.1 Resistivity vs. Temperature

The resistivities were measured between 50 K and 400 K for all of the sample structures, and have been plotted in Fig. 4.16. The corresponding metal-insulator transition temperatures are summarized in Table 4.1. Considering the combination of errors that was found to influence the results, comparing the absolute values should be done with care.

The resistivities for the reference and BTO(5 nm)/LSMO are almost overlapping, indicating that the BTO layer has little influence on the transport properties. On the other hand, the sample with a thinner BTO layer is shifted towards slightly larger resistivities. It should also be noted that the resistivity for the reference corresponds to the average shown in Fig. 4.12. If the second bonding configuration in that figure had been plotted, the reference would have overlapped with BTO(1.26 nm)/LSMO instead. Essentially this means that the values for these three samples lie within the expected error range, thus complicating the search for general trends.

The large upwards shift of the resistivity for the sample with 10 nm BTO possibly indicates that thicker BTO layers increases the resistivity. An even larger shift was observed for the LSMO/BTO structures, which cannot be explained by the un-

Table 4.1: Overview of metal-insulator temperatures for each of the measured sample structures

Sample	$T_{MI}(\text{K})$
LSMO	373.9
BTO(1.26 nm)/LSMO	355.6
BTO(5 nm)/LSMO	380.5
BTO(10 nm)/LSMO:	364.5
LSMO/BTO(1.26 nm)	329.8
LSMO/BTO(5 nm)	311.7

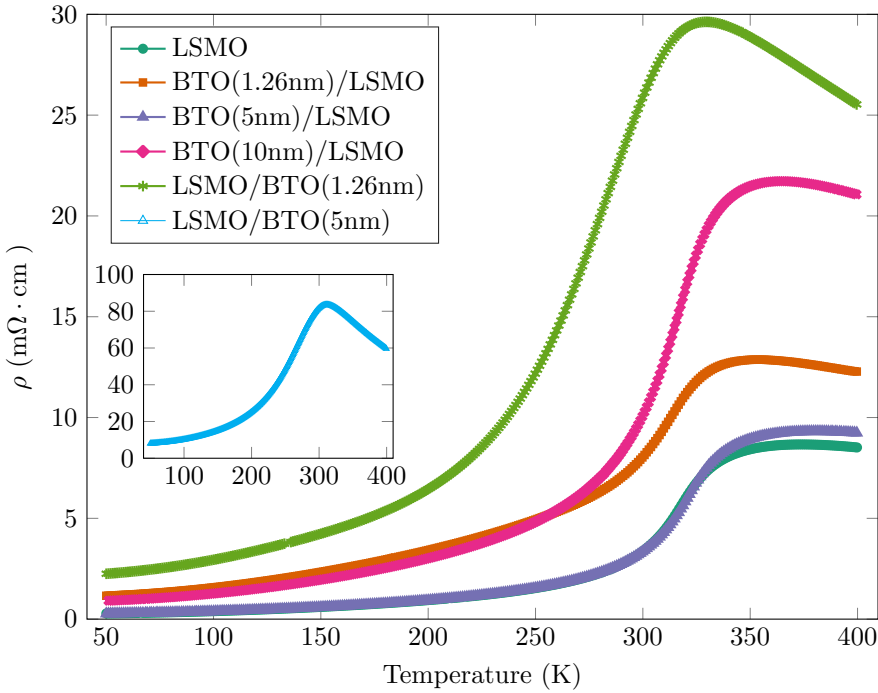


Figure 4.16: The resistivities plotted as a function of temperature for all of the samples. The inset shows the resistivity for LSMO/BTO(5 nm) separately as it was significantly larger than the rest.

certainties. The same trend can be seen when comparing the T_{MI} values, as the two lowest transition temperatures were obtained for the samples with LSMO on top. Since the LSMO thickness was kept constant, these observations were attributed to lower LSMO film quality when grown on BTO rather than the STO substrates. Moreover, the LSMO/BTO structure with the thickest BTO layer (5 nm) exhibited the largest resistivities and the lowest T_{MI} value. This indicated that the film quality gradually got worse as the BTO thickness increased, which implies a non-ideal epitaxial growth of BTO. Generally, a decreased film quality may involve a lower degree of crystallinity, or the presence of defects and impurities. Such factors suppress the hopping mechanism of the itinerant carriers in LSMO, effectively increasing the resistivity and reducing T_{MI} .

In the literature there are several examples of measurements based on (001)-oriented LSMO films with thicknesses between 10 – 150 nm. Similarly to the results in Fig. 2.3, the reported resistivities range from around 0.3 mΩ · cm at 50 K, to about 50 mΩ · cm close to 350 K [34, 117, 125, 126]. (111)-oriented LSMO has been reported to lie in the lower part of this range [127], which is analogous to the results for the reference and the BTO/LSMO samples in this work. The measured metal-insulator transition temperatures for the BTO/LSMO samples agree with

the literature, but the values obtained from the LSMO/BTO samplers are about 20 – 60 K lower than what is normally reported.

As opposed to the first studies given as examples in section 2.4.2, no discontinuous jumps were observed at temperatures corresponding to the phase transitions of BTO. The same applies to the phase transition of the STO substrates at 105 K. In spite of this, the latter studies in that section proved that the lack of such discontinuities is not necessarily synonymous with zero coupling. Clearly, some of the heterostructures in this study produced significantly different results as compared to the reference. These variations may have been caused by a combination of errors and varying film quality. However, they could also indicate that BTO affected the properties of LSMO by imposing strain at the interfaces. As was shown in the first example in section 2.4.1, BTO has already been observed to be able to change the transport properties of LSMO via strain effects. In order to determine the origin of these variations with greater certainty, the accuracy of the measurements needs to be improved.

4.5.2 Magnetoresistance vs. Temperature

The calculated magnetoresistances are plotted as a function of temperature in Fig. 4.17. Similarly to the results above, a close overlap is seen between the reference and BTO(5 nm)/LSMO. Since the errors associated with the magnetoresistances were expected to stay below 10%, this may indicate that the overlapping resistivities was not a coincidence. Additionally, the RHEED oscillations indicated a more ideal layer-by-layer growth for these two samples than the others⁷. Consequently these samples were assumed to be of higher quality, hence corroborating the assumption of better transport properties.

Focusing on the peak temperatures, the LSMO/BTO samples attained the largest magnetoresistances in the range 275 – 285 K, which is 40 – 70 K lower than in previous reports. The BTO/LSMO layers peaked around 330 K which is in close agreement to previous studies [33, 126, 128]. These observations provide further evidence which indicates that the transport properties of the LSMO layers were altered considerably when grown on BTO. Another feature separating the LSMO/BTO samples from the others, was the observation of wider peak regions and larger magnetoresistances at lower temperatures. The proposed explanation of a reduced hopping rate for these structures is likely to go in hand with an increased degree of misalignment between the spins. Therefore, the application of an external field may still yield a substantial magnetoresistance in the range 50 – 150 K. Although the largest magnetoresistance was obtained for the reference sample at around –33%, the effect of adding BTO layers did not seem to be predictable.

4.5.3 Magnetoresistance vs. Magnetic Field

To get a broader perspective of the magnetoresistance, it was measured as a function of the applied magnetic field at a range of temperatures close to the peak

⁷Observed in unpublished work by Torstein Bolstad

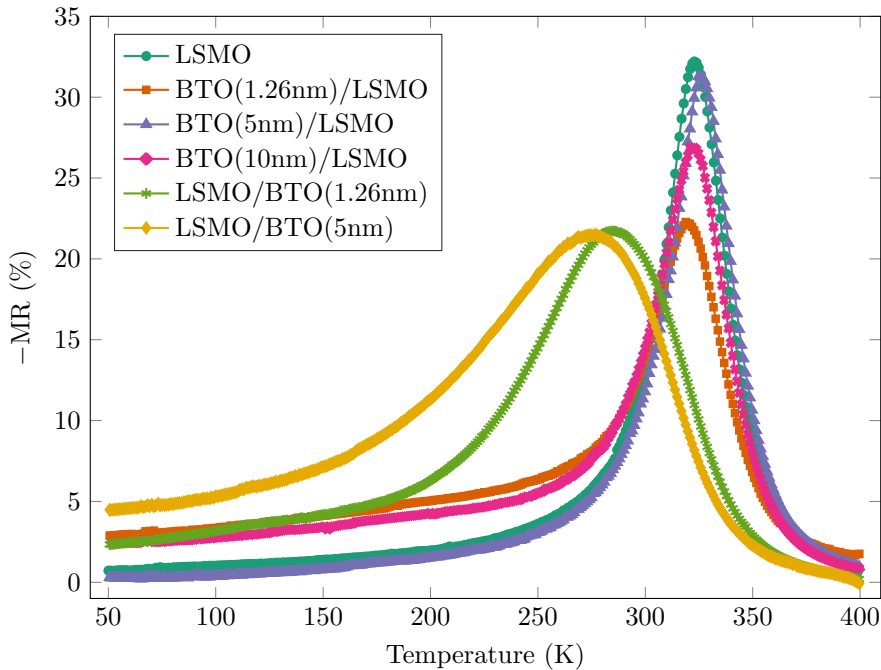


Figure 4.17: Comparison of the magnetoresistance as a function of temperature. The values were calculated based on resistivity measurements at 0 T and 2 T.

value. Examples are shown for the reference sample and LSMO/BTO(5 nm) in Fig. 4.18 and 4.19 respectively. As expected, the magnetoresistances increased slowly at temperatures well above the peak temperatures. In the proximity of the peaks, the magnetoresistances increased at larger rates and exhibited close to linear behavior. It was also noted that relatively high fields were required in order to observe a significant magnetoresistance. Taking the reference as an example, approximately 0.6 T was required in order to obtain absolute values larger than 10% at the peak temperature. This emphasizes the practical problems related to exploiting the CMR effect in LSMO.

An interesting observation, is the relatively large magnetoresistances for the reference sample⁸. At the peak temperature in Fig. 4.18, the magnetoresistance lies close to -45% at 3 T, whereas previous studies have reported values between -15 to -35% at 5 T both for (001) [126, 129] and (111)-oriented samples [127]. Based on the the slope at 320 K and 3 T in Fig. 4.18, it is possible that an even larger magnetoresistance would have been observed at 5 T. The most probable explanation is considered to be a better film quality than samples with lower peak values⁹.

⁸ The same was observed for the sample structure BTO(5 nm)/LSMO

⁹ Further discussions regarding the film quality are not included since this was not the topic of this work.

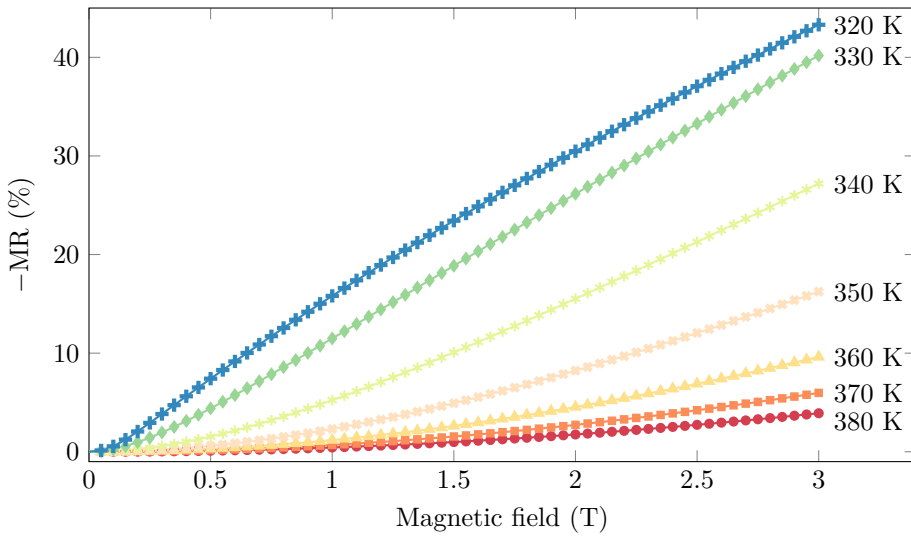


Figure 4.18: Magnetoresistance plotted as a function of an external magnetic field for the reference sample. The included temperature range was chosen in order to capture the behavior from the minimum values to the peak at about 320 K.

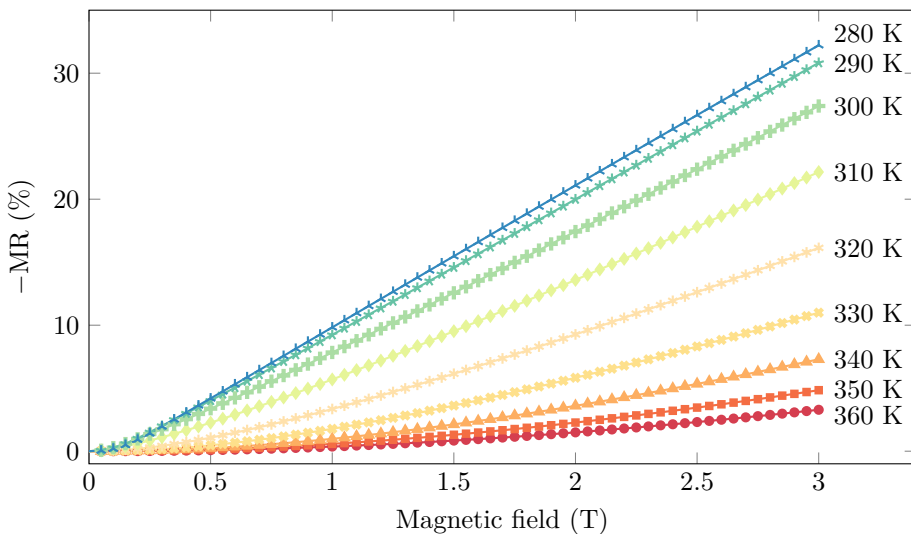


Figure 4.19: Magnetoresistance plotted as a function of an external magnetic field for LSMO/BTO(5 nm). The included temperature range illustrates the behavior from the minimum values to the peak at about 275 K.

4.5.4 Carrier Density

The calculated carrier densities have been plotted separately between 50 – 400 K in Fig. 4.20. Although varying results were obtained above 275 K and below 100 K, the calculated carrier densities were relatively consistent between 100 – 275 K. In this regime the carrier densities were found to slowly increase from about 1 to 2 holes/unit cell, which is comparable to the results in previous studies [20, 105, 123]. However, these values surpasses the theoretical expectation of 0.3 holes/unit cell that was mentioned in section 2.1.3. This mismatch is a result of the simplifications that were made using the one-band model. In section 2.5.2 it was noted that electrons are known to contribute to the transport in LSMO. Thus the slope of the Hall resistance is decreased, which means that the one-band model tends to overestimate the carrier density. Overall, this emphasizes the fact that a two-band model should be employed in order to obtain more accurate results.

Given the complexity of the system close to or above T_C , this regime will not be given further attention, other than stating that similar behavior has been observed by others using the same model [20]. Once again, the reference and BTO(5 nm)/LSMO show the same behavior, while a larger spread is seen for the other samples. The most inconsistent result was obtained for LSMO/BTO(5 nm), which strengthens the proposal of lower film quality for this sample. Below 100 K, either a major increase or decrease takes place, in addition to a change of sign for four of the samples. To the knowledge of the author, no other studies have reported similar behavior. One explanation is that the transport properties actually changes dramatically at low temperatures due to the crystal orientation or coupling to the BTO layers. On the contrary, the inconsistent change of sign suggests that the measurements are influenced by uncertainties of considerable magnitude. It has already been stated that the impact of the standard deviations increases in this region, which may explain the results. To confirm if these observations originated from presently unknown mechanisms, the accuracy of the method needs to be improved.

4.6 Mobility

The mobility was calculated using equation (2.21), which means that it is affected by the errors from at least two bonding procedures (sheet resistance and sheet carrier density). Because of this, comparing all of the calculated mobilities was not considered to provide any new insights. To illustrate the general behavior, the calculated mobilities are included only for the reference sample and BTO(5 nm)/LSMO. These results are shown in Fig. 4.21. Ignoring the negative sign caused by the erroneous carrier densities above 300 K, the increasing trend from 300 – 125 K is in line with the expected behavior for LSMO and LCMO [97, 130]. On the contrary, the maximum values around 0.4 – 0.5 cm²/Vs are significantly lower than previously reported mobilities of 1.8 cm²/Vs [131] and 3.67 cm²/Vs [130]. These studies were based (001)-oriented films with thicknesses of 200 nm and 500 nm respectively. Thus, direct comparisons cannot be fully justified. Additionally, the

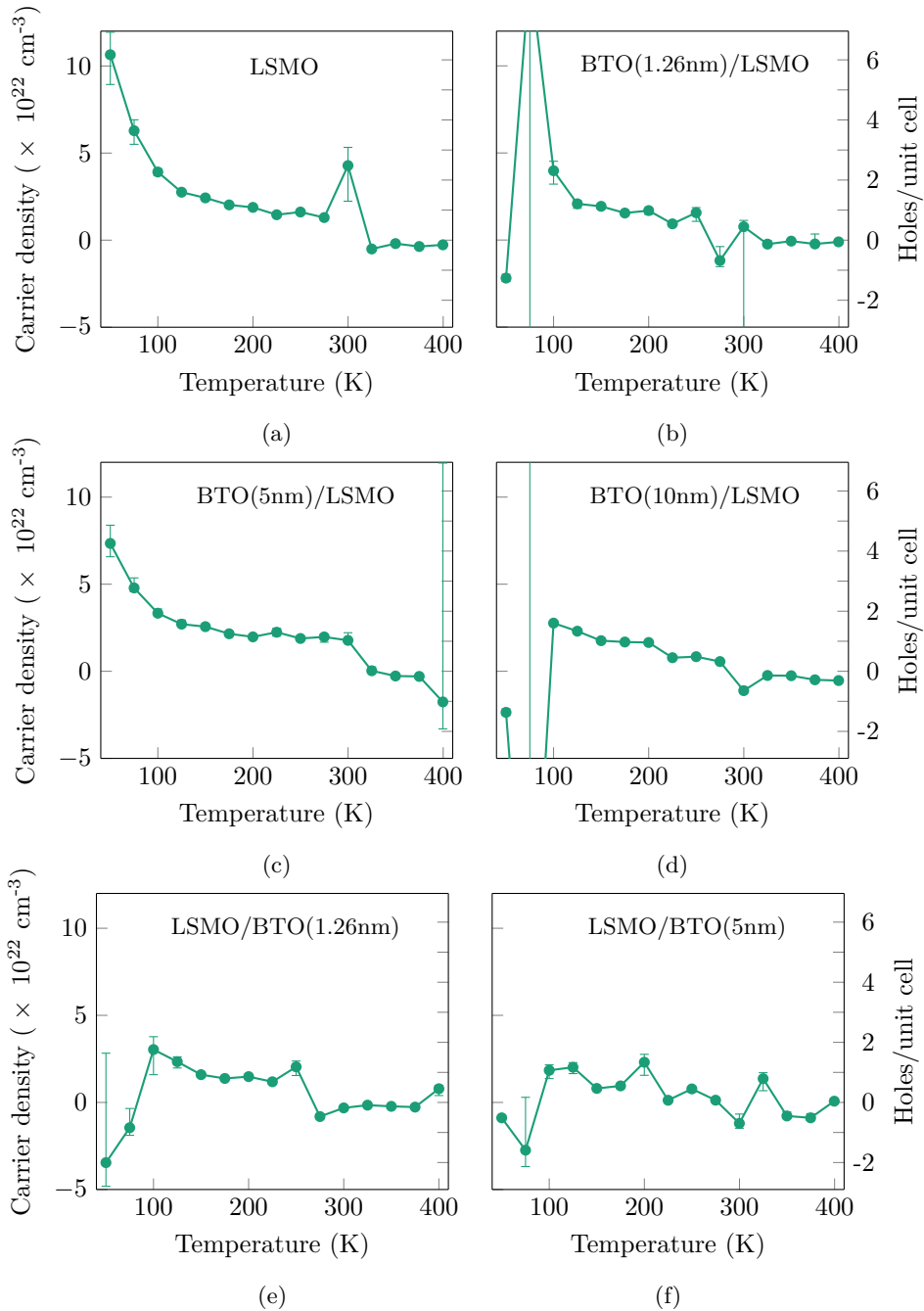


Figure 4.20: Calculated carrier densities for all of the samples structures. Some of the outlying data points are clearly caused by errors, but they were not removed in order to illustrate the behavior at low temperatures.

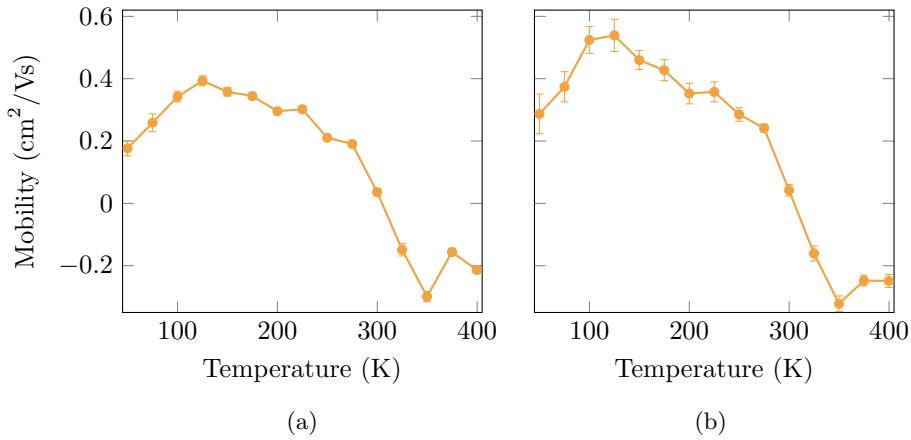


Figure 4.21: Carrier mobilities for the reference sample **(a)**, and BTO(5 nm)/LSMO **(b)**.

quantitative limitations of this work makes it risky to compare absolute values directly. The decreasing mobility below 125 K is caused by the abrupt increase of the carrier densities, which means that the behavior may be dominated by errors. To this date, no one has reported similar results at low temperatures.

5. Conclusion

An experimental technique was established that enable characterization of electrical transport properties of thin film heterostructures. An investigation of the electrical properties of BTO/LSMO-based heterostructures was intended to complement existing magnetic measurements in order to examine the effects of possible magnetoelectric coupling. The most crucial procedures were gold contact formation, wire bonding, electrical measurements and data processing. Important quantities such as resistivity, magnetoresistance, carrier density and mobility were examined in the temperature range 50 – 400 K. Since LSMO is a half-metal when doped with 30% Sr^{2+} and BTO an insulator, the obtained results were dominated by the properties of LSMO. On the other hand, the influence of the BTO layers was studied by comparing a series of heterostructures with varying BTO thicknesses and stacks of BTO and LSMO.

Van der Pauw's method formed the basis for the measurements, but a simplified version was adopted where the averaging procedure was omitted. The implications of using only a single bonding configuration were investigated for two of the samples. The results indicated that the resistivity was impacted to a larger degree than the magnetoresistance and the carrier density. This observation was attributed the fact that the resistivity is proportional to the measured resistances, while the other transport properties are deduced from relative differences.

Analyzing the Hall measurements was complicated by the anomalous Hall effect and instrument limitations. A one-band model was utilized where the slope of the Hall resistance in the linear region was taken as a measure of the ordinary Hall effect. Using this approach, the calculated carrier densities were considered to be most accurate for temperatures in the range 100 – 275 K. Close to or above T_C , the complexity of the Hall effect made it difficult to analyze the data. Below 100 K, the Hall resistances were comparable to the standard deviations of the electrical measurements, which decreased the credibility of the corresponding carrier densities.

The most detrimental errors were related to a simplified bonding scheme, instrument limitations, non-ideal contacts and unoptimized data processing. The combined uncertainties were expected to be up to 50% for the resistivity measurements, and below 10% for the magnetoresistances. However, the overall shape of the curves and the metal-insulator transitions temperatures were regarded as relatively accurate. The errors for the carrier densities were expected to lie below 20%

in the range 100 – 275 K. In summary, the established technique was suitable for preliminary and qualitative studies, but not for quantitative investigations.

The obtained resistivities and magnetoresistances were comparable to previous results for (001)-oriented LSMO. The reference sample exhibited a magnetoresistance close to -45% at 3 T, which surpasses the findings in similar studies. The carrier densities were between 1 – 2 holes/unit cell, which is more than the theoretical expectation of 0.3 holes/unit cell. This emphasized the fact that a one-band model is insufficient when examining the Hall effect in LSMO, and that a two-band model is required for more accurate results.

No clear indications of magnetoelectric coupling were discovered. Since the growth procedure was developed in parallel with this work, the films were of varying quality which may have been responsible for many of the observed differences. It is possible that a non-ideal epitaxial growth suppressed interactions between the oxygen octahedra at the interfaces. Given the relatively thin films that were studied, a potential strain-mediated coupling may have been of smaller magnitude than noise-related errors. The only observable trend indicated that LSMO films grown on top of BTO were of lower quality than those grown directly on the STO substrates.

5.1 Future Prospects

In future work, improving the general accuracy can most easily be accomplished by following der Pauw's method more closely. This implies a complete implementation of the averaging procedures using a rewiring approach. Furthermore, a consistent procedure should be introduced for the gold contact formation. A set of metal masks has already been developed, but these could not be used in this work because of improper sample dimensions. Substituting these for the manual tape masks would reduce the uncertainties related to the slightly varying contact sizes and shapes. With regard to optimization of the Hall measurements, the parameters related to the curve fits need to be improved. In the current state of the developed MATLAB scripts, choosing the optimal range for the curve fits has to be done manually. Developing an automated optimization procedure would improve the results and reduce the time consumption. At the end of this work, it was discovered that the ETO parameters could be further optimized, effectively reducing the ETO standard deviations by a factor of up to 20. Analogously to the curve fits, optimizing these parameters also has to be done manually. In order to avoid such problems, a possible solution is to use the VersaLab instrument solely for temperature and field control, and an external current source and voltmeter for the electrical measurements.

To conclude, the established technique was found to be suitable for qualitative studies of the electrical transport properties of thin films. If the above suggestions are implemented, it could prove to become a valuable tool for more detailed and quantitative studies in the future.

References

- [1] G. E. Moore. Cramming more components onto integrated circuits. 38(8), 1965.
- [2] Richard P. Feynman. There's Plenty of Room at the Bottom, February 1960.
- [3] Sieu D. Ha and Shriram Ramanathan. Adaptive oxide electronics: A review. *Journal of Applied Physics*, 110(7):071101, October 2011.
- [4] Wolfgang Arden, Michel Brillouët, Patrick Coge, Mart Graef, Bert Huizing, and Reinhard Mahnkopf. “More-than-Moore” White Paper. *International technology roadmap for semiconductors*, 2010.
- [5] A. P. Ramirez. Colossal magnetoresistance. *Journal of Physics: Condensed Matter*, 9:8171–8199, 1997.
- [6] J. G. Bednorz and K. A. Muller. Possible high T_C superconductivity in the Ba-La-Cu-O system. *Zeitschrift für Physik B Condensed Matter*, 64(2):189–193, June 1986.
- [7] S. Tehrani, J.M. Slaughter, M. Deherrera, B.N. Engel, N.D. Rizzo, J. Salter, M. Durlam, R.W. Dave, J. Janesky, B. Butcher, K. Smith, and G. Grynkewich. Magnetoresistive random access memory using magnetic tunnel junctions. *Proceedings of the IEEE*, 91(5):703–714, May 2003.
- [8] G. R. Fox, F. Chu, and T. Davenport. Current and future ferroelectric nonvolatile memory technology. *Journal of Vacuum Science & Technology B: Microelectronics and Nanometer Structures*, 19(5):1967, September 2001.
- [9] S. A. Wolf, D. D. Awschalom, R. A. Buhrman, J. M. Daughton, S. von Molnár, M. L. Roukes, A. Y. Chtchelkanova, and D. M. Treger. Spintronics: a spin-based electronics vision for the future. *Science (New York, N.Y.)*, 294(5546):1488–95, November 2001.
- [10] J.M. Daughton. GMR applications. *Journal of Magnetism and Magnetic Materials*, 192(2):334–342, February 1999.
- [11] R. Ramesh and N. A. Spaldin. Multiferroics: progress and prospects in thin films. *Nature materials*, 6(1):21–9, January 2007.

- [12] Manfred Fiebig. Revival of the magnetoelectric effect. *Journal of Physics D: Applied Physics*, 38(8):R123–R152, April 2005.
- [13] N. A. Spaldin and M. Fiebig. Materials science. The renaissance of magnetoelectric multiferroics. *Science (New York, N.Y.)*, 309(5733):391–2, July 2005.
- [14] Manuel Bibes and Agnès Barthélémy. Multiferroics: towards a magnetoelectric memory. *Nature materials*, 7(6):425–6, June 2008.
- [15] Yusuke Tokunaga, Nobuo Furukawa, Hideaki Sakai, Yasujiro Taguchi, Takahisa Arima, and Yoshinori Tokura. Composite domain walls in a multiferroic perovskite ferrite. *Nature materials*, 8(7):558–62, July 2009.
- [16] W. Prellier, M. P. Singh, and P. Murugavel. The single-phase multiferroic oxides: from bulk to thin film. *Journal of Physics: Condensed Matter*, 17(30):R803–R832, August 2005.
- [17] I. Hallsteinsen, J. E. Boschker, M. Nord, S. Lee, M. Rzechowski, P. E. Vullum, J. K. Grepstad, R. Holmestad, C. B. Eom, and T. Tybell. Surface stability of epitaxial $\text{La}_{0.7}\text{Sr}_{0.3}\text{MnO}_3$ thin films on (111)-oriented SrTiO_3 . *Journal of Applied Physics*, 113(18):183512, May 2013.
- [18] Aldo Raelarijaona and Huaxiang Fu. Various evidences for the unusual polarization behaviors in epitaxially strained (111) BaTiO_3 . *Journal of Applied Physics*, 115(5), February 2014.
- [19] M. K. Lee, T. K. Nath, C. B. Eom, M. C. Smoak, and F. Tsui. Strain modification of epitaxial perovskite oxide thin films using structural transitions of ferroelectric BaTiO_3 substrate. *Applied Physics Letters*, 77(2000):3547, 2000.
- [20] Ishrat Mubeen Dildar. *Conductance of perovskite oxide thin films and interfaces*. Universiteit Leiden, 2013.
- [21] N. Izyumskaya, Ya. Alivov, and H. Morkoç. Oxides, Oxides, and More Oxides: High- κ Oxides, Ferroelectrics, Ferromagnetics, and Multiferroics. *Critical Reviews in Solid State and Materials Sciences*, 34(February 2015):89–179, 2009.
- [22] Y. Harada, Y. Nakanishi, N. Yoshimoto, A. Yamaguchi, M. Nakamura, and M. Yoshizawa. Structural and magnetic properties of epitaxial fe/cu multilayers. *Journal of Magnetism and Magnetic Materials*, 272-276, 2004.
- [23] W. Eerenstein, M. Wiora, J. L. Prieto, J. F. Scott, and N. D. Mathur. Giant sharp and persistent converse magnetoelectric effects in multiferroic epitaxial heterostructures. *Nature materials*, 6(May):348–351, 2007.
- [24] A. Vailionis, H. Boschker, W. Siemons, E. P. Houwman, D. H. Blank, G. Rijnders, and G. Koster. Misfit strain accommodation in epitaxial ABO_3 perovskites: Lattice rotations and lattice modulations. *Physical Review B - Condensed Matter and Materials Physics*, 83(6):1–13, 2011.

- [25] P. G. Radaelli, G. Iannone, M. Marezio, H. Y. Hwang, S. W. Cheong, J. D. Jorgensen, and D. N. Argyriou. Structural effects on the magnetic and transport properties of perovskite $A_{1-x}A_xMnO_3$. *Physical Review B*, 56(13):8265–8276, 1997.
- [26] J. Gonzalez, M.A. Martin-Delgado, G. Sierra, and A.H. Vozmediano. *Quantum Electron Liquids and High-Tc Superconductivity*. 1995.
- [27] Duan Feng and Guojun Jin. *Introduction to Condensed Matter Physics, Volume 1*. World Scientific, 2005.
- [28] Myron B. Salamon and Marcelo Jaime. The physics of manganites: Structure and transport. *Reviews of Modern Physics*, 73(3):583–628, 2001.
- [29] M. Cesaria, P. Caricato, G. Maruccio, and M. Martino. LSMO - growing opportunities by PLD and applications in spintronics. *Journal of Physics: Conference Series*, 292:012003, 2011.
- [30] Clarence Zener. Interaction between the d -shells in the transition metals. ii. ferromagnetic compounds of manganese with perovskite structure. *Phys. Rev.*, 82:403–405, May 1951.
- [31] R. Aggarwal. *Integration of functional oxide thin film heterostructures with silicon (100) substrates*. PhD thesis, North Carolina State University, 2010.
- [32] K. Liu, X. Wu, K. Ahn, T. Sulchek, C. Chien, and John Xiao. Charge ordering and magnetoresistance in $Nd_{1-x}Ca_xMnO_3$ due to reduced double exchange. *Physical Review B*, 54(5):3007–3010, 1996.
- [33] L Méchin, S Wu, B Guillet, P Perna, C Fur, S Lebargy, C Adamo, D G Schlom, and J M Routoure. Experimental evidence of correlation between $1/f$ noise level and metal-to-insulator transition temperature in epitaxial $La_{0.7}Sr_{0.3}MnO_3$ thin films. *Journal of Physics D: Applied Physics*, 46(20):202001, 2013.
- [34] R. Bertacco, M. Riva, M. Cantoni, L. Signorini, and F. Ciccacci. Epitaxial $La_{2/3}Sr_{1/3}MnO_3$ thin films with metallic behavior above the Curie temperature. *Applied Physics Letters*, 86(25):1–3, 2005.
- [35] A. Millis, P. Littlewood, and B. Shraiman. Double Exchange Alone Does Not Explain the Resistivity of $La_{1-x}Sr_xMnO_3$. *Physical Review Letters*, 74(25):5144–5147, 1995.
- [36] Y. Tokura and Y. Tomioka. Colossal magnetoresistive manganites. *Journal of Magnetism and Magnetic Materials*, 200(1):1–23, 1999.
- [37] John B. Goodenough. Theory of the role of covalence in the perovskite-type manganites $[La,M(II)]MnO_3$. *Physical Review*, 100(2):564–573, 1955.
- [38] Rajendran. *Engineering Physics*. Tata McGraw-Hill Education, 2009.

- [39] J. M. Chaudhari, C. D. Patel, M. V. Patel, and M. N. Parmar. Giant Magneto Resistance (GMR). *International Journal of Advanced Engineering Technology*, 2011.
- [40] S Jin, T H Tiefel, M McCormack, R A Fastnacht, R Ramesh, and L H Chen. Thousandfold change in resistivity in magnetoresistive la-ca-mn-o films. *Science (New York, N.Y.)*, 264(5157):413–5, April 1994.
- [41] A.M. Haghiri-Gosnet and J.P. Renard. CMR manganites: physics, thin films and devices. *Journal of Physics D: Applied Physics*, 36(8):R127–R150, 2003.
- [42] C. A. Randall, R. E. Newnham, and L. E. Cross. History of the First Ferroelectric Oxide, BaTiO₃. Technical report, Materials Research Institute - The Pennsylvania State University, 2009.
- [43] Burcu Ertug. The Overview of The Electrical Properties of Barium Titanate. *American Journal of Engineering Research*, 2(08):1–7, 2013.
- [44] M.M. Vijatovic, J.D. Bobic, and B.D. Stojanovic. History and challenges of barium titanate: Part II. *Science of Sintering*, 40(3):235–244, 2008.
- [45] M.M. Vijatovic, J.D. Bobic, and B.D. Stojanovic. History and challenges of barium titanate: Part I. *Science of Sintering*, 40(2):155–165, 2008.
- [46] R. Surana. *MSc. Thesis*. PhD thesis, University of Cincinnati, 2004.
- [47] G. H. Kwei, A. C. Lawson, S. J. L. Billinge, and S. W. Cheong. Structures of the ferroelectric phases of barium titanate. *The Journal of Physical Chemistry*, 97(10):2368–2377, March 1993.
- [48] A. Von Hippel. Ferroelectricity, domain structure, and phase transitions of barium titanate. *Reviews of Modern Physics*, 22(3):221–237, 1950.
- [49] J. T. Heron, D. G. Schlom, and R. Ramesh. Electric field control of magnetism using BiFeO₃-based heterostructures. *Applied Physics Reviews*, 1(2):021303, June 2014.
- [50] W. Eerenstein, N. D. Mathur, and J. F. Scott. Multiferroic and magnetoelectric materials. *Nature*, 442(7104):759–65, August 2006.
- [51] L. D. Landau, J. S. Bell, M. J. Kearsley, L. P. Pitaevskii, E.M. Lifshitz, and J. B. Sykes. *Electrodynamics of Continuous Media*. 1984.
- [52] W. C. Röntgen. Über die durch Bewegung eines im homogenen electrischen Felde Befindlichen Dielectricums hervorgerufene electrodynamische Kraft. *Ann. d. Phys*, 3(35):264, 1888.
- [53] Harold A. Wilson. On the Electric Effect of Rotating a Dielectric in a Magnetic Field. *Philosophical Transactions of the Royal Society A: Mathematical, Physical and Engineering Sciences*, 204(129):121–137, 1905.

- [54] P. Curie. Sur la symétrie dans les phénomènes physiques, symétrie d'un champ électrique et d'un champ magnétique. *Journal de Physique Théorique et Appliquée*, 3(1):393–415, 1894.
- [55] V. J. Folen, G. T. Rado, and E. W. Stalder. Anisotropy of the magnetoelectric effect in Cr_2O_3 . *Phys. Rev. Lett.*, 6:607–608, Jun 1961.
- [56] Daniel Khomskii. Classifying multiferroics: Mechanisms and effects. *Physics*, 2:20, March 2009.
- [57] Sang-Wook Cheong and Maxim Mostovoy. Multiferroics: a magnetic twist for ferroelectricity. *Nature materials*, 6(1):13–20, January 2007.
- [58] Yoshinori Tokura and Shinichiro Seki. Multiferroics with spiral spin orders. *Advanced materials (Deerfield Beach, Fla.)*, 22(14):1554–65, April 2010.
- [59] Yaojin Wang, Jiefang Li, and D. Viehland. Magnetoelectrics for magnetic sensor applications: status, challenges and perspectives. *Materials Today*, 17(6):269–275, July 2014.
- [60] Hans Schmid. Some symmetry aspects of ferroics and single phase multiferroics. *Journal of Physics: Condensed Matter*, 20(43):434201, October 2008.
- [61] N. A. Hill. Why Are There so Few Magnetic Ferroelectrics? *The Journal of Physical Chemistry B*, 104(29):6694–6709, July 2000.
- [62] Hans Schmid. Introduction to the proceedings of the 2nd international conference on magnetoelectric interaction phenomena in crystals, MEIPIC-2. *Ferroelectrics*, 161(1):1–28, 1994.
- [63] G. Srinivasan. Magnetoelectric Composites. *Annual Review of Materials Research*, 40:153–178, 2010.
- [64] Gustau Catalan and James F. Scott. Physics and Applications of Bismuth Ferrite. *Advanced Materials*, 21(24):2463–2485, June 2009.
- [65] T. Zhao, A. Scholl, F. Zavaliche, K. Lee, M. Barry, A. Doran, M. P. Cruz, Y. H. Chu, C. Ederer, N. Spaldin, R. R. Das, D. M. Kim, S. H. Baek, C. B. Eom, and R. Ramesh. Electrical control of antiferromagnetic domains in multiferroic BiFeO_3 films at room temperature. *Nature materials*, 5(10):823–9, October 2006.
- [66] Chuanwei Huang and Lang Chen. Effects of Interfaces on the Structure and Novel Physical Properties in Epitaxial Multiferroic BiFeO_3 Ultrathin Films. *Materials*, 7(7):5403–5426, July 2014.
- [67] Ce-Wen Nan, M. I. Bichurin, Shuxiang Dong, D. Viehland, and G. Srinivasan. Multiferroic magnetoelectric composites: Historical perspective, status, and future directions. *Journal of Applied Physics*, 103(3):031101, 2008.

- [68] J. Van Den Boomgaard, A. M. J. G. Van Run, and J. Van Suchtelen. Magnetolectricity in piezoelectric-magnetostrictive composites. *Ferroelectrics*, 10(1), February 1976.
- [69] Jung-ho Ryu, Shashank Priya, Kenji Uchino, and Hyoun Ee Kim. Magnetolectric effect in composites of magnetostrictive and piezoelectric materials. *Journal of Electroceramics*, 8:107–119, 2002.
- [70] Yao Wang, Jiamian Hu, Yuanhua Lin, and Ce-Wen Nan. Multiferroic magnetolectric composite nanostructures. *NPG Asia Materials*, 2(2):61–68, April 2010.
- [71] Sergey Lopatin, Irina Lopatina, and Inna Lisnevskaya. Magnetolectric PZT/ferrite composite material. *Ferroelectrics*, 162(1):63, February 1994.
- [72] Girish Harshe, J. P. Dougherty, and R. E. Newnham. Theoretical modelling of multilayer magnetolectric composites. *International journal of applied electromagnetics in materials*, 4(2):145–159, 1993.
- [73] J. van Suchtelen. Product properties – new application of composite materials. *Philips Research Reports*, 27:28, 1972.
- [74] Ce W. Nan. Magnetolectric effect in composites of piezoelectric and piezomagnetic phases. *Physical Review B*, 50(9):6082–6088, 1994.
- [75] Guoxi Liu, Xiaotian Li, Jianguo Chen, Huaduo Shi, Wenlei Xiao, and Shuxiang Dong. Colossal low-frequency resonant magnetomechanical and magnetolectric effects in a three-phase ferromagnetic/elastic/piezoelectric composite. *Applied Physics Letters*, 101(2012), 2012.
- [76] H. L. Wang and B. Liu. The theoretical ultimate magnetolectric coefficients of magnetolectric composites by optimization design. *Journal of Applied Physics*, 115, 2014.
- [77] Aldo Raeliarijaona and Huaxiang Fu. Various evidences for the unusual polarization behaviors in epitaxially strained (111) BaTiO₃. *Journal of Applied Physics*, 115(5):054105, February 2014.
- [78] Paolo Perna. *Colossal magnetoresistive manganites for sensing applications*. PhD thesis, 2008.
- [79] Igor Žutić, Jaroslav Fabian, and S. Das Sarma. Spintronics: Fundamentals and applications. *Reviews of Modern Physics*, 76(2):323–410, 2004.
- [80] J. M. De Teresa. Role of Metal-Oxide Interface in Determining the Spin Polarization of Magnetic Tunnel Junctions. *Science*, 286(5439):507–509, 1999.
- [81] F. J. Wang, C. G. Yang, Z. Vally Vardeny, and X. G. Li. Spin response in organic spin valves based on La_{2/3}Sr_{1/3}MnO₃ electrodes. *Physical Review B*, 75(24):245324, June 2007.

- [82] Z H Xiong, Di Wu, Z Vally Vardeny, and Jing Shi. Giant magnetoresistance in organic spin-valves. *Nature*, 427(6977):821–4, February 2004.
- [83] Tho D Nguyen, Golda Hukic-Markosian, Fujian Wang, Leonard Wojcik, Xiao-Guang Li, Eitan Ehrenfreund, and Z Vally Vardeny. Isotope effect in spin response of pi-conjugated polymer films and devices. *Nature materials*, 9(4):345–52, April 2010.
- [84] Luis E Hueso, José M Pruneda, Valeria Ferrari, Gavin Burnell, José P Valdés-Herrera, Benjamin D Simons, Peter B Littlewood, Emilio Artacho, Albert Fert, and Neil D Mathur. Transformation of spin information into large electrical signals using carbon nanotubes. *Nature*, 445(7126):410–3, January 2007.
- [85] Aiping Chen, Zhenxing Bi, Chen Fong Tsai, Joonhwan Lee, Qing Su, Xinghang Zhang, Quanxi Jia, Judith L. MacManus-Driscoll, and Haiyan Wang. Tunable low-field magnetoresistance in (La_{0.7}Sr_{0.3}MnO₃)_{0.5}:(ZnO)_{0.5} self-assembled vertically aligned nanocomposite thin films. *Advanced Functional Materials*, 21(13):2423–2429, 2011.
- [86] Sayani Majumdar, H. Huhtinen, H. S. Majumdar, and P. Paturi. Stress and defect induced enhanced low field magnetoresistance and dielectric constant in La_{0.7}Sr_{0.3}MnO₃ thin films. *Journal of Alloys and Compounds*, 512(1):332–339, 2012.
- [87] H. Lu, T. A. George, Y. Wang, I. Ketsman, J. D. Burton, C. W. Bark, S. Ryu, D. J. Kim, J. Wang, C. Binek, P. A. Dowben, A. Sokolov, C. B. Eom, E. Y. Tsybal, and A. Gruverman. Electric modulation of magnetization at the BaTiO₃/La_{0.67}Sr_{0.33}MnO₃ interfaces. *Applied Physics Letters*, 100(23):0–5, 2012.
- [88] Ting Xian Li, Ming Zhang, Zhou Hu, Kuo She Li, Dun Bo Yu, and Hui Yan. Preparation and Study of Strong Magnetoelectric Coupling on Multiferroic BaTiO₃/La_{0.7}Sr_{0.3}MnO₃ Bilayer Heterostructure. *Advanced Materials Research*, 295-297(2011):2015–2019, 2011.
- [89] Srinivasa Rao Singamaneni, Wu Fan, J. T. Prater, and J. Narayan. Magnetic properties of BaTiO₃/La_{0.7}Sr_{0.3}MnO₃ thin films integrated on Si(100). *Journal of Applied Physics*, 116(22):224104, December 2014.
- [90] Srinivasa Rao Singamaneni, Sandhyarani Punugupati, John T. Prater, Frank Hunte, and Jagdish Narayan. Ferroelectric and ferromagnetic properties in BaTiO₃ thin films on Si (100). *Journal of Applied Physics*, 116(9):094103, September 2014.
- [91] Edward Ramsden. *Hall-Effect Sensors: Theory and Application*. Newnes, 2011.
- [92] R.S. Popovic. *Hall Effect Devices: Magnetic Sensors and Characterization of Semiconductors*. CRC Press, 1991.

- [93] E. H. Hall. On a new Action of the Magnet on Electric Currents. *American Journal of Mathematics*, 2(3), 1879.
- [94] Charles Kittel. *Introduction to Solid State Physics, Eighth Edition*. 2005.
- [95] Dieter K. Schroder. In *Semiconductor Material and Device Characterization*. 2006.
- [96] Manijeh Razeghi. In *Fundamentals of Solid State Engineering*, chapter 8, page 792. Springer Science & Business Media, 2009.
- [97] G. Jakob, F. Martin, W. Westerburg, and H. Adrian. Evidence of charge-carrier compensation effects in $\text{La}_{0.67}\text{Ca}_{0.33}\text{MnO}_3$. *Physical Review B*, 57(17):10252–10255, 1998.
- [98] Edwin H. Hall. *Philos. Mag.*, 12(157), 1881.
- [99] Naoto Nagaosa, Jairo Sinova, Shigeki Onoda, A. H. MacDonald, and N. P. Ong. Anomalous Hall effect. *Reviews of Modern Physics*, 82(2):1539–1592, 2010.
- [100] P. Matl, Y. F. Ong, N. P. and Yan, Y. Q. Li, and D. Studebaker. Hall effect of the colossal magnetoresistance manganite $\text{La}_{1-x}\text{Ca}_x\text{MnO}_3$. *Physical Review B*, 57(17):248–251, 1998.
- [101] Robert Karplus and J. M. Luttinger. Hall effect in ferromagnetics. *Phys. Rev.*, 95:1154–1160, Sep 1954.
- [102] J. Smit. The spontaneous hall effect in ferromagnetics I. *Physica*, 21(6-10):877–887, January 1955.
- [103] J. Smit. The spontaneous hall effect in ferromagnetics II. *Physica*, 24(1-5):39–51, January 1958.
- [104] L. Berger. Side-Jump Mechanism for the Hall Effect of Ferromagnets. *Physical Review B*, 2(11):4559–4566, 1970.
- [105] A Asamitsu and Y. Tokura. Hall effect in $\text{La}_{1-x}\text{Sr}_x\text{MnO}_3$. *Physical Review B*, 58(1):47–50, 1998.
- [106] S. H. Chun, M. B. Salamon, and P. D. Han. Hall effect of $\text{La}_{2/3}(\text{Ca,Pb})_{1/3}\text{MnO}_3$ single crystals. *Journal of Applied Physics*, 85(8):5573, 1999.
- [107] L. J. van der Pauw. A method of measuring specific resistivity and Hall coefficient of discs of arbitrary shape. *Philips Research Reports*, 13(1):1–9, 1958.
- [108] Leo J. van der Pauw. A method of measuring the resistivity and Hall coefficient on lamellae of arbitrary shape. *Philips Technical Review*, 20:220–224, 1958.

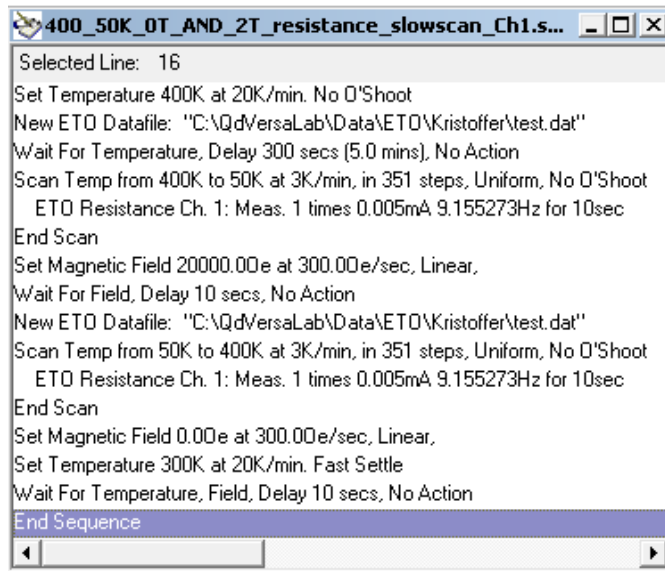
- [109] Lake Shore. Appendix a - Hall Effect Measurements. *7500/9500 Series Hall System User's Manual*, pages 1–18.
- [110] R. K. Rajput. In *A Textbook of Electrical Engineering*, chapter 2, page 690. Firewall Media, 2004.
- [111] U. A. Bakshi and A. V. Bakshi. Network Analysis. In *Network Analysis*, chapter 3. Technical Publications, 2009.
- [112] Radomir Džakula, Slavica Savi, and Goran Stojanovi. Investigation of electrical characteristics of different ceramic samples using Hall effect measurement. *Processing and Application of Ceramics*, 2:33–37, 2008.
- [113] Alexander J E Rettie, Heung Chan Lee, Luke G Marshall, Jung-Fu Lin, Cigdem Capan, Jeffrey Lindemuth, John S McCloy, Jianshi Zhou, Allen J Bard, and C Buddie Mullins. Combined charge carrier transport and photoelectrochemical characterization of BiVO₄ single crystals: intrinsic behavior of a complex metal oxide. *Journal of the American Chemical Society*, 135(30):11389–96, July 2013.
- [114] Josef Náhlík, Irena Kašpárková, and Pemysl Fitl. Study of quantitative influence of sample defects on measurements of resistivity of thin films using van der Pauw method. *Measurement*, 44(10):1968–1979, December 2011.
- [115] David C. Look. In *Electrical Characterization of GaAs Materials and Devices*, chapter 2. 1992.
- [116] Gaiser Precision Bonding Tools CoorsTek Inc. Wedge Bonding.
- [117] H. Boschker, M. Huijben, A. Vailionis, J. Verbeeck, S. van Aert, M. Luysberg, Bals, G. van Tendeloo, E. P. Houwman, G. Koster, D. H. Blank, and G. Rijnders. Optimized fabrication of high quality La_{0.67}Sr_{0.33}MnO₃ thin films considering all essential characteristics. *J. Phys. D: Appl. Phys.*, 205001(44), 2011.
- [118] Baomin Wang, Lu You, Peng Ren, Xinmao Yin, Yuan Peng, Bin Xia, Lan Wang, Xiaojiang Yu, Sock Mui Poh, Ping Yang, Guoliang Yuan, Lang Chen, Andriwo Rusydi, and Junling Wang. Oxygen-driven anisotropic transport in ultra-thin manganite films. *Nature communications*, 4(May 2012):2778, 2013.
- [119] S. Nakatsuji, Y. Machida, J. J. Ishikawa, S. Onoda, Y. Karaki, T. Tayama, and T. Sakakibara. Spontaneous Hall Effect in the Spin Liquid Phase of Pr₂Ir₂O₇. *Journal of Physics: Conference Series*, 320:12056, 2011.
- [120] Frank Ortmann, Stephan Roche, and Sergio O. Valenzuela. Topological Insulators: Fundamentals and Perspectives. In *Topological Insulators: Fundamentals and Perspectives*, chapter 14, page 360. John Wiley & Sons, 2015.
- [121] J. E. Nunez-Regueiro, D. Gupta, and A. M. Kadin. Hall effect and giant magnetoresistance in lanthanum manganite thin films. *Journal of Applied Physics*, 79(8):5179, 1996.

- [122] Liuqi Yu, Lingfei Wang, Xiaohang Zhang, W. B. Wu, S von Molnár, Z Fisk, and P. Xiong. Signatures of electronic phase separation in the Hall effect of anisotropically strained $\text{La}_{0.67}\text{Ca}_{0.33}\text{MnO}_3$ films. *New Journal of Physics*, 15(11):113057, 2013.
- [123] W. Westerburg, F. Martin, P.J.M. van Bentum, J.A.A.J. Perenboom, and G. Jakob. Charge-carrier density collapse in $\text{La}_{0.67}\text{Ca}_{0.33}\text{MnO}_3$ and $\text{La}_{0.67}\text{Sr}_{0.33}\text{MnO}_3$ epitaxial thin film. *The European Physical Journal B*, 14(3):509–513, March 2000.
- [124] T. Wutscher and F. J. Giessibl. Note: In situ cleavage of crystallographic oriented tips for scanning probe microscopy. *The Review of scientific instruments*, 82(2):026106, March 2011.
- [125] P Perna, L Méchin, M P Chauvat, P Ruterana, Ch Simon, and U Scotti di Uccio. High Curie temperature for $\text{La}_{0.7}\text{Sr}_{0.3}\text{MnO}_3$ thin films deposited on CeO_2 /YSZ-based buffered silicon substrates. *Journal of physics. Condensed matter : an Institute of Physics journal*, 21:306005, 2009.
- [126] Yayoi Takamura, Rajesh V Chopdekar, Andreas Scholl, Andrew Doran, J Alexander Liddle, Bruce Harteneck, and Yuri Suzuki. Tuning magnetic domain structure in nanoscale $\text{La}_{0.7}\text{Sr}_{0.3}\text{MnO}_3$ islands. *Nano letters*, 6(6):1287–1291, 2006.
- [127] Rajesh V. Chopdekar, Elke Arenholz, and Y. Suzuki. *Physical Review B - Condensed Matter and Materials Physics*, (10):1–7.
- [128] Z G Sheng, M Nakamura, W Koshibae, T Makino, Y Tokura, and M Kawasaki. Magneto-tunable photocurrent in manganite-based heterojunctions. *Nature communications*, 5:4584, January 2014.
- [129] Y. M. Nikolaenko, V. N. Varyukhin, Y. V. Medvedev, N. B. Efros, I. V. Zhikharev, S. V. Kara-Murza, and A. A. Tikhii. Optimum oxygen content in $\text{La}_{0.7}\text{Sr}_{0.3}\text{MnO}_3$ thin films. *ArXiv e-prints*, November 2011.
- [130] Pankaj Jha, Timothy D. Sands, Philip Jackson, Cory Bomberger, Tela Favaloro, Stephen Hodson, Joshua Zide, Xianfan Xu, and Ali Shakouri. Cross-plane thermoelectric transport in p-type $\text{La}_{0.67}\text{Sr}_{0.33}\text{MnO}_3/\text{LaMnO}_3$ oxide metal/semiconductor superlattices. *Journal of Applied Physics*, 113(19):193702, May 2013.
- [131] Jie Qiu, Kui-juan Jin, Peng Han, Hui-bin Lu, Chun-lian Hu, Bao-ping Wang, and Guo-zhen Yang. A theoretical study on the transport property of the $\text{La}_{0.7}\text{Sr}_{0.3}\text{MnO}_3/\text{Si}$ p-n heterojunction. *Europhysics Letters (EPL)*, 79(5):57004, September 2007.

Appendix A: ETO Scripts

Below three typical examples are shown for the ETO scripts. The script in Fig. A.1 was used to obtain the resistivity and magnetoresistance as a function of temperature, Fig. A.2 for magnetoresistance vs. field and Fig. A.3 for Hall measurements.

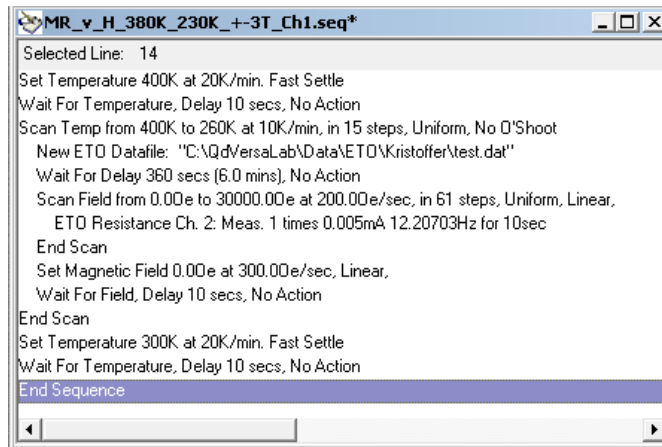
A.1 Resistivity and MR vs. Temperature



```
Selected Line: 16
Set Temperature 400K at 20K/min. No O'Shoot
New ETO Datafile: "C:\QdVersaLab\Data\ETO\Kristoffer\test.dat"
Wait For Temperature, Delay 300 secs (5.0 mins), No Action
Scan Temp from 400K to 50K at 3K/min, in 351 steps, Uniform, No O'Shoot
  ETO Resistance Ch. 1: Meas. 1 times 0.005mA 9.155273Hz for 10sec
End Scan
Set Magnetic Field 20000.00e at 300.00e/sec, Linear,
Wait For Field, Delay 10 secs, No Action
New ETO Datafile: "C:\QdVersaLab\Data\ETO\Kristoffer\test.dat"
Scan Temp from 50K to 400K at 3K/min, in 351 steps, Uniform, No O'Shoot
  ETO Resistance Ch. 1: Meas. 1 times 0.005mA 9.155273Hz for 10sec
End Scan
Set Magnetic Field 0.00e at 300.00e/sec, Linear,
Set Temperature 300K at 20K/min. Fast Settle
Wait For Temperature, Field, Delay 10 secs, No Action
End Sequence
```

Figure A.1: Example of ETO script used to obtain data in order to calculate resistivity and magnetoresistance vs. temperature.

A.2 MR vs. Magnetic Field

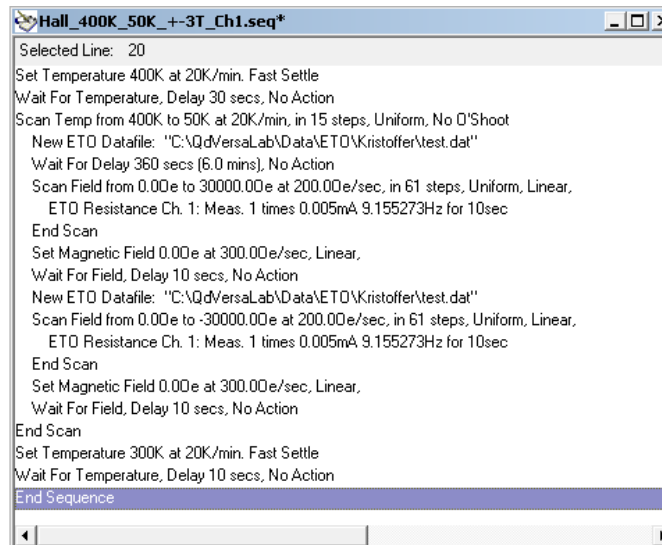


```

MR_v_H_380K_230K_+-3T_Ch1.seq*
Selected Line: 14
Set Temperature 400K at 20K/min. Fast Settle
Wait For Temperature, Delay 10 secs, No Action
Scan Temp from 400K to 260K at 10K/min, in 15 steps, Uniform, No D'Shoot
  New ETO Datafile: "C:\QdVersaLab\Data\ETO\Kristoffer\test.dat"
  Wait For Delay 360 secs (6.0 mins), No Action
  Scan Field from 0.00e to 30000.00e at 200.00e/sec, in 61 steps, Uniform, Linear,
    ETO Resistance Ch. 2: Meas. 1 times 0.005mA 12.20703Hz for 10sec
  End Scan
  Set Magnetic Field 0.00e at 300.00e/sec, Linear,
  Wait For Field, Delay 10 secs, No Action
End Scan
Set Temperature 300K at 20K/min. Fast Settle
Wait For Temperature, Delay 10 secs, No Action
End Sequence
  
```

Figure A.2: ETO script used to obtain magnetoresistance as a function of magnetic field at a range of selected temperatures.

A.3 Hall Measurements



```

Hall_400K_50K_+-3T_Ch1.seq*
Selected Line: 20
Set Temperature 400K at 20K/min. Fast Settle
Wait For Temperature, Delay 30 secs, No Action
Scan Temp from 400K to 50K at 20K/min, in 15 steps, Uniform, No D'Shoot
  New ETO Datafile: "C:\QdVersaLab\Data\ETO\Kristoffer\test.dat"
  Wait For Delay 360 secs (6.0 mins), No Action
  Scan Field from 0.00e to 30000.00e at 200.00e/sec, in 61 steps, Uniform, Linear,
    ETO Resistance Ch. 1: Meas. 1 times 0.005mA 9.155273Hz for 10sec
  End Scan
  Set Magnetic Field 0.00e at 300.00e/sec, Linear,
  Wait For Field, Delay 10 secs, No Action
  New ETO Datafile: "C:\QdVersaLab\Data\ETO\Kristoffer\test.dat"
  Scan Field from 0.00e to -30000.00e at 200.00e/sec, in 61 steps, Uniform, Linear,
    ETO Resistance Ch. 1: Meas. 1 times 0.005mA 9.155273Hz for 10sec
  End Scan
  Set Magnetic Field 0.00e at 300.00e/sec, Linear,
  Wait For Field, Delay 10 secs, No Action
End Scan
Set Temperature 300K at 20K/min. Fast Settle
Wait For Temperature, Delay 10 secs, No Action
End Sequence
  
```

Figure A.3: ETO script for Hall measurements. Hall resistance, carrier density and mobility may be deduced from the data measured by this script.

Appendix B: MATLAB Scripts

In this appendix complete versions of the MATLAB scripts and functions that were developed are included. The codes are divided into sections according to their area of use.

B.1 Resistivity and MR vs. Temperature

MR vs Tv5

```
1 %% Magneto-resistance and resistivity calculations
2 % Calculates magneto-resistance and resistivity as a function of ...
   temperature
3 % using van der Pauw's method.
4
5 % Input data format:
6 % Requires resistance to be measured in a give temperature interval ...
   in zero
7 % field and at a finite field value. Assumes the use of two bonding
8 % configurations, i.e. two zero field data sets and two finite field...
   sets.
9 % If only one configuration is used: set1=set3 and set2=set4. See ...
   ETO
10 % script "resistivity and MR vs temperature"
11 clear all
12 close all
13 clc
14 hold on
15
16 %% Switches for plots and save functions
17 plot_R_vs_T_switch = 1;
18 plot_MR_vs_T_switch = 1;
19 write_MR_to_file = 0;
20 home = 0; %Determines plot placement (1 vs 2 monitors)
21
22 %% Measurement specific constants
23 thickness = 10e-7; % Sets thickness of LSMO needed for resistivity ...
   calculation
24 Ch_num = 1; % ETO channel used for the measurements
25 R_col = 7;
26 if Ch_num == 1
27     R_col = 7;
```

```

28 else
29     R_col = 27;
30 end
31
32 %% Program begins
33 % Imports data from e.g. 50-400 K in zero field (set1) and 2T (set2)...
34   . Set3
35 % and set4 corresponds to alternate bonding configurations
36 set1 = importdata('Data/R_Tsweep\5nmBTO_10nmLSMO/5...
37   nmBTO_10nmLSMO_0T_400_50K_00000.dat',' ',18); % With magnetic ...
38   field
39 set2 = importdata('Data/R_Tsweep\5nmBTO_10nmLSMO/5...
40   nmBTO_10nmLSMO_2T_400_50K_00000.dat',' ',18); % Without ...
41   magnetic field
42 set3 = importdata('Data/R_Tsweep\5nmBTO_10nmLSMO/5...
43   nmBTO_10nmLSMO_0T_400_50K_00000.dat',' ',18); % With magnetic ...
44   field
45 set4 = importdata('Data/R_Tsweep\5nmBTO_10nmLSMO/5...
46   nmBTO_10nmLSMO_2T_400_50K_00000.dat',' ',18); % Without ...
47   magnetic field
48
49 element_num = length(set1.data(:,1));
50
51 % Calculates sheet resistance and resistivity for all points
52 [ T_data_res1, T_data_res2, sheet_resistance1, sheet_resistance2, ...
53   resistivity1, resistivity2] = resistivity_calc( set1,set2,set3,...
54   set4,thickness,R_col);
55
56 %Calculates magnetoresistance as a function of temperature
57 [ T_data_MR, MR_values] = MR_calc2(T_data_res1, T_data_res2, ...
58   resistivity1, resistivity2);
59
60 % Finds Metal-insulataor temperature as peak of R vs T curve
61 % Assumes only one peak, reports first peak value
62 for i = 2:length(resistivity1)
63     if resistivity1(i) > resistivity1(i-1) && resistivity1(i) > ...
64       resistivity1(i+1)
65         TMI = T_data_res1(i)
66         break;
67     end
68 end
69
70 % Calculates sheet resistance Rs at specific temperatures to be used...
71   for mobility calculations
72 % using the Hall script.
73 T=400; %Start temperature for Hall measurements
74 n=1;
75 T_step=25; % Size of T steps used when measuring Hall effect
76 while T>49
77     index = dsearchn(T_data_res1',T);
78     Rs(n) = sheet_resistance1(index);
79     n=n+1;
80     T=T-T_step;
81 end
82
83 % Plots resistivity vs T
84 if plot_R_vs_T_switch

```

```

71     plot_R_vs_T(1,home,T_data_res1,T_data_res2,resistivity1,...
              resistivity2);
72 end
73
74 % Plots MR vs T
75 if plot_MR_vs_T_switch
76     plot_MR_vs_T(2,home,T_data_MR,MR_values);
77 end

```

MR calc2

```

1 function [ T_data_MR MR_values] = MR_calc2(T_data_res1, T_data_res2,...
      resistivity1, resistivity2)
2 % Calculates magnetoresistance as  $(R(0) - R(H))/R(H)$ , but the plots ...
      report
3 % negative values
4
5 %----- List of arguments:-----
6 % T_data_res1: Temperatures at zero field
7 % T_data_res2: Temperatures at finite field
8 % resistivity1: resistivity at zero field
9 % resistivity2: resistivity at finite field
10
11 element_num = length(resistivity1);
12 n=1;
13 % Loops through all resistances at their corresponding temperatures ...
      at zero
14 % field. Finds the closest temperatuer at a finite field and ...
      calculates the
15 % magnetoresistance.
16 for i = 1:element_num
17     ind_closest = dsearchn(T_data_res2',T_data_res1(i));
18     if abs(T_data_res1(i)-T_data_res2(ind_closest))<.5
19         T_data_MR(n) = (T_data_res1(i)+T_data_res2(ind_closest))/2;
20         MR_values(n) = (resistivity1(i)-resistivity2(ind_closest))/...
              resistivity2(ind_closest)*100;
21         n=n+1;
22     end
23 end
24 end

```

plot MR vs T

```

1 function [ ] = plot_MR_vs_T( fig_num,home,T_data_MR,MR_values )
2 % Function that plots resistivity vs T
3
4 %----- List of arguments:-----
5 % fig_num: Number of figure window generated by plot
6 % home: Decides position of plot windows
7 % T_data: list of temperatures for MR values
8 % MR_values: array of calculated MR values
9
10 figure(fig_num)

```

```

11 [linestyles,MarkerEdgeColors,Markers,MarkerFaceColor ] =...
    set_linestyles(10); % Imports line colors and markers for 'n' ...
    lines
12 style_type = 3; %select style, choose between the linestyles ...
    intiated above
13
14 if home
15     set(gcf,'position',[50,200,600,400]); %Home PC
16 else
17     set(gcf,'position',[-650,500,600,400]);
18 end
19
20 %Plots MR vs temperature
21 plot(T_data_MR,MR_values,[ '-' Markers(style_type)],'Color',...
    MarkerEdgeColors{style_type},'MarkerFaceColor',MarkerFaceColor{...
    style_type}); % Plots ME vs T
22 xlim ([min(T_data_MR)-10 max(T_data_MR)+10]); % x range
23 title('1.26nm BTO/10nm LSMO','FontSize',18);
24 xlabel('Temperature (K)','FontSize',20 );
25 ylabel('MR (%)','FontSize',20)
26 set(gca,'FontSize',20); %sets tick fontsize
27 box on; % Turns on box around plots
28 end

```

plot R vs T

```

1 function [ ] = plot_R_vs_T( fig_num,home,T_data_res1,T_data_res2,...
    resistivity_set1,resistivity_set2)
2 % Function that plots resistivity vs T
3
4 %----- List of arguments:-----
5 % fig_num: number of figure window generated by plot
6 % home: Switch to decide position of plot windows
7 % T_data_res1: Temperatures at zero field
8 % T_data_res2: Temperatures at finite field
9 % resistivity_set1: resistivity at zero field
10 % resistivity_set2: resistivity at finite field
11
12 figure(fig_num)
13 hold on
14 [linestyles,MarkerEdgeColors,Markers,MarkerFaceColor ] =...
    set_linestyles(10); % Imports line colors and markers for 'n' ...
    lines
15 style_type = 1; %select style, choose between the linestyles ...
    intiated above
16
17 if home
18     set(gcf,'position',[50,700,600,400]); %Home PC
19 else
20     set(gcf,'position',[-1250,500,600,400]);
21 end
22
23 % Plots resistivities with and without external field
24 plot(T_data_res1,resistivity_set1,[ '-' Markers(style_type)],'Color'...
    ,MarkerEdgeColors{style_type},'MarkerFaceColor',MarkerFaceColor...
    {style_type}) % Plots R vs T for R(0) using green lines with ...

```



```

stars
25 plot(T_data_res2,resistivity_set2,[ '-' Markers(style_type)],'Color'...
    , 'b','MarkerFaceColor','b') % Plots R vs T for R(H) using green...
    lines with stars
26 title('1.26nm BTO/10nmLSMO','FontSize',18);
27 xlim ([min(T_data_res1)-10 max(T_data_res1)+10]); % x range
28 xlabel('Temperature (K)','FontSize',20);
29 ylabel('\rho (m\Omega-cm)','FontSize',20)
30 h_legend = legend('0 T', '2 T','Location','northwest'); % makes a ...
    handle to edit properties
31 set(h_legend,'fontsize',20,'position', [0.75,0.6,0.09,0.07]); % ...
    position [left,bottom,width,height]
32 set(gca,'FontSize',20); %sets tick fontsize
33 box on; % Turns on box around plots
34 end

```

vdP solver

```

1 function [ sheet_resistance , resistivity ] = vdP_solver(R1,R2,...
    thickness )
2 % Solves van der Pauw's formula numerically and returns sheet ...
    resistance
3 % and resistivity
4 % Algorithm taken form http://www.nist.gov/pml/div683/...
    hall_algorithm.cfm
5
6 %----- List of arguments:-----
7 % R1: resistance 1st bonding configuration
8 % R2: resistance 2nd bonding configuration
9 % thickness: sample thickness
10
11 delta = 0.00005; % end condition
12 z0 = 2*log(2)/(pi*(R1+R2));
13 zi = delta+1;
14 while(zi-z0)/zi>delta
15     yi = 1/exp(pi*z0*R1)+1/exp(pi*z0*R2);
16     zi = z0 - ((1-yi)/pi)/(R1*exp(pi*z0*R1) +R2*exp(pi*z0*R2));
17     z0=zi;
18 end
19 sheet_resistance = 1/zi;
20 resistivity = sheet_resistance*thickness*1e3;
21 end

```

resistivity calc

```

1 function [ T_data_res1 T_data_res2 sheet_resistance1 ...
    sheet_resistance2 resistivity1 resistivity2] = ...
    resistivity_calc( set1,set2,set3,set4,thickness,R_col)
2
3 element_num = length(set1.data(:,1));
4 n=1;
5 for i = 1:element_num
6     ind_closest1 = dsearchn(set3.data(:,3),set1.data(i,3));
7     if abs(set1.data(i,3)-set3.data(ind_closest1,3))<.5

```

```

8         T_data_res1(n) = (set1.data(i,3)+set3.data(ind_closest1,3))...
          /2;
9         [sheet_resistance1(n), resistivity1(n)] = vdP_solver(...
          set1.data(i,R_col),set3.data(ind_closest1,R_col),...
          thickness);
10        n=n+1;
11    end
12 end
13
14 n=1;
15 for i = 1:element_num
16     ind_closest2 = dsearchn(set4.data(:,3),set2.data(i,3));
17     if abs(set2.data(i,3)-set4.data(ind_closest2,3))<.5
18         T_data_res2(n) = (set2.data(i,3)+set4.data(ind_closest2,3))...
          /2;
19         [sheet_resistance2(n), resistivity2(n)] = vdP_solver(...
          set2.data(i,R_col),set4.data(ind_closest2,R_col),...
          thickness);
20        n=n+1;
21    end
22 end
23 end

```

B.2 Hall Measurements

Hallv4

```

1
2 %% Hall calculations and plotting
3 % Loads data for resistance vs. H at different temperatures and ...
  calculates
4 % the Hall resistance (R_Hall). Only uses data from a single bonding...
  configuration. A linear curve fit is used to extract the slope
5 % of the linear region corresponding to the ordinary Hall effect. ...
  The slope is then used
6 % to calculate the carrier density. Calculations of the mobility ...
  requires the sheet
7 % resistance to be calculated beforehand using the MR_vs_Tv5 script.
8
9 % Input data format:
10 % Requires two input files at each temperature where the first ...
  contains the resistances
11 % measured from 0 -> +X Tesla end the second from 0-> -X Tesla. See ...
  ETO
12 % script for Hall measurements.
13
14 close all
15 % clear all
16 hold on
17
18 %% Switches for plots and save functions etc.
19 plot_R_hall = 1;
20 plot_R_vs_H_switch = 0;

```

```

21 save_R_vs_H_png = 0;
22 save_RHall_vs_H_png = 0;
23 plot_mobility = 1;
24 plot_carrier_density = 1;
25 plot_lin_range = 0;
26 plot_slopes = 0;
27 plot_offsets = 0;
28 home = 1; %Determines plot placement (1 vs 2 monitors)
29 % Imports line colors and markers for better plotting clarity
30 [linestyles,MarkerEdgeColors,Markers,MarkerFaceColor ] =...
    set_linestyles(16);
31 style_type = 4;
32
33 %% Measurement specific variables
34 file_numbers =15; % Number of measurements at different temperatures
35 file_start = 0; % First file to be plotted, useful when not all ...
    temperatures are needed
36 reg_start_field = 10000; % Performs curve fit from the given field(...
    linear region), given in Oe
37 Ch_num = 1; % ETO channel used for the measurements
38 if Ch_num == 1
39     R_col = 7;
40 else
41     R_col = 27;
42 end
43
44 %% Physical parameters
45 thickness = 10e-7; % Thickness in cm
46 q = 1.6e-19;
47
48 %% Program begins
49 %Iterates over a series of measurements at different temperatures ...
    and
50 %calculates the desired quantities
51 for k=file_start:file_numbers-1
52     clear R_Hall
53
54     % Changes filename (format '****_000xx.dat') for data import
55     if k<10
56         filename1 = ['Data/Hall\5nmBTO_10nmLSMO\Hall_5nmBTO_10nmLSMO_+3...
            T_0000',num2str(k),'.dat'];%Filename of positive field data
57         filename2 = ['Data/Hall\5nmBTO_10nmLSMO\...
            Hall_5nmBTO_10nmLSMO_-3T_0000',num2str(k),'.dat'];%...
            Filename of negative field data
58     else
59         filename1 = ['Data/Hall\5nmBTO_10nmLSMO\...
            Hall_5nmBTO_10nmLSMO_+3T_000',num2str(k),'.dat'];%...
            Filename of positive field data
60         filename2 = ['Data/Hall\5nmBTO_10nmLSMO\...
            Hall_5nmBTO_10nmLSMO_-3T_000',num2str(k),'.dat'];%...
            Filename of negative field data
61     end
62
63
64     % Imports data as struct to remove header(skip xx first lines)
65     set1 = importdata(filename1,',',18);
66     set2 = importdata(filename2,',',18);

```

```

67
68 % Calculates Hall resistance R_Hall
69 for i=1:length(set1.data(:,1))
70     R_Hall(i) = (set1.data(i,R_col) - set2.data(i,R_col))/2;
71 end
72
73 % Stores temperatures and offsets for each of the field sweeps
74 T_data(k+1-file_start) = set1.data(1,3);
75 offsets(k+1) = set1.data(1,R_col)-set2.data(1,R_col);
76
77 %% Linear Regression
78 % Performs a linear regression for data points between the field
79 % value set by reg_start and the end value. By default every ...
80 % point is
81 % weighted equally. The regress() function also returns lower ...
82 % and upper
83 % bounds for the 95% confidence intervals
84 reg_start = dsearchn(set1.data(:,4),reg_start_field);
85 y= R_Hall(1,reg_start:length(set1.data(:,1)));
86 x=[ones(length(set1.data(:,1))-reg_start+1,1) set1.data(...
87     reg_start:length(set1.data(:,1)),4)];
88 [coeffs, coeffints] = regress(y',x);
89 slope(k+1-file_start) = coeffs(2)*2e4;
90 lin_range(k+1-file_start) = R_Hall(length(R_Hall)) - R_Hall(...
91     reg_start);
92
93 %% Plotting part starts
94 %Plots Hall resistance vs. field
95 if plot_R_hall
96     figure(k+1)
97     hold on
98     % Determines position of plot windows
99     if home
100         set(gcf,'position',[10+mod(k,4)*0300,940-(floor((k+1)/4...
101             .01)*250),300,190]);
102     else
103         set(gcf,'position',[-1270+mod(k,4)*300,750-(floor((k+1)...
104             /4.01)*280),300,180]);
105     end
106
107     plot((0:1.5:3),(0:15000:30000).*coeffs(2)+coeffs(1),'Color',...
108         MarkerEdgeColors{k-file_start+1});
109     plot(set1.data(:,4)/1e4,R_Hall,['-' Markers(k-file_start+1)...
110         ],'Color',MarkerEdgeColors{k-file_start+1},'...
111         MarkerFaceColor',MarkerFaceColor{k-file_start+1})
112     title(['10nmLSMO at ',num2str(round(set1.data(1,3))),'K'],'...
113         FontSize',18);
114     xlabel('Magnetic field (T)','FontSize',20);
115     ylabel('R_{Hall} (\Omega)','FontSize',20)
116
117     %Adds temperature label at end of each curve
118     labelpoints(3.43,R_Hall(length(R_Hall))+.015,[num2str(round(...
119         set1.data(1,3))),'K'],'FontSize',18);
120     set(gca,'FontSize',20);
121     box on;
122 end

```

```

113 % Option to automatically save each plot as a png file
114 if save_RHall_vs_H_png
115     filename = ['images\Hall\20nmBTO_20nmLSMO\Au contacts\Hall ...
                resistance/20nmBTO_20nmLSMO_RHall_vs_H_', num2str(round(...
                set1.data(1,3)), 'K');
116     print(filename, '-dpng')
117 end
118
119 % Plots R vs H for each temperature
120 if plot_R_vs_H_switch
121     plot_R_vs_H(k+1, home, set1.data(:,4), set2.data(:,4), set1.data...
                (:,R_col), set2.data(:,R_col), set1.data(1,3), ...
                save_R_vs_H_png)
122 end
123
124 % Calculates carrier density and error bars from the ...
    coefficients
125 % obtained from the regression
126 if plot_carrier_density
127     carrier_density(k+1-file_start) = 1e-8/(q*thickness*coeffs...
                (2));
128     lower_bound = 1e-8/(q*thickness*coeffints(2,1));
129     upper_bound = 1e-8/(q*thickness*coeffints(2,2));
130     lower_error(k+1-file_start) = abs( carrier_density(k+1-...
                file_start)-lower_bound);
131     upper_error(k+1-file_start) = abs( carrier_density(k+1-...
                file_start)-upper_bound);
132 end
133
134 %Calculates mobility if Rs has been found previously using ...
    MR_vs_Tv5 script
135 if plot_mobility
136     mobility(k+1) = 1/(carrier_density(k+1)*Rs(k+1)*q*thickness)...
                ;
137     mob_lower_bound = 1/(lower_bound*Rs(k+1)*q*thickness);
138     mob_upper_bound = 1/(upper_bound*Rs(k+1)*q*thickness);
139     mob_lower_error(k+1-file_start) = abs( mobility(k+1-...
                file_start)-mob_lower_bound);
140     mob_upper_error(k+1-file_start) = abs( mobility(k+1-...
                file_start)-mob_upper_bound);
141 end
142 end
143
144 % Plots carrier density vs T
145 if plot_carrier_density
146     figure(file_numbers+1)
147     set(gcf, 'position', [1200,500,600,400]);
148     errorbar(T_data, carrier_density./1e22, lower_error./1e22, ...
                upper_error./1e22, [ '-' Markers(style_type)], 'Color', ...
                MarkerEdgeColors{style_type}, 'MarkerFaceColor', ...
                MarkerFaceColor{style_type})
149     title('5nmBTO/10nm LSMO', 'FontSize', 18);
150     xlabel('Temperature (K)', 'FontSize', 20);
151     ylabel('Carrier density (\times 10^{22} cm^{-3})', 'FontSize', 20)...
                ;
152     ylim ([-5 12])
153     xlim ([40 410]);

```

```

154     set(gca, 'FontSize',20);
155
156     % Includes alternative right side scale for carrier density in ...
        units of
157     % holes/unit cell.
158     f = @(y2) y2./3.87e-8^3./1e22;
159     y2_ticks = [-2:6]';
160     addaxis_unit(gcf, f, y2_ticks);
161     set(gca, 'FontSize',20);
162     ylabel('Holes/unit cell', 'FontSize',20);
163 end
164
165 % Plots R_Hall(2T) calculated by the slopes found with regress()
166 if plot_slopes
167     figure(55)
168     plot(T_data, slope, [ '-' Markers(1)], 'Color', MarkerEdgeColors{1}, ...
        'MarkerFaceColor', MarkerFaceColor{1})
169     title('Slopes(2T)', 'FontSize',18);
170 end
171
172 % Plots the linear range of R_Hall as a function of temperature
173 if plot_lin_range
174     figure(56)
175     plot(T_data, lin_range, [ '-' Markers(1)], 'Color', MarkerEdgeColors...
        {1}, 'MarkerFaceColor', MarkerFaceColor{1})
176     xlabel('Temperature (K)', 'FontSize',20);
177     ylabel('Resistance (\Omega)', 'FontSize',20);
178     title('Linear range', 'FontSize',18);
179     set(gca, 'FontSize',20);
180     % ylim ([0.005 0.1])
181     xlim ([40 410]);
182 end
183
184 % Plots mobility
185 if plot_mobility
186     figure(file_numbers+2)
187     set(gcf, 'position', [50,100,600,400]);
188     errorbar(T_data, mobility, mob_lower_error, mob_upper_error, [ '-' ...
        Markers(style_type)], 'Color', MarkerEdgeColors{style_type}, ...
        'MarkerFaceColor', MarkerFaceColor{style_type})
189     title('', 'FontSize',18);
190     xlabel('Temperature (K)', 'FontSize',20);
191     ylabel('Mobility (cm^2/Vs)', 'FontSize',20);
192     set(gca, 'FontSize',20);
193 end
194
195 % Plots zero field offsets
196 if plot_offsets
197     figure(file_numbers+3)
198     set(gcf, 'position', [50,100,600,400]);
199     plot(T_data, offsets, [ '-' Markers(style_type)], 'Color', ...
        MarkerEdgeColors{style_type}, 'MarkerFaceColor', ...
        MarkerFaceColor{style_type})
200     title('', 'FontSize',18);
201     xlabel('Temperature (K)', 'FontSize',20);
202     ylabel('Resistance (\Omega)', 'FontSize',20);
203     set(gca, 'FontSize',20);

```

204 end

plot R vs H

```

1 function [ ] = plot_R_vs_H(fig_num,home,Hpos,Hneg,Rpos,Rneg,cur_T,...
    save_R_vs_H_png )
2 % Plots Resistance vs H for each temperature
3
4 %----- List of arguments:-----
5 % fig_num: number of figure window generated by plot
6 % home: Determines position of plot windows
7 % Hneg:negative field values
8 % Hpos:positive field values
9 % Rpos: positive resistance values
10 % Rneg: negative resistance values
11 % cur_T: temperature for current measurement
12 % save_R_vs_H_png: switch for save function
13
14 figure(fig_num)
15 if home
16     set(gcf,'position',[10+mod(fig_num,3)*0300,940-(floor((fig_num...
        +1)/3.01)*250),300,190]); %Home PC
17 else
18     set(gcf,'position',[-1270+mod(fig_num,4)*300,750-(floor((fig_num...
        +1)/4.01)*280),300,180]); % Laptop
19 end
20 % Plots R values for positive and negative field values
21 plot(Hpos/1e4,Rpos,'-r*')
22 hold on
23 plot(Hneg/1e4,Rneg,'-b*')
24 title(['10nm BTO at ',num2str(round(cur_T)), 'K']);
25 xlabel('Magnetic field (Tesla)');
26 ylabel('R (\Omega)')
27 set(gca,'FontSize',20); %sets tick fontsize, plots as xaxis in Tesla
28
29 % Saves current figure as png
30 if save_R_vs_H_png
31     filename = ['images\Hall\5nmTO_10nmLSMO/5...
        nmTO_10nmLSMO_Hall_R_vs_H_',num2str(round(cur_T)), 'K'];
32     print(filename,'-dpng') %saves current plot
33 end
34 end

```

B.3 MR vs. Magnetic Field

MR vs Hv2

```

1 %% Magnetoresistance vs. H plotting tool
2 % Calculates and plots magnetoresistance as a function of magnetic ...
    field at
3 % a range of temperature

```

```

4
5 % Input data format:
6 % Requires resistance to be measured from 0 -> x Tesla at a given ...
   set of
7 % temperatures. See ETO" scrip MR vs magnetic field"
8
9 clear all
10 close all
11 clc
12 hold on
13
14 %% Switches for plots and save functions
15 plot_MR_values = 1;
16 plot_end_MR_values = 3;
17 file_numbers = 9;
18 file_start = 0;
19 home = 1; %Determines plot placement (1 vs 2 monitors)
20 Ch_num = 0; % ETO channel used for the measurements
21 R_col = 7;
22 if Ch_num == 1
23     R_col = 7;
24 else
25     R_col = 27;
26 end
27 % Imports line colors and markers for better plotting clarity
28 [linestyles,MarkerEdgeColors,Markers,MarkerFaceColor ] =...
   set_linestyles(16);
29 style_type = 4;
30
31 %% Program begins
32 %Iterates over a series of measurements at different temperatures
33 for k=file_start:file_numbers-1
34     %Imports data at each for each set at a given temperature
35     if k<10
36         set1 = importdata(['Data/R_Hsweep\10nmLSMO/10...
           nmLSMO_R_vs_H_260_400K_0000',num2str(k),'.dat'],'',18)...
           ;
37     else
38         set1 = importdata(['Data/R_Hsweep\10nmLSMO/10...
           nmLSMO_R_vs_H_260_400K_000',num2str(k),'.dat'],'',18);
39     end
40
41     element_num = length(set1.data(:,1));
42     %Calculates magnetoresistance vs H
43     for i=1:element_num
44         MR_values(i) = (set1.data(1,R_col)-set1.data(i,R_col))/...
           set1.data(i,R_col)*100;
45     end
46     % Saves MR at highest field value for further analysis
47     MR_end_values(k+1) = MR_values(element_num);
48     T_data(k+1) = set1.data(1,3);
49
50     %Plots MR as a function of H at a given temperature
51     if plot_MR_values
52         figure(k+1)
53         if home

```



```

54         set(gcf,'position',[10+mod(k,3)*0300,940-(floor((k+1)/3...
55             .01)*250),300,190]); %Home PC
56     else
57         set(gcf,'position',[-1270+mod(k,4)*300,750-(floor((k+1)...
58             /4.01)*280),300,180]); % Laptop
59     end
60     plot((set1.data(:,4)./1e4)',MR_values,[ '-' Markers(k+1-...
61         file_start)],'Color',MarkerEdgeColors{k+1-file_start},'...
62         MarkerFaceColor',MarkerFaceColor{k+1-file_start}) % ...
63         Plots positive R values for positive H
64     title([' at ',num2str(round(set1.data(1,3))),'K']);
65     % Adds temperature label at each temperature, useful for ...
66     many plots
67     % in same figure
68     labelpoints(3.43,MR_values(element_num)+.015,[num2str(round(...
69         set1.data(1,3)),' K'],'FontSize',18);
70     xlabel('Magnetic field (Tesla)');
71     ylabel('MR (%)','FontSize',20)
72     set(gca,'FontSize',20); %sets tick fontsize, plots as xaxis ...
73     in Tesla
74     box on;
75 end
76 end
77 end
78
79 %Plots high field MR values at each of the temperatures
80 if plot_end_MR_values
81     figure(k+2)
82     plot(T_data,MR_end_values,'-r*')
83     title([' at ',num2str(round(set1.data(1,3))),'K']);
84     xlabel('Magnetic field (Tesla)');
85     ylabel('MR (%)','FontSize',20)
86     set(gca,'FontSize',20);
87     box on;
88 end
89 end

```

B.4 General Functions

set linestyles

```

1 function [linestyles MarkerEdgeColors Markers MarkerFaceColor] = ...
2     set_linestyles( n )
3
4 linestyles = cellstr(char('-',':','-.', '--', '-|', ':|', '-|', '--', '-|', ':|', ...
5     '-|', '--', '-|', ':|', '-.', '--', '-|', ':|', '-.'));
6
7 % MarkerEdgeColors=jets(n); % n is the number of different items you...
8     have
9 MarkerEdgeColors = {'k','b','r','g','c',[.8 .5 .3],[.5 .6 .7],[.8 .2...
10     .6],[.8 .1 .4],[.3 .7 .6],[.8 .1 .1],[.4 .4 .4],...
11     [.1 .1 .6],[.8 .5 .2],[.8 .5 .2],[.8 .7 .7],[.3 .5 .2],[.1 .8 .4]};

```

```
10 MarkerFaceColor = {'k','b','r','g','c','m',[.5 .6 .7],[.8 .2 .6],[.8...  
    .1 .4],[.3 .7 .6],[.8 .1 .1],[.4 .4 .4],...;  
11 [.1 .1 .6],[.8 .5 .2],[.8 .7 .7],[.3 .5 .2],[.1 .8 .4]};  
12 Markers={'o','*','^','x','s','+','d','v','^','<','>','x','h',...  
13 '+','o','x','<','h','.', '>', 'p', 's', 'd', 'v', ...  
14 'o', 'x', '+', '*', 's', 'd', 'v', '^', '<', '>', 'p', '.'};  
15 end
```

Additionally the externally downloaded function *labelpoints.m* was used in some of the scripts. This can be downloaded at

<http://www.mathworks.com/matlabcentral/fileexchange/46891-labelpoints>

Appendix C: Testing Structures

Table C.1 lists the sample structures that were used for testing purposes during the establishment of the technique. Since these were harmed in the process, they were not used in the final study.

Table C.1: Sample structures used for testing purposes during the establishment of the technique.

Sample
20 nm LSMO
BTO(20 nm)/LSMO(10 nm)
BTO(20 nm)/LSMO(20 nm)
BTO(100 nm)/LSMO(10 nm)
LSMO(10 nm)/LSMO(10 nm)
LSMO(10 nm)/BTO(20 nm)